UNIVERSITY OF CALIFORNIA
SANTA CRUZ

# INVESTIGATION OF LOCAL STRUCTURE ANOMALIES AT LOW TEMPERATURE IN $URu_{2-X}Fe_XSi_2$

A thesis submitted in partial satisfaction of the
requirements for the degree of

MASTER OF SCIENCE

in

PHYSICS

by

**Ryan K. Dudschus**

June 2019

The Thesis of Ryan K. Dudschus
is approved:

Professor Frank Bridges, Chair

Professor David P. Belanger

Professor Jairo Velasco Jr.

Lori Kletzer
Vice Provost and Dean of Graduate Studies

# Table of Contents

# List of Figures

# List of Tables

**Abstract**

Investigation of Local Structure Anomalies at Low Temperature in $URu_{2-x}Fe_xSi_2$

by

Ryan K. Dudschus

The Ru K, Fe K, and the U $L_{III}$ absorption edge of $URu_{2-x}Fe_xSi_2$ were investigated by the EXAFS technique. No change in the electronic structure was found in the U $L_{III}$ absorption edge as the Fe concentration varied. Tiny changes in the electronic structure were found in the Ru K absorption edge and the Fe K absorption edge in relation to the Fe concentration. However, the variation in these structures are at the limit of our resolution. The distance between U with its nearest U neighbor was found to decrease from 4.12 Å to 4.11 Å as the concentration x of Fe increased from x=0.00 to x=0.20. Position plots of U with its nearest Ru neighbor and nearest Si neighbor indicate a decreases in distance as temperature decreases. Position plots of Fe K edge show evidence for Fe doping on the Ru site acts as a chemical pressure; the Fe-Si distance decreases by 0.05 Å. The Debye-Waller factor was plotted as a function of temperature which led to the finding of excess disorder in the Ru-Si, Ru-U, U-Ru, and U-U pairs. The remaining atomic pairs fit the Debye model reasonably well. The Ru-Si pair showed a significant increase in $\sigma^2$ from 70 K to 25 K, indicating a split Ru-Si peak. The Ru-U, U-Ru, and U-U pairs also showed a slight increase in disorder at low temperature. A distortion model was constructed that followed these results where the ab-plane of the tetragonal structure of $URu_{2-x}Fe_xSi_2$ distorts from a square

to a rectangle, resulting in an orthorhombic structure in the low temperature region. The elongation of the ab-plane is able to happen along either the a-axis or the b-axis since Ru may have two distinct positions due to the splitting of the Ru-Si bond. This orthorhombic distortion does not affect the U-Si or the Ru-Ru distances which agrees with no excess disorder found in their corresponding $\sigma^2$ plots. A resulting mix of this effect on a local scale (few nm) will have the structure appear tetragonal to X-ray diffraction techniques.

To my parents,

Brad and Stephanie,

who provided me with the opportunity to expand my knowledge in the world of physics.

## Acknowledgments

An enormous thank you to Frank (Bud) Bridges, who provided me with this amazing opportunity for which I am eternally grateful. Thank you for all of your help, wisdom, and support through this journey!

# Chapter 1

# Introduction

$URu_2Si_2$ is one of the most interesting heavy fermion uranium based crystals. The most interesting feature of $URu_2Si_2$ is mysterious phase transition that occurs at 17.5 K [11, 12, 13]. Resistivity measurements as temperature decreases reveal a sharp minimum around 18 K and a local maximum around 17 K [13, 11]. Specific heat measurements as a function of temperature reveal a sharp increase near 17 K [12, 13]. These results indicate a phase transition occurs at 17.5 K, along with a significantly small U magnetic moment around 0.03 $\mu_B$ [14, 15]. This phase change appears to be non-magnetic; However, this small magnetic moment suggests that there could be an impurity in the sample, or some other lattice defect, or the electron spins are not exactly aligned.

Through today, the order parameter of this phase transition is still unknown, resulting in the name hidden order (HO) phase. Lately, it was discovered that under moderate pressure, around 0.5 GPa, the HO phase gives way to a large moment

antiferromagnetic (LMAFM) phase where the U magnetic moment increases to $0.4\mu_B$ [20]. Kanchanavatee et al. (2011) determined that Fe doping on the Ru site in $URu_2Si_2$ behaves as a chemical pressure; the smaller size of Fe causes the structure of $URu_2Si_2$ to contract, similar to that of an external pressure [21]. The HO phase gives way to the LMAFM phase when the Fe concentration in $URu_{2-x}Fe_xSi_2$ reaches x=0.10 [21]. In this paper, we will use the EXAFS technique to investigate the behavior of the lattice structure of $URu_{2-x}Fe_xSi_2$ from 10 K to 300 K, in hopes that the hidden order parameters might show up in the local structure. This chapter will focus on the necessary background and theory behind the EXAFS technique, as well as $URu_{2-x}Fe_xSi_2$.

## 1.1 Photoelectric Effect

X-rays are a type of light that have high energy, on the order of thousands of electron-volts (eV). This allows X-rays to penetrate and probe materials that are opaque to lower energy forms of light. As a photon, or a quantum of light, is absorbed by a material, its energy is transferred to an electron in the material. This excites the electron to a higher energy level, if that level is not already filled.

The absorption of X-rays does not always happen. Electrons in an atom occupy quantized energy states, while filling the lowest energy states first. These quantized energy states, or bands, have widths that are attributed to multiple types of broadening. All possible energy states are not filled, leading to a cutoff energy where all

energy states below this cutoff energy are filled and all energy states above this cutoff energy are empty. This cutoff energy is known as the chemical potential, or Fermi level.

Above the chemical potential, the electron energy bands overlap due to the broadening, resulting in the formation of a continuous empty energy band; low energy electrons may be excited into this continuum band by x-rays if the x-ray energy is high enough. Specifically, X-ray absorption occurs when the energy of an incident X-ray exceeds the threshold for a given inner electron shell, such as the 1s orbital and the 2p orbital; less energy is required to excite higher energy electrons to the continuum. Figure 1.1 shows a simplified depiction of the quantized energy states of a material.

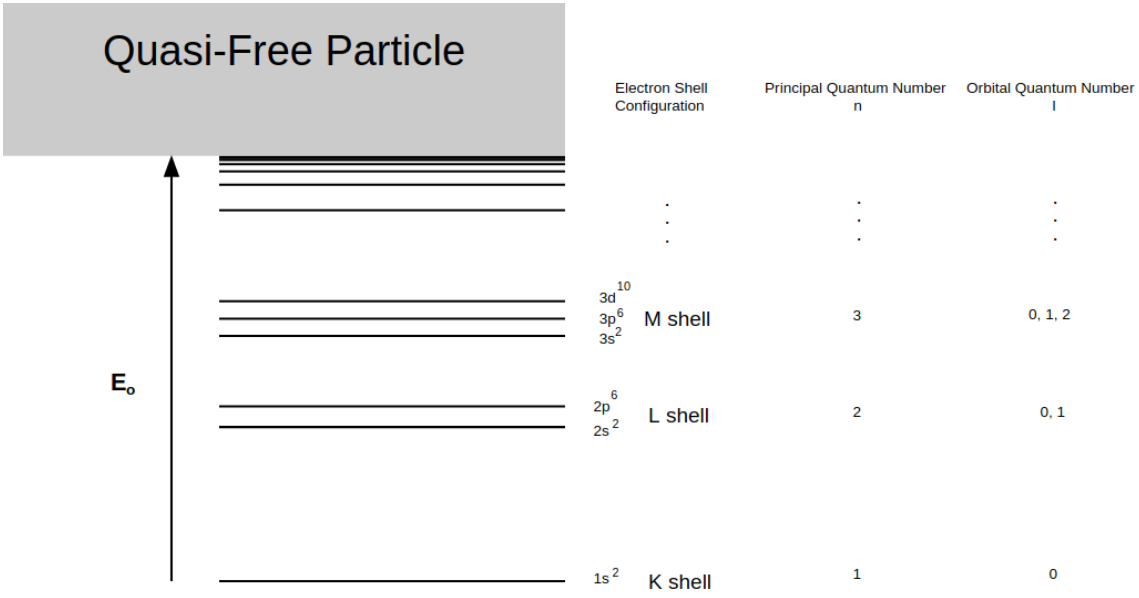


Figure 1.1: Simplified model of the quantized electron energy states of an atom, which are depicted by the horizontal lines. The energy $E_o$ represents the energy required to eject an electron from the K shell.

The lowest couple of energy states have labels that show the electronic configura-

tion for each shell, as well as the corresponding principal quantum number and orbital quantum number. If an incident X-ray has enough energy, it will eject an electron from the atom, which places the ejected electron into a quasi-free state since it still feels the potential from the core atom, or the atom that the photoelectron originated from. This phenomena is known as the photoelectric effect and the ejected electron is known as a photoelectron, and the energy needed to eject a photon is known as the ionization energy. In Figure 1.1, $E_o$ is the energy needed for an X-ray to eject an electron from the K shell (1s orbital). An electron in the K shell is tightly bound to the atom, which is called the core atom. Note that the ionization energy to eject an electron from the K shell is unique for each atom.

When the absorption of these monochromatic X-rays are measured as a function of energy, sudden steps are seen at the energies that are needed to eject an electron from corresponding inner electron shell. These steps are known as absorption edges. Figure 1.2 demonstrates the U $L_{III}$ absorption edge.

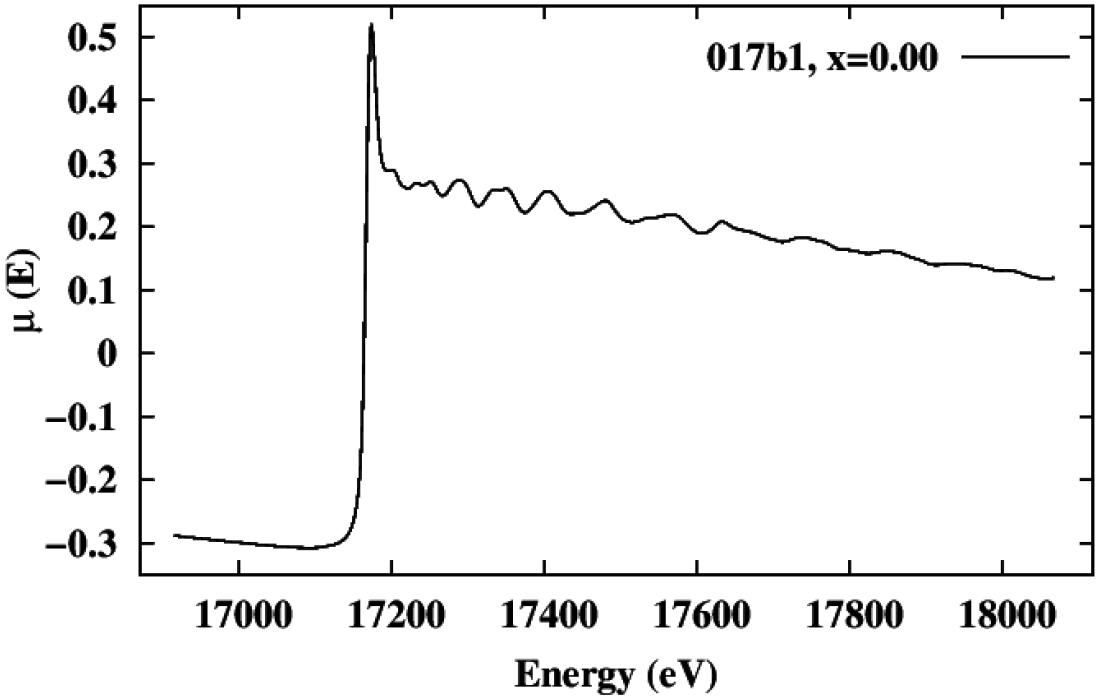


Figure 1.2: U $L_{III}$ absorption edge transmission data with no Fe concentration taken at 4 K.

As an electron from a deep energy level is ejected from its shell, it leaves behind an empty energy state known as a hole. The lifetime of a core hole is on the order of $10^{-16}$s, in which an electron in a higher energy state decays to fill the core hole, since electrons occupy the lowest possible energy state. In order for the electron in the higher energy state to drop down to occupy the lower energy state, it must emit a photon whose energy is equal to the difference between the two energy states so that energy is conserved. The emission of these photons are known as fluorescence. Figure 1.3 depicts this process.

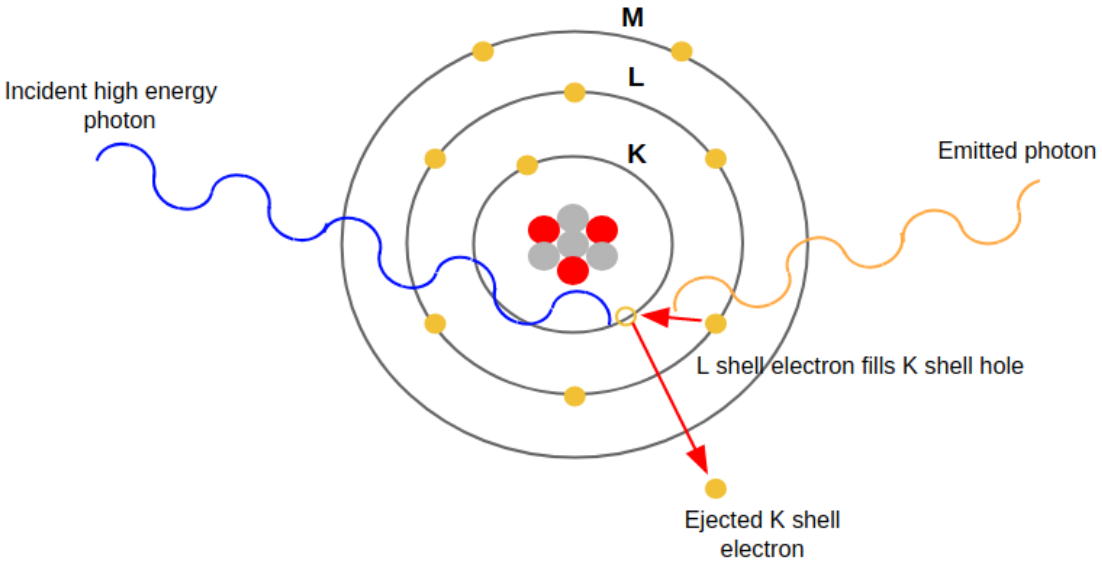


Figure 1.3: Generalized photoelectric effect. An incident high energy photon (blue wave) ejects a K shell electron, leaving behind a hole. An electron in the L shell transitions to fill the hole, emitting a lower energy photon (yellow wave) in the process.

The emitted photon from the core hole decay process or the ejected photoelectron may have enough energy to excite a higher energy electron of the core atom into the continuum. This will leave behind another hole that will eventually decay and emit another photon. This secondary photon emission process is known as the Auger effect [1].

## 1.2 Crystalline Solid

This section follows the discussion taken place in *Solid State Physics* by Ashcroft and Mermin, and *The Oxford Solid State Basics* by Steven H. Simon.

A crystal is a material whose structure is in a highly ordered arrangement. The structure of a crystal in real space (r-space) is described by it's direct lattice, or where the set of atomic positions in the crystal are defined by a basis which consists of a set of linearly independent vectors, known as lattice vectors, where the addition of any two lattice vectors results in a third vector that is in the set. The set of lattice vectors in r-space $\vec{R}$ is defined as

$$\vec{R} = n_1\vec{a_1} + n_2\vec{a_2} + n_3\vec{a_3}, \tag{1.1}$$

where $n_1$, $n_2$, and $n_3$ are integers, and $\vec{a_1}$, $\vec{a_2}$, and $\vec{a_3}$ are the lattice vectors that make up the basis. However, it is important to note that the choice of lattice vectors are not unique. Figure 1.4 below shows a two dimensional case of lattice vectors.

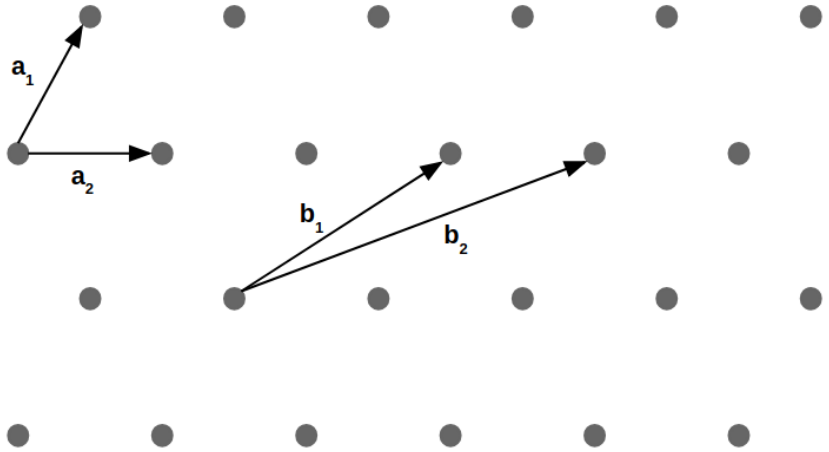


Figure 1.4: Two possible arrangements of lattice vectors that form a basis for the given crystalline structure.

A crystalline structure is also a periodic structure, which can be seen in Figure 1.4. If the basis of the r-space lattice vectors is moved to another atom in the crystal, the same structure is recreated using the same basis; $x \rightarrow x + na$, where n is an integer, and a is the spacing between lattice points, or the lattice constant. This allows a simplified form of the crystal to be constructed called a unit cell. A unit cell is a select region of the crystalline structure that is chosen such that the entire crystal may be reconstructed by a repeated tiling of the selected region. If a lattice point is on the boundary of the unit cell, only the fraction of what is in the unit cell is counted. There are a couple of different methods to construct a unit cell. Two of the most popular methods are the primitive unit cell, which contains exactly one lattice point, and the conventional unit cell, or Bravais lattice, which is chosen to show the symmetry of the lattice based on an orthogonal basis. The basis of a unit cell describes the position of each lattice point within the unit cell from a reference

point. Figure 1.5 displays an example of both of these unit cells.

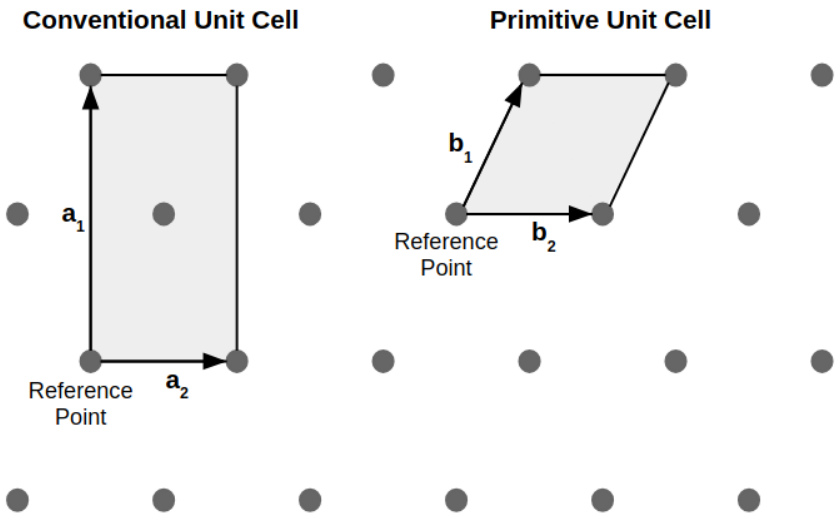


Figure 1.5: A conventional unit cell and a primitive unit cell for the given crystalline structure.

It is useful to study the crystalline solid in reciprocal space, or k-space, since the physics of a wave is described in terms of the wavenumber k. The wavenumber is defined by $k = \frac{2\pi}{\lambda}$, where $\lambda$ is the wavelength of the propagating wave. The derivation of the dispersion relation, or the relationship between frequency and wavevector ($\vec{k} = \mathrm{k}\hat{n}$), for a 1 dimensional monatomic chain of atoms shows that the wavenumber is also periodic by a spacing of $\frac{2\pi}{a}$, where a is the lattice constant. This means that two points in k-space are equivalent if the difference between them is an integer multiple of $\frac{2\pi}{a}$, or

$$G_m = \frac{2\pi}{a} m = k_1 - k_2, \tag{1.2}$$

where $\mathrm{k}_1$ and $\mathrm{k}_2$ are k-space lattice points, m is an integer, and $\mathrm{G}_m$ is the set of points

that form the reciprocal lattice. A plane wave is generally described as

$$Ae^{i(\omega t - kx)} = Ae^{i(\omega t - kna)}, \tag{1.3}$$

where A is the amplitude of the wave, $\omega$ is the frequency, t is time, k is the wavenumber of the wave, and x is the position of the wave. The r-space periodic condition has already been inserted into the plane wave equation. The k-space periodicity results in the plane wave being invariant under conditions of integer multiples of $\frac{2\pi}{a}$, which leads to

$$e^{-i2\pi mn} = 1. \tag{1.4}$$

This returns the same plane wave prior to inserting the periodic conditions. Generalizing Eq. 1.4 to multiple dimensions allows for the reciprocal lattice to be defined by

$$e^{i\vec{G}\cdot\vec{R}} = 1, \tag{1.5}$$

where $\vec{G}$ is the set of points that make the reciprocal lattice, and $\vec{R}$ is the set of points that construct the direct lattice. From Eq. 1.5, the basis vectors for k-space are the

following:

$$\vec{b_1} = \frac{2\pi\vec{a_2} \times \vec{a_3}}{\vec{a_1} \cdot (\vec{a_2} \times \vec{a_3})} \tag{1.6}$$

$$\vec{b_2} = \frac{2\pi\vec{a_3} \times \vec{a_1}}{\vec{a_1} \cdot (\vec{a_2} \times \vec{a_3})} \tag{1.7}$$

$$\vec{b_3} = \frac{2\pi\vec{a_1} \times \vec{a_2}}{\vec{a_1} \cdot (\vec{a_2} \times \vec{a_3})} \tag{1.8}$$

such that the set of all points in the reciprocal space $\vec{G}$ is defined as

$$\vec{G} = m_1\vec{b_1} + m_2\vec{b_2} + m_3\vec{b_3}, \tag{1.9}$$

where $m_1$, $m_2$, and $m_3$ are integers, and $\vec{b_1}$, $\vec{b_1}$, and $\vec{b_1}$ are reciprocal space lattice vectors.

## 1.3 Space Groups

A crystal is made up of a periodic arrangement of one or more atoms at each lattice points, as discussed in Section 1.2. There exists a certain arrangement of atoms that may be grouped together such that the repetition of this group constructs the structure of the crystal, known as a unit cell. One of the simplest forms of a unit cell is the Bravais lattice, which is created by discrete translations amongst the direct lattice. The application of other symmetry operations, such as reflection and rotation, lead to 230 unique types of space groups. If two groups of Bravais lattices

have the same symmetry operations, then they are equivalent Bravais lattices. This results in 14 possible Bravais lattices in three dimensions.

$URu_2Si_2$ has a simple tetragonal crystal structure that can be seen below in Figure 1.6.

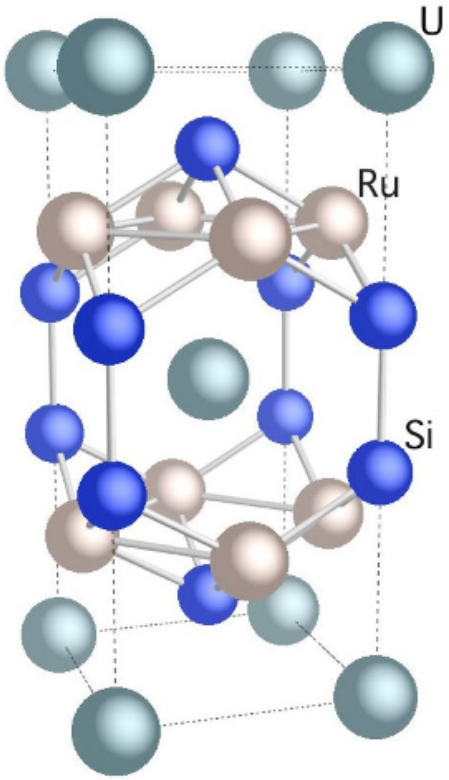


Figure 1.6: Unit cell of $URu_2Si_2$. It has a tetragonal crystal structure with a I / 4mmm space group. The green spheres represent U atoms, the blue sphere represent Si atoms, and the grey represent Ru atoms. The a-axis is in the direction of the shortest U-U bond, as with the b-axis, but perpendicular to the a-xis. The c-axis is perpendicular to both the a-axis and b-axis.

$URu_2Si_2$ belongs to the space group I 4/mmm, or space group 139. This means that this crystal structure is highly symmetrical. This is shown in Table 1.1 below, which was taken from cryst.ehu.es [9]. The structure that we used for $URu_2Si_2$ has U placed at site a, Ru placed at site d, and Si placed at site e.

Table 1.1: Symmetry of Space Group 139

| Multiplicity | Wyckoff Letter | Site Symmetry | Coordinates<br>(0,0,0) + $(\frac{1}{2},\frac{1}{2},\frac{1}{2})$ |
|---|---|---|---|
| 32 | o | 1 | (x,y,z) (-x,-y,z) (-y,x,z) (y,-x,z)<br>(-x,y,-z) (x,-y,-z) (y,x,-z) (-y,-x,-z)<br>(-x,-y,-z) (x,y,-z) (y,-x,-z) (-y,x,-z)<br>(x,-y,z) (-x,y,z) (-y,-x,z) (y,x,z) |
| 16 | n | .m. | (0,y,z) (0,-y,z) (-y-,0,z) (y,0,z)<br>(0,y,-z) (0,-y,-z) (y,0,-z) (-y,0,-z) |
| 16 | m | ..m | (x,x,z) (-x,-x,z) (-x,x,z) (x,-x,z)<br>(-x,x,-z) (x,-x,-z) (x,x,-z) (-x,-x,-z) |
| 16 | l | m.. | (x,y,0) (-x,-y,0) (-y,x,0) (y,-x,0)<br>(-x,y,0) (x,-y,0) (y,x,0) (-y,-x,0) |
| 16 | k | ..2 | (x,x+$\frac{1}{2}$,$\frac{1}{4}$) (-x,-x+$\frac{1}{2}$,$\frac{1}{4}$) (-x+$\frac{1}{2}$,x,$\frac{1}{4}$)<br>(x+$\frac{1}{2}$,-x,$\frac{1}{4}$) (-x,-x+$\frac{1}{2}$, $\frac{3}{4}$) (x,x+$\frac{1}{2}$, $\frac{3}{4}$)<br>(x+$\frac{1}{2}$,-x, $\frac{3}{4}$) (-x+$\frac{1}{2}$,x, $\frac{3}{4}$) |
| 8 | j | m2m . | (x,$\frac{1}{2}$,0) (-x,$\frac{1}{2}$,0) ($\frac{1}{2}$,x,0) ($\frac{1}{2}$,-x,0) |
| 8 | i | m2m . | (x,0,0) (-x,0,0) (0,x,0) (0,-x,0) |
| 8 | h | m.2 m | (x,x,0) (-x,-x,0) (-x,x,0) (x,-x,0) |
| 8 | g | 2mm . | (0,$\frac{1}{2}$,z) ($\frac{1}{2}$,0,z) (0,$\frac{1}{2}$,-z) ($\frac{1}{2}$,0,-z) |
| 8 | f | ..2/m | ($\frac{1}{4}$,$\frac{1}{4}$,$\frac{1}{4}$) ($\frac{3}{4}$,$\frac{3}{4}$,$\frac{1}{4}$) ($\frac{3}{4}$,$\frac{1}{4}$,$\frac{1}{4}$) ($\frac{1}{4}$,$\frac{3}{4}$,$\frac{1}{4}$) |
| 4 | e | 4mm | (0,0,z) (0,0,-z) |
| 4 | d | -4m2 | (0,$\frac{1}{2}$,$\frac{1}{4}$) ($\frac{1}{2}$,0,$\frac{1}{4}$) |
| 4 | c | mmm . | (0,$\frac{1}{2}$,0) ($\frac{1}{2}$,0,0) |
| 2 | b | 4/mmm | (0,0,$\frac{1}{2}$) |
| 2 | a | 4/mmm | (0,0,0) |

## 1.4 Conditions for X-ray Scattering

Previously, it was discussed how an incoming X-ray with a high enough energy is able to eject an inner shell electron. The incoming X-ray could scatter off of an electron that surrounds an atom instead of being absorbed. If the atoms are arranged in a periodic fashion to form a crystal, the scattered X-rays from each atom will interact with each other and result in constructive and destructive interference.

### 1.4.1 Bragg's Law

In 1913, Lawrence Bragg and William Henry Bragg discovered that crystals that are bombarded with monochromatic X-rays, or X-rays of a single wavelength, at specific incident angles form patterns of sharp intensity peaks [2]. In order to describe the sharp peaks in intensity, Lawrence Bragg assumed that the atoms in the crystal are equally spaced in parallel lattice planes that are separated by a distance $d$. It is important to note that there are many different ways of labeling parallel lattice planes in a crystal structure. He also assumed that elastic scattering occurs, where the energy of the X-ray is conserved, as well as that specular reflection takes place, or that the incident angle of reflection is equal to the angle of reflection. Bragg also made the assumption that the incident monochromatic X-rays that are reflected from successive lattice planes must constructively interfere with each other. Figure 1.7 models the method Lawrence Bragg used.

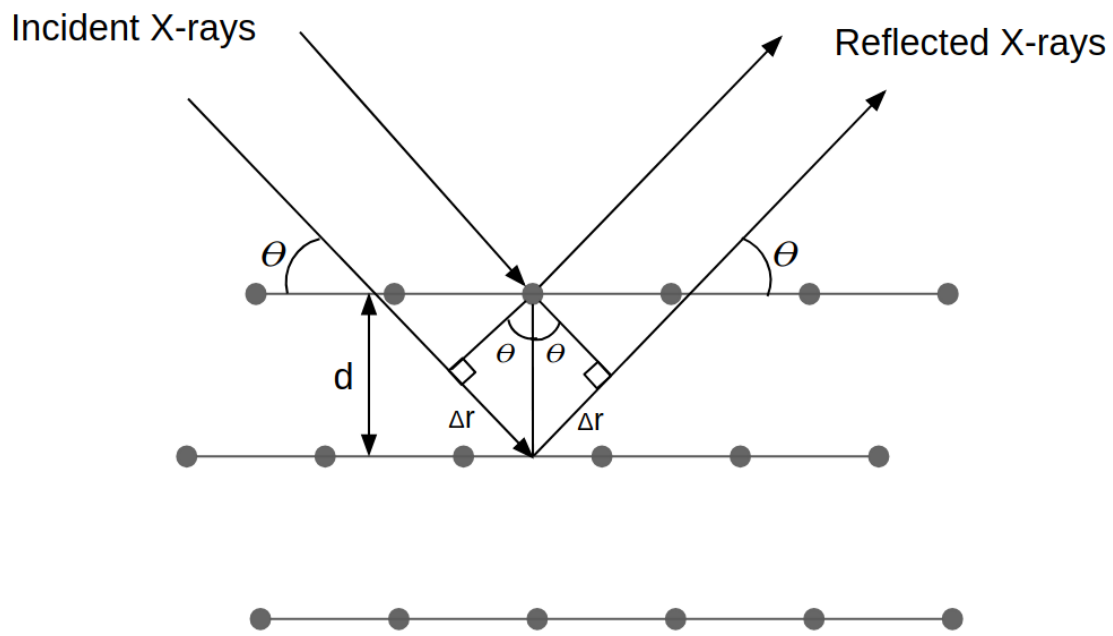


Figure 1.7: Monochromatic X-rays scattering off of a family of lattice planes that are separated a distance $d$ apart. One of the two X-rays is shown to scatter off of a neighboring lattice plane. The path length difference between the two X-rays is $2dsin(\theta) = m\lambda$.

In Figure 1.7, $d$ is the distance between parallel lattice planes, $\theta$ is the angle with respect to the lattice plane where the incident and reflected X-rays interact with the lattice plane.

An incident monochromatic X-ray that interacts with an atom at a successive lattice plane will travel more distance than an incident monochromatic X-ray that strikes the lattice plane above. This extra distance traveled is known as the path length difference $2\Delta r$. A line perpendicular to both path lengths is drawn from the tip of the shorter path length to the longer path length, which is shown in Figure 1.7. Trigonometry determines that the path length difference between the two incident

X-rays to be

$$2\Delta r = 2dsin\theta$$

In order to maintain that the two scattered X-rays constructively interfere with each other, the total path length difference should equal an integer multiple of their wavelength, or

$$2dsin\theta = m\lambda \tag{1.10}$$

where m is an integer, and $\lambda$ is the wavelength of the monochromatic X-rays. Eq. 1.10 is known as Bragg's Law.

### 1.4.2 Laue's Condition

Unlike Bragg's Law, Max von Laue did not assume that the X-ray energy was conserved, that specular reflection did not occur, and that certain lattice planes are not considered. Instead, Laue treated the atoms in a crystal as being placed in the direct lattice at points $\vec{R}$, and that each atom is able to scatter the incident X-ray in any direction. The assumption that the sharp peaks of intensity occur when the scattered X-rays constructively interfere is still kept.

Let two atoms that will scatter incident X-rays be a distance $d$ apart. Let the incident monochromatic X-rays with wavelength $\lambda$ travel in direction $\hat{\vec{n}}$, with its wavevector given as $\vec{k} = 2\pi\hat{\vec{n}}/\lambda$. Similarly, let the scattered X-rays with wavelength $\lambda$ travel in a direction $\hat{\vec{n'}}$, with its wavevector given as $\vec{k'} = 2\pi\hat{\vec{n'}}/\lambda$. This is shown in

Figure 1.8, where $\theta$ is the angle of incidence with respect to the distance $d$ between the two atoms, and $\theta'$ is the angle of reflection with respect to the distance $d$ between the two atoms.

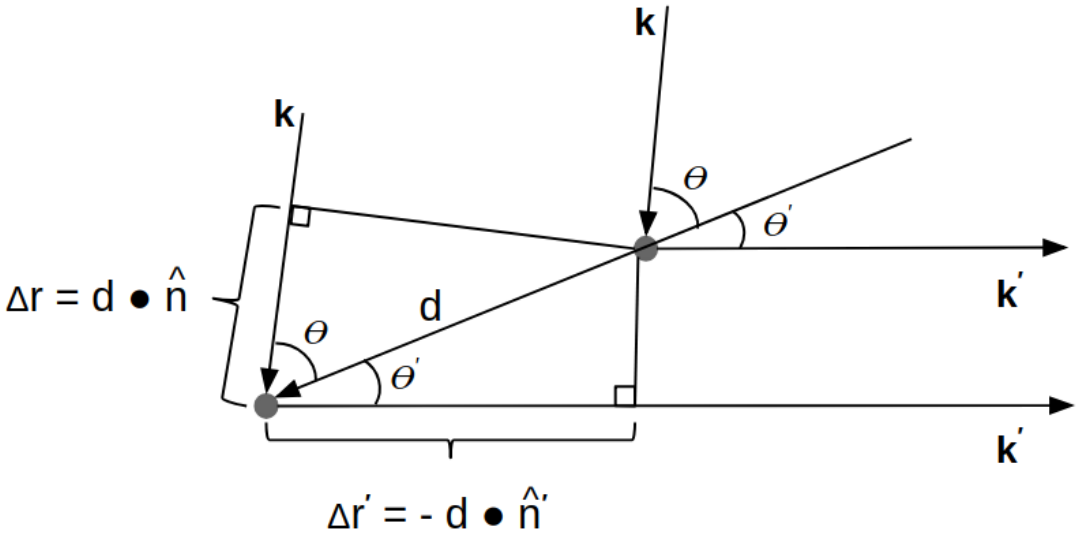


Figure 1.8: Two incident X-rays scattering off of two lattice points separated by a distance $d$. The path difference is given by Eq. 1.11.

From Figure 1.8, it is seen that the total path length difference is

$$\Delta r + \Delta r' = dcos\theta + dcos\theta' = d \cdot \hat{n} - d \cdot \hat{n'} \tag{1.11}$$

In order to make sure that the reflected X-rays constructively interfere, they must be an integer multiple of their wavelength $m\lambda$

$$d \cdot (\hat{n} - \hat{n'}) = m\lambda. \tag{1.12}$$

Multiplying both sides of Eq. 1.12 by $\frac{2\pi}{\lambda}$ results in

$$d \cdot (\vec{k} - \vec{k'}) = 2\pi m. \tag{1.13}$$

However, this brief derivation only considers one set of scattering within the crystal. The two atoms are located at points described by their corresponding direct lattice vector. The entire set of direct lattice vectors $\vec{R}$ describes the location of every atom where, by definition, the difference between two direct lattice vectors results in another direct lattice vector. Therefore, the distance between two atoms in the crystal is a direct lattice vector. This allows the distance between atoms in Eq. 1.13 to be replaced by the set of direct lattice vectors

$$\vec{R} \cdot (\vec{k} - \vec{k'}) = 2\pi m. \tag{1.14}$$

This equation may also be rewritten as

$$e^{i(\vec{k'} - \vec{k}) \cdot \vec{R}} = 1. \tag{1.15}$$

The Laue condition definition is found by comparing Eq. 1.14 to Eq. 1.5, which is the definition of the reciprocal lattice. The Laue condition is written as

$$\vec{G} = \vec{k'} - \vec{k}, \tag{1.16}$$

where the difference between the incident and the outgoing wavevector must be a reciprocal lattice vector.

### 1.4.3 Ewald Sphere Construction

In 1921, Paul Peter Ewald created a pictorial method to visualize the sharp intensity peaks that are created by X-ray scattering by a crystal structure [3]. Let the incident wavevector be $\vec{k}$. In reciprocal space, draw a sphere of radius $|\vec{k}|$, where the tip of the wavevector $|\vec{k}|$ is at the origin of the sphere and the sphere intersects two reciprocal lattice points. This results in the emission of a scattered wavevector $\vec{k'}$ in which the Laue condition is satisfied. Bragg's law will also be satisfied for the family of direct lattice planes that are perpendicular to the reciprocal lattice vector $\vec{G}$ that is the difference between the incident wavevector $\vec{k}$ and the scattered wavevector $\vec{k'}$. The Ewald Sphere construction is depicted in Figure 1.9 below.

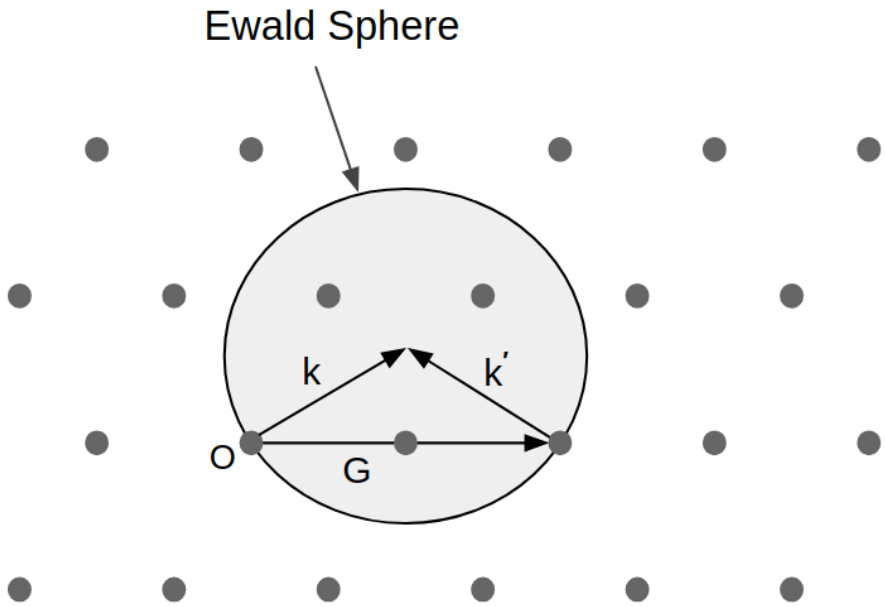


Figure 1.9: Construction of an Ewald Sphere. Given the incident wavevector $\vec{k}$, a sphere of radius $|\vec{k}|$ is drawn about an origin. Constructive interference will only occur if the difference between the scattered wavevector $\vec{k'}$ and the incident wavevector is a reciprocal lattice vector $\vec{G}$. As the length of $\vec{k}$ increases, the radius of the Ewald sphere increases and sometimes a third point may also fall on the Ewald sphere. This is the condition for a monochromator glitch formation.

Let the surface of the sphere be pinned to the two reciprocal lattice points that it currently intersects, but is allowed to radially expand. The surface will eventually intersect another reciprocal lattice point(s), resulting in multiple scattering cases to occur. These multiscattering cases may create small sharp peaks in the data that are known as glitches.

## 1.5 Electron Scattering

If the binding energy of one of the inner shell electrons is $E_o$, that inner shell electron will absorb an incoming X-ray of energy $E > E_o$ and will be ejected from the atom. If the lattice site potentials are ignored, the photoelectron will have an average energy $E_e$ defined as

$$E_e = E - E_o = \frac{p^2}{2m_e}, \tag{1.17}$$

where p is the momentum of the photoelectron, and $m_e$ is the mass of the photoelectron. The photoelectron has a velocity and direction associated with it. However, due to the relative size of the electron, a wave-like description of the electron is necessary in order to properly describe its velocity and direction. In 1924, Louis de Broglie assumed that a moving mass behaves as a wave

$$\lambda = \frac{h}{p}$$

which can be written in terms of the wavenumber k as

$$k = \frac{p}{\hbar}$$

where k is defined as $k = \frac{2\pi}{\lambda}$, h is the Planck constant and p is the momentum of the particle. Applying de Broglie's theory, the wavenumber of the photoelectron is

$$k = \frac{\sqrt{2m_e E_e}}{\hbar}, \tag{1.18}$$

where $m_e$ is the mass of the photoelectron, and $E_e$ is the energy of the photoelectron.

The direction that the photoelectron travels away from the core atom is not exactly known, hence the photoelectron is treated as a spherical wave emitted from the core atom. If the core atom is the only atom in the system, such as a monatomic gas, the equation of this wave will be the free particle solution to the spherical Schrödinger equation. However, there are neighboring atoms to take into account. The wave of the photoelectron that scatters off of the nearby atoms creates new tiny spherical waves called backscattered waves. This is portrayed in Figure 1.10.

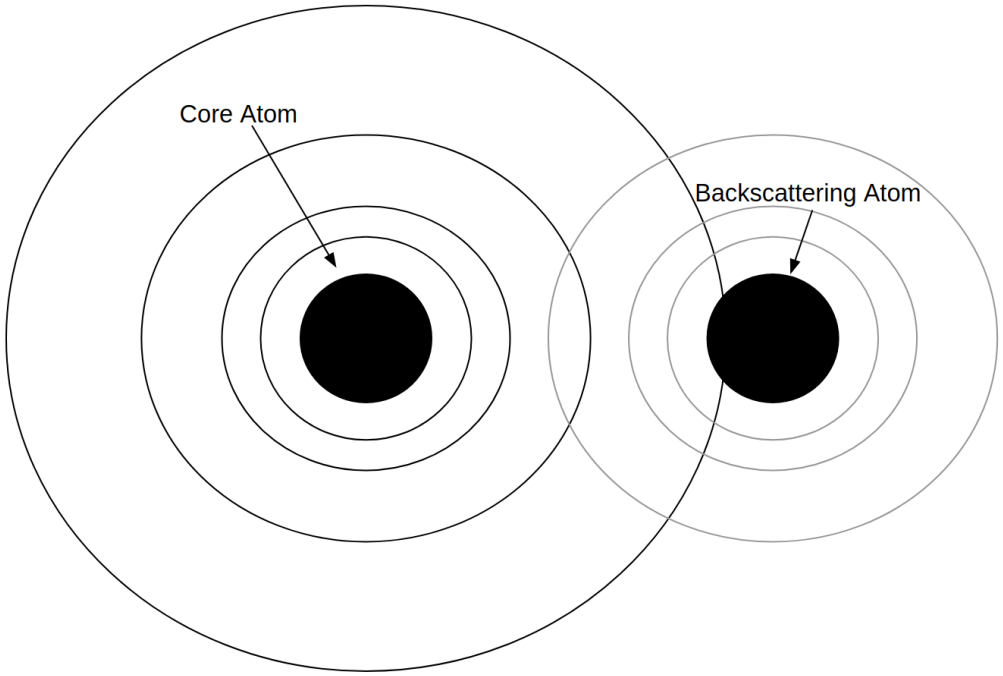


Figure 1.10: Wavefunctions of the outgoing photoelectron and the backscattered photoelectron. As an electron is ejected from an inner electron shell of its core atom, it may be described as a wavefunction. This is represented by the black circles emanating from the core atom. As the outgoing wavefunction scatters off of neighboring atoms, the wavefunction will reflect back towards the core atom. This is represented by the grey circles surrounding the backscattering atom.

This demonstrates that the wavefunction of the photoelectron will be a linear

combination of the outgoing wavefunction and all of the backscattered wavefunctions:

$$\Psi_{total} = \Psi_{outgoing} + \Psi_{backscattered}. \tag{1.19}$$

The outgoing wavefunction and all of the backscattered wavefunction will also be superimposed on each other. This will lead to interference between these wavefunctions at the absorbing atom. If the outgoing wave and the backscattered wave are in phase, the two waves will constructively interfere with each other and the amplitude of the total wavefunction will increase. If the ougoing wave and the backscattered wave are out of phase, the two waves will destructively interfere with each other and the amplitude of the total wavefunction will decrease. This interference is observed as oscillations after the absorption edge, which can be seen in Figure 1.2.

## 1.6 Einstein Model

The discussion below follows the Einstein model described in *The Oxford Solid State Basics* by Steven H. Simon.

In 1907, Albert Einstein came up with a quantum-mechanical model that describes properties of a solid state system. He assumed that each atom in the structure could be treated as a harmonic oscillator, where all of the atoms in the lattice oscillate at the same harmonic frequency, known as the Einstein frequency $\omega_e$.

A quantum simple harmonic oscillator in one dimension is known to have energy eigenstates of

$$E_n = \hbar\omega_e(n + 1/2)$$

where n $= 0, 1, 2, \ldots$ and $\omega_e$ is the Einstein frequency. Statistical mechanics states that the partition function all possible statistical ensembles of a system from which properties of the system, such as expectation energy and heat capacity, may be determined. The partition function for Einstein's model in one dimension is then

$$\begin{aligned} Z &= \sum_{n\geq 0} e^{-\beta E_n} = \sum_{n\geq 0} e^{-\beta\hbar\omega_e(n+1/2)} \\ &= \frac{e^{-\beta\hbar\omega_e/2}}{1 - e^{-\beta\hbar\omega_e}} = \frac{1}{2sinh(\beta\hbar\omega_e/2)}, \end{aligned}$$

where $\beta = \frac{1}{k_B T}$, $k_B$ is the Boltzmann constant.

The average energy of the system proposed by Einstein is given as

$$\langle E\rangle = -\frac{1}{Z}\frac{\partial Z}{\partial \beta} = \hbar\omega_e\Big(n_B(\beta\hbar\omega_e) + 1/2\Big), \tag{1.20}$$

where $n_B$ is the Bose factor

$$n_B(\beta\hbar\omega_e) = \frac{1}{e^{\beta\hbar\omega_e} - 1}.$$

The average energy in Eq. 1.20 may be rewritten as

$$\langle E\rangle = \frac{k_B\Theta_E}{2} coth\Big(\frac{\Theta_E}{2T}\Big), \tag{1.21}$$

where $\Theta_E = \frac{\hbar\omega_e}{k_B}$ is the Einstein temperature.

The EXAFS technique is interested in the Debye-Waller factor $\sigma^2$ to examine the average lattice vibrations between a pair of atoms. Assume an isolated pair of bound atoms where the bond between them may be represented by a spring with a spring constant $\kappa$. The total energy of this system is given as

$$E = \frac{1}{2}M_R v^2 + \frac{1}{2}\kappa x^2, \tag{1.22}$$

where $M_R$ is the reduced mass, $v^2$ is the velocity of the two atoms, $\kappa$ is the spring constant, and x is the variation in the bond length. The average energy of this system

is then

$$\langle E\rangle = \langle \frac{1}{2} M_R v^2 + \frac{1}{2}\kappa x^2 \rangle$$

$$\langle E\rangle = \langle \kappa x^2 \rangle = \kappa \langle x^2 \rangle$$

$$\langle E\rangle = \kappa \sigma^2. \tag{1.23}$$

The Debye-Waller factor is the ratio of the average energy of the system and the spring constant of the atomic pair. The Debye-Waller factor for the Einstein model is then

$$\sigma_E^2 = \frac{k_B \Theta_E}{2\kappa} coth\Big(\frac{\Theta_E}{2T}\Big). \tag{1.24}$$

This represents the temperature dependence of the mean square average of the difference of the displacement between atoms when fit to the Einstein model of a solid.

## 1.7 Debye Model

The discussion below follows the Debye model described in *The Oxford Solid State Basics* by Steven H. Simon.

In 1912, Peter Debye came up with a quantum mechanical model that was able to describe a solid state system better than the Einstein model, which came to be known as the Debye model. Debye assumed that vibrations of the atomic lattice, or phonons, may be treated as phonons in a box, such that the crystal is treated as many individual quantum oscillators. Each phonon has 3 modes of vibration ( 2 transverse modes and 1 longitudinal mode), where each mode has the same velocity. Debye also assumed that the system is periodic. This differs from the Einstein model, where Einstein assumed that all of the atoms have the same oscillation frequency.

Each wavevector $\vec{k}$ will have 3 vibrational modes. The average energy of the system is given as

$$\begin{aligned}\langle E\rangle &= 3\frac{4\pi L^3}{(2\pi)^3}\int_0^\infty d\omega \frac{\omega^2}{v^3}\hbar\omega\Big(n_B(\beta\hbar\omega)+\frac{1}{2}\Big)\\ &= \int_0^\infty d\omega g(\omega)\hbar\omega\Big(n_B(\beta\hbar\omega)+\frac{1}{2}\Big),\end{aligned}$$

where $g(\omega)$ is the density of states $g(\omega) = \frac{12N\pi\omega^2}{(2\pi)^3 n v^3}$, v is the velocity of the propagating wave, n is the density of atoms in the material, and $n_B(\beta\hbar\omega)$ is the Bose factor. The density of states contains the Debye frequency $\omega_d$, which is

$$\omega_d^3 = 6\pi^2 n v^3 \tag{1.25}$$

and the Debye Temperature $\Theta_D$ is

$$\Theta_D = \frac{\hbar\omega_d}{k_B}. \tag{1.26}$$

However, a phonon cannot have infinite energy. Debye stated that there should be as many modes as degrees of freedom in the system, or

$$3N = \int_0^{\omega_{max}} d\omega g(\omega),$$

where N is the number of atoms in the system and $\omega_{max}$ is the maximum frequency for the system. This will also allow a maximum energy for the system given by

$$\langle E\rangle = \int_0^{\omega_{max}} d\omega g(\omega)\hbar\omega\Big(n_B(\beta\hbar\omega) + \frac{1}{2}\Big) \tag{1.27}$$

The EXAFS technique is interested in the Debye-Waller factor $\sigma^2$ to examine the average lattice vibrations between a pair of atoms. The Debye-Waller factor was related to the average energy of the system in Eq. 1.23. Inserting the density of states equation and the Bose factor into the average energy for the Debye model, the Debye-Waller factor for the correlated Debye model is given as

$$\sigma_D^2 = \frac{\hbar}{2M_R}\int_0^{\omega_{max}} \frac{3\omega}{\omega_D^3} coth\Big(\frac{\hbar\omega}{2k_BT}\Big)\Big[1 - \frac{sin(\frac{\omega}{v}R_{ij})}{\frac{\omega}{v}R_{ij}}\Big], \tag{1.28}$$

where $M_R$ is the reduced mass, and $R_{ij}$ is the distance between atom pair $ij$. The

term in the brackets is known as the Debye correlation factor which determines if the two atoms move in phase, out of phase, or somewhere in between with respect to each other [4]. Eq. 1.28 represents the temperature dependence of the mean square average of the difference of the displacement between atoms when fit to the Debye model of a solid.

## 1.8 Extended X-ray Absorption Fine Structure

Extended X-ray Absorption Fine Structure (EXAFS) is a type of X-ray Absorption Spectroscopy (XAS) where the oscillations of the X-ray absorption coefficient above the absorption edge are studied [5].

As a collimated beam of monochromatic X-rays travels through a material, the intensity of the incident beam of X-rays decreases in intensity in proportion to the thickness of the material

$$dI = -\mu I dX, \tag{1.29}$$

where $dI$ is the infinitesimal change in intensity, $\mu$ is the constant of proportionality, known as the absorption coefficient, $I$ is the intensity of the incident collimated beam of monochromatic X-rays, and $dX$ is the differential thickness of the material. EXAFS is interested in measuring the absorption coefficient $\mu$, which is determined by integrating Eq. 1.29

$$\mu X = ln\Big(\frac{I_o}{I}\Big), \tag{1.30}$$

where $I_o$ is the incident X-ray intensity and $I$ is the transmitted X-ray intensity. This allows the absorption coefficient to be measure as a function of energy.

If there are no neighboring atoms, such as in a monatomic gas, the absorption edge monotonically decreases after the absorption process. If there are neighboring atoms, such as in a material, the photoelectron may scatter off of them in which the outgoing wave and the incoming backscattered waves interfere to cause constructive

and destructive interference, as discussed in Section 1.4. This results in an oscillation in $\mu$ that begin at the absorption edge. However, the oscillations 40 - 50 eV above the absorption edge is caused by a combination of single electron and multi-electron effects. The oscillations beyond 40 - 50 eV is primarily caused by single electron effect, which is needed for EXAFS. This region is called the fine structure.

The pre-edge contains absorption below the edge from other atoms that have no structure. The region that includes the pre-edge through the oscillations 40 - 50 eV above the absorption edge is known as the X-ray Absorption Near Edge Structure (XANES) that is sensitive to electronic structure, as well as to other structures, around the edge region. XANES partially overlaps with the beginning of the fine structure typically around 40-50 eV above the absorption edge. XANES studies the electronic structure of a material by examining the empty electron states near the Fermi level.

In EXAFS, the variation of the absorption coefficient $\Delta\mu(E)$ from the background absorption coefficient $\mu_o(E)$ is of interest. The background absorption coefficient is the non-oscillatory part of the absorption coefficient that would be present if there were no backscattering. This variation in the absorption coefficient is then normalized by the background absorption coefficient and is given by

$$\chi(E) = \frac{\mu(E) - \mu_o(E)}{\mu_o(E)}. \tag{1.31}$$

The probability that a photon will excited an electron from an initial state $i$ to a

final state $f$ is determined by the use of Fermi's Golden Rule, in which the absorption coefficient is proportional to

$$\mu \sim | < f|\hat{\epsilon} \cdot \vec{r}|i > |^2, \tag{1.32}$$

where $\hat{\epsilon}$ is the polarization vector of the electric field of the incident X-rays, and $\vec{r}$ is the position of the electron. The initial state $i$ is the localized bound energy state of a core electron, and the final state $f$ is the corresponding ejected photoelectron and the excited atom. $\chi(E)$ is converted from energy space to k space, since the waves describing the photoelectron are in terms of the photoelectron's wavevector, as shown in Eq. 1.18. $\chi(k)$ is then written as

$$\chi(k) = S_o^2 \sum_i \frac{|F_i(k)|}{kr_i^2} e^{-2r_i/\lambda(k)} e^{-2k^2\sigma_i^2} sin(2kr_i + \phi_{ij}(k)). \tag{1.33}$$

The above equation, known as the EXAFS equation, is in a simplified form in which the $\frac{1}{r^2}$ term is fixed over the width of a symmetric Gaussian distribution of distances, which results in the exponentially dampening term $e^{-2k^2\sigma_i^2}$. The EXAFS equation was first derived by Sayers, Stern, and Lytle in 1971 where they assume that the atoms in the substance acted as point scattering sources [6]. Other formal derivations of the EXAFS equation have been achieved that investigates different properties that spawn from the EXAFS formula [7] [8]. The terms in Eq. 1.33 are explained in the paragraphs below.

$S_o^2$ is an amplitude reduction factor that accounts for multiple electrons processes. When an x-ray is absorbed by an electron, the electron does not always leave the core atom without interacting with the surrounding electrons. The initial electron may interact with another electron and cause it to be excited to a higher bound energy level. This is known as a shake up process. The initial electron may interact with another electron and have enough energy to completely eject that electron as well, which is known as a shake off process. Both processes cause a reduction in the amplitude for the wavenumber $k$ of the photoelectron of interest, which leads to $\mathrm{S}_o^2$ to be less than one. This results in an overall reduction to the EXAFS signal.

The summation over the index $i$ takes into account every possible scattering path. If the same scattering path occurs more than once, it would be the same value added each time that it occurs. $S_o^2$ is taken out of the summation because the multiple electron processes only pertain to the core atom.

The $\frac{1}{r_i^2}$ factor is a result from the assumption of wavefunction of the photoelectron to be spherical. $r_i$ is taken to be the distance from the core atom to the i$^t h$ neighboring atom.

The function $F_i(k)$ is known as the backscattering amplitude. This function represents the fraction of backscattered photoelectron's wave that travels back to the core atom. The backscattering amplitude depends on the wavenumber of each unique backscattered wavefunction.

The first exponential term, $e^{-2r_i/\lambda(k)}$, takes into account the lifetime of the hole created by the photoelectron. It also takes into account inelastic scattering processes

that contribute to a reduction in the overall EXAFS amplitude. The term $\lambda(k)$ is the mean free path of the photoelectron. The photoelectron may interact with electrons that belong to the core atom, as well as interact with electrons that pertain to the neighboring atoms. This term also takes into account the lifetime of the hole created by the photoelectron.

The Debye-Waller factor $\sigma$ holds valuable information that pertains to the structure of the crystal. The Debye-Waller factor is the root mean square average of the difference of displacement from the average distance between atoms, or the amount of disorder as it deviates from a perfect crystal. It contains a component that describes the static disorder of the system and a component that describes the disorder due to thermal vibrations. Only temperature dependent EXAFS measurements are able to separate the static contribution from the vibrational component. It is defined as

$$\sigma^2 = \sigma^2_{stat} + \sigma^2_{vib}, \tag{1.34}$$

where $\sigma^2_{stat}$ models the static disorder, and $\sigma^2_{vib}$ models the thermal vibrations of the system. The temperature dependence of the Debye-Waller factor could be fit to both the Einstein model and the Debye model, which is discussed in Section 1.6 and Section 1.7, respectfully. The temperature dependence of the Debye-Waller factor could be fit to the Einstein model and to the Debye model – i.e. using Eq. 1.24 for the Einstein model or Eq. 1.28 for the Debye model.

## 1.9 History of $URu_2Si_2$

$URu_2Si_2$ was first analyzed by Schlabitz et al. (1984), with the results originally posted on an unpublished poster, which sparked interest in the substance [10]. The heavy-fermion material $URu_2Si_2$ has a simple tetragonal crystal structure whose space group is I 4/mmm, which is shown in Figure 1.11. It was found that $URu_2Si_2$ was the first material where both superconductivity and a magnetic moment coexist, in which both require the U 5f electrons [11].

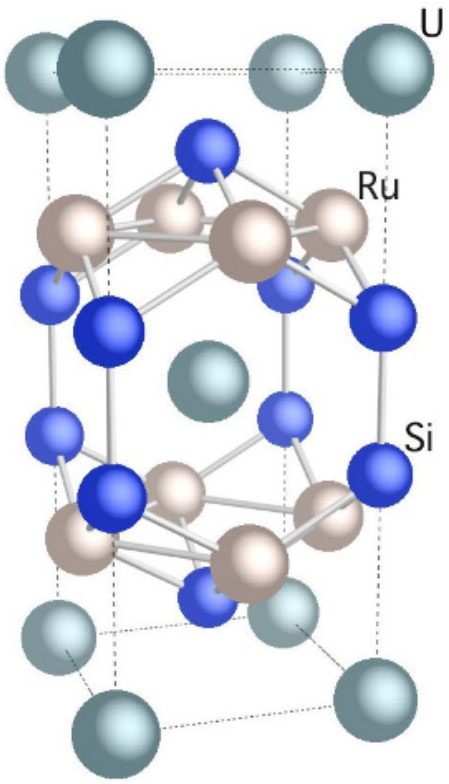


Figure 1.11: Unit cell of $URu_2Si_2$. It has a tetragonal crystal structure with a I / 4mmm space group. The green spheres represent U atoms, the blue sphere represent Si atoms, and the grey represent Ru atoms. The a-axis is in the direction of the shortest U-U bond, as with the b-axis, but perpendicular to the a-xis. The c-axis is perpendicular to both the a-axis and b-axis.

Shortly after this poster, two other groups found an interest in $URu_2Si_2$. All three of these research groups agreed that there was a magnetic transition from a paramagnetic phase to another magnetic phase around 17.5 K, with a corresponding large decrease entropy 0.2Rln(2) that is shown in Figure 1.12, as well as a superconducting phase transition that occurs around 1 K [11, 12, 13].

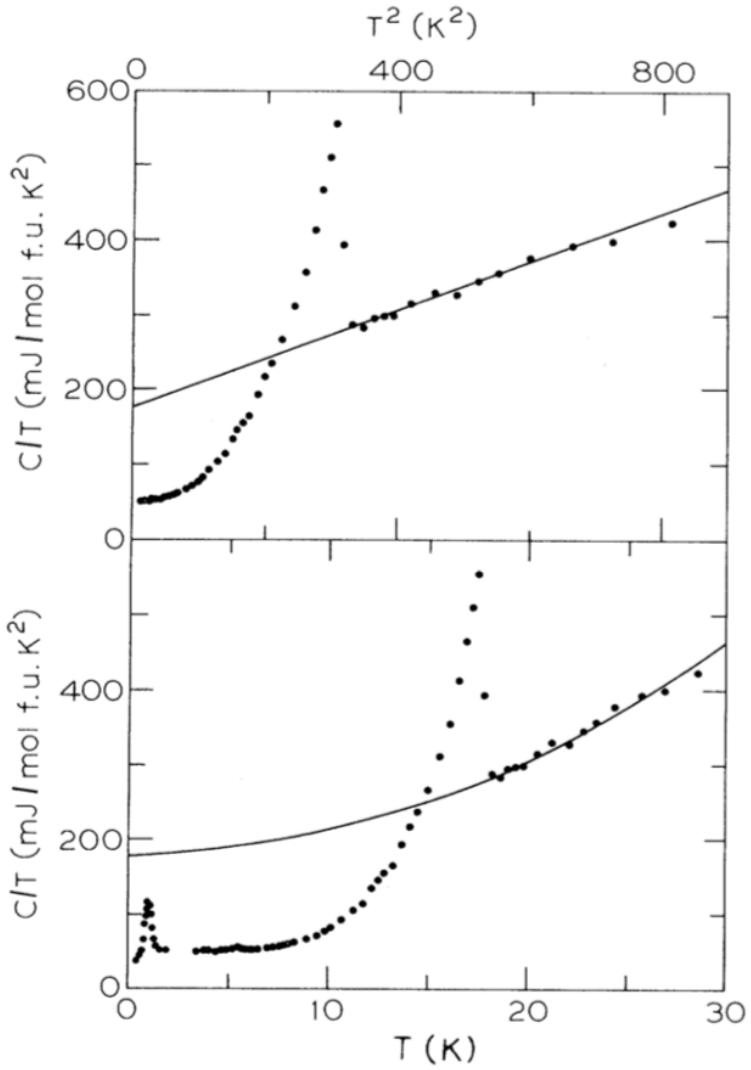


Figure 1.12: Specific heat of $URu_2Si_2$ taken from Palstra et al. (1985). The top plot shows C/T vs $T^2$ and the bottom plot shows C/T vs T [12].

However, they all had different hypotheses for the magnetic phase transition that occurs at 17.5 K. Schlabitz et al. (1986) suggested that an antiferromagnetic phase transition occurs around 17.5 K due to localized U 5f - electrons [11]. Palstra et al. (1985) hypothesized that the magnetic phase transition at 17.5 K is a weak type of antiferromagnetism [12]. Maple et al. (1986) suggested that the transition occurred to do either a spin-density wave (SDW) or a static charge density wave (CDW) [13]. Further investigation by Broholm et al. (1987) and Isaacs et al. (1990) found that this magnetic phase transition at 17.5 K under ambient pressure had a significantly small U magnetic moment of $0.03 \pm 0.01\mu_B$ and $0.02 \pm 0.01\mu_B$, respectively [14, 15].

It is now known that these three hypotheses are not correct. The order parameters of this mysterious phase transition at 17.5 K are still unknown; The term hidden order (HO) was adopted for the unknown phase that the paramagnetic phase transitions to. Recent work by Booth et al. (2016) discovered that the U 5f - electrons are partially delocalized with an occupancy $n_f \sim 2.87$, which stays consistent from 10 K to 300 K, by Resonant X-ray Emission Spectroscopy (RXES) [16]. This result is consistent with the lack of significant U magnetic moment at low temperatures. Butch et al. (2015) investigated this small U magnetic moment by neutron scattering and found that it remain constant to low temperatures, which indicates a hybridization between U f - electron states and conduction electrons [17]. Wray et al. (2015) discovered that excited electrons in the U f-shell have symmetric properties by X-ray absorption spectroscopy measurements and high-resolution resonant inelastic X-ray scattering measurements [18]. The electrons pertaining to the U $f^2$ shell behave as a doublet $\Gamma_5$

crystal field state of U [18].

The HO phase transition of $URu_2Si_2$ was also measured in high magnetic fields and high pressure environments. De Boer et al. (1986) found out that the transition to the HO phase does not occur at magnetic fields greater than around 36 T [19]. Instead, $URu_2Si_2$ transitions from its paramagnetic phase directly into a large moment antiferromagnetic (LMAFM) phase. Amitsuka et al. (1999) investigated the pressure dependence of $URu_2Si_2$ up to 2.5 GPa by examining the Bragg peaks created by neutron scattering. It was determined that around 0.5 GPa, the HO phase gives way to the LMAFM phase, where the U magnetic moment greatly increased from around $0.03\mu_B$ to $0.4\mu_B$ [20].

It was found that similar effects to that caused by an increase in pressure occur when Fe is chemically substituted on the Ru site while remaining at ambient pressure, known as a chemical pressure. This presents an opportunity to investigate both cases to determine the differences between the HO phase and the LMAFM phase. In 2011, Kanchanavatee et al. took specific heat, resistivity, and magnetization measurements on $URu_{2-x}Fe_xSi_2$ where the concentration x varied from x=0.00 to x=2.00. The difference in entropy increases until it reaches a maximum entropy around x= 0.20. After that point, the difference in entropy decreases, which Kanchanavatee et al. suggest that the HO phase possibly transitions to the LMAFM phase [21]. This is shown in Figure 1.13.

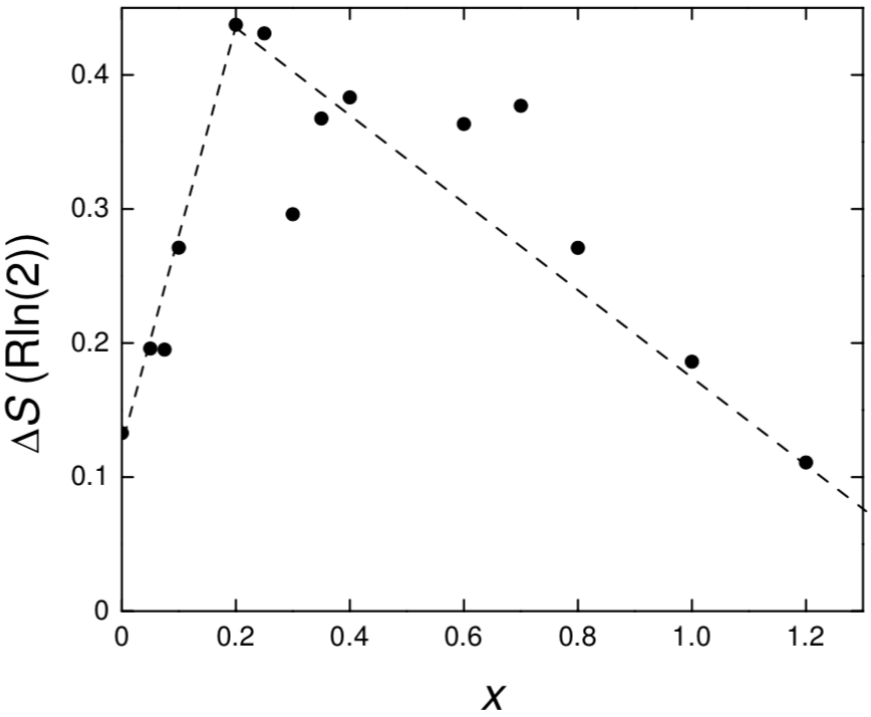


Figure 1.13: The difference in entropy $\Delta S$ between the paramagnetic phase and the HO phase vs Fe concentration x [21]. The peak at x= 0.2 followed by a decrease in $\Delta S$ suggests that the HO phase gives way to the LMAFM phase.

Ran et al. (2016) constructed a T - x phase diagram for $URu_{2-x}Fe_xSi_2$ which depicts a relation between the PM phase, LMAFM phase, and the HO phase in the absence of a magnetic field. The HO phase gave way to the LMAFM phase above x$\sim$0.15 based on the difference of entropy between the paramagnetic phase and the HO phase. The LMAFM phase was determined to be stable when the Fe concentration was around x=0.10, where the HO phase transition occurs without entering the LMAFM phase with a Fe concentration below x$\approx$0.07, which is shown in Figure 1.14 [22].

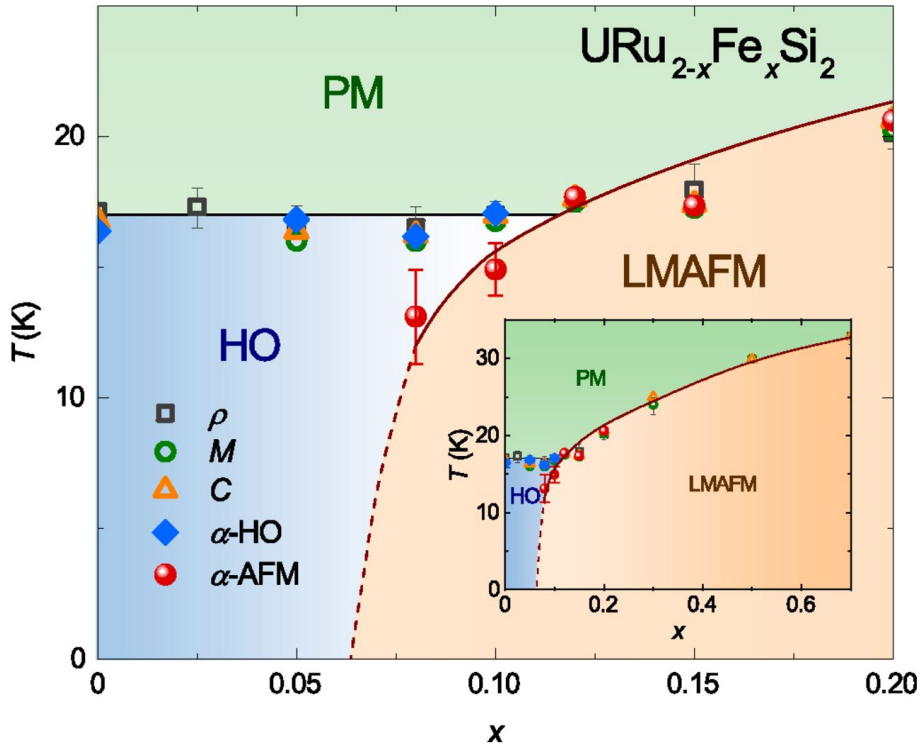


Figure 1.14: T - x phase diagram of $URu_{2-x}Fe_xSi_2$ in the absence of a magnetic field created by Ran et al. (2016) [22].

Ran et al. (2017) took electrical transition measurements of $URu_{2-x}Fe_xSi_2$ in DC magnetic fields up to 45 T and pulsed magnetic fields up to 60 T. Unlike Kanchanavatee et al., the reentrance of the HO phase at x=0.15 and x=0.20 was noticed, where Ran et al. suggest that the LMAFM is suppressed [23]. A 3 dimensional phase diagram of temperature T vs Fe concentration x vs magnetic field H was created by Ran et al. (2017), which shown in Figure 1.15.

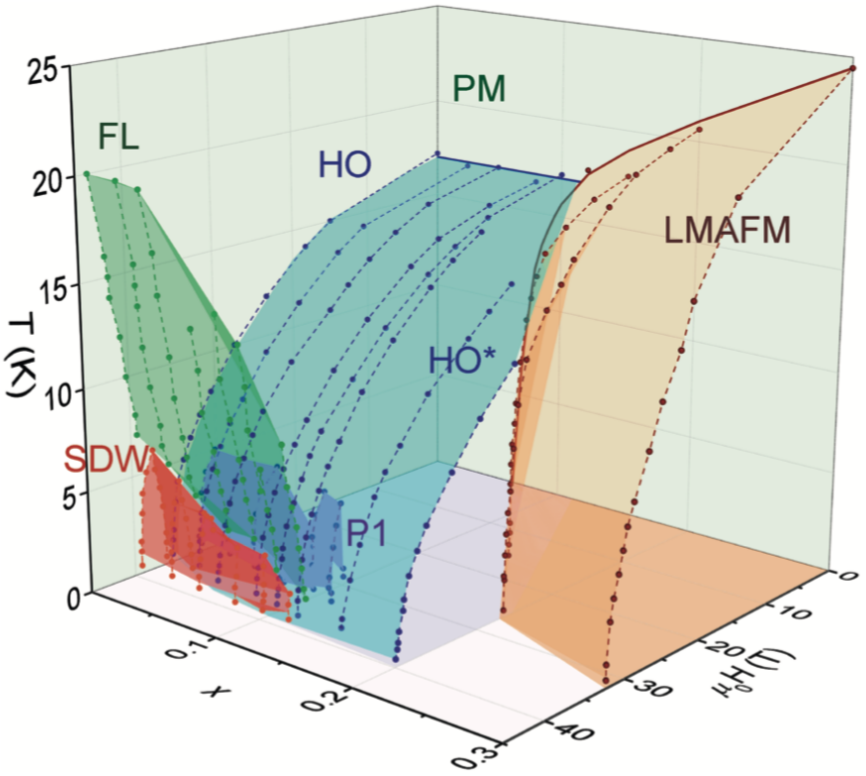


Figure 1.15: Phase diagram of $URu_{2-x}Fe_xSi_2$ created by Ran et al. (2017). The three axis are temperature T, Fe concentration x, and magnetic field H, where the magnetic field was applied along the c-axis of the material [23]. The HO label represents the hidden order phase. The HO* label represents the reentry of the hidden order phase. The LMAFM label represents the large moment antiferromagnetic phase. The PM label represents the paramagnetic phase. The FL label represents the field-induced recovery of the normal metallic phase. The SDW label represents the occurance of spin density waves. The P1 label represents a possible new phase [23].

In Figure 1.15, presented by Ran et al. (2017), there is an overlap of the HO phase and LMAFM phase around x≈0.07 with no magnetic field, which then increases to x≈0.20 as the magnetic field increases.

# Chapter 2

# Data Collection Methods

This chapter will discuss the experimental methods used to collect data and the process of converting the data from energy space to real space by EXAFS analysis. The data were collected at the Stanford Synchrotron Radiation Lightsource (SSRL). Synchrotron radiation is radiation emitted from radially accelerated charged particles traveling at relativistic speeds [24]. Two types of data collection methods were used, transmission and fluorescence, in order to measure the absorption coefficient $\mu$ as a function of energy of a particular atom in the material of interest. The data collected from each collection method is in energy space, or in units of energy (eV).

## 2.1 Creation of Monochromatic X-rays

Synchrotrons emit a continuous spectrum of X-rays, where the emitted X-rays are polarized in the plane of the synchrotron ring [24]. A monochromator is used to select

a specific energy of X-rays from a synchrotron and are typically two silicon crystals. Each of the two crystals are cut parallel to one of their common lattice planes and are placed in the path of the incoming X-rays prior to reaching the sample. This allows for X-rays that satisfy Bragg's law to only pass through the monochromator.

An issue is that Bragg's law allows for multiple orders to exist, due to the integer $m$. This will allow the monochromator to pass higher order harmonics, where $m > 1$, to be transmitted. In order to reject higher harmonics with m $> 1$, one of the crystals in the monochromator could be slightly rotated so that it is no longer parallel to the other crystal. The rotation of one of the crystals allows for both of the crystals to satisfy Bragg's law with m=1, but one of the two crystals will not satisfy Bragg's law for higher harmonics [5]. This set up is shown in Figure 2.1.

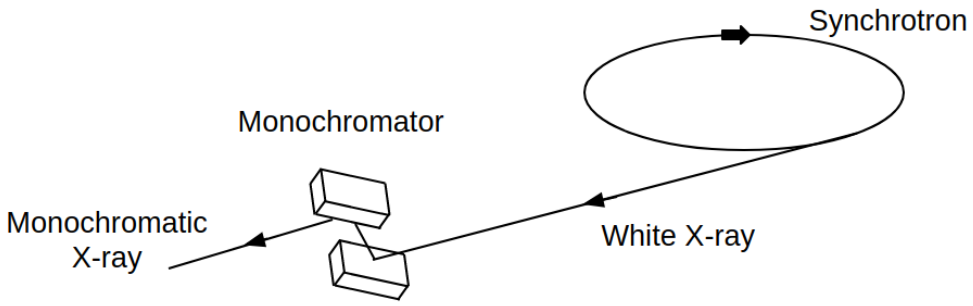


Figure 2.1: Production of monochromatic X-rays from a synchrotron. As X-rays are emitted from the synchrotron, they encounter a monochromator that consists of two parallel crystals. The crystals act as a family of lattice planes, in which only wavelengths that satisfy Bragg's law are transmitted. One of the crystals may be slightly rotated to only allow the lowest harmonic $m = 1$ through.

## 2.2 Transmission Data Collection

In an EXAFS transmission experiment, the intensity of monochromatic X-ray beam prior to and after the sample is measured in order to determine the absorption coefficient as a function of energy, which is given by Eq. 1.30. The intensity $I_o$ is the intensity that is measured before the sample, and the intensity $I_1$ is the intensity measured after the monochromatic X-ray beam is transmitted through the sample. The intensity of the monochromatic X-ray beam is measured by the ionization of gas in the detector.

The sample of interest is placed inside of a cryostat where a continuous flow of liquid helium maintained the sample at some set temperature between 10 K and 300 K. Another sample, known as a reference sample, is placed in the path of the monochromatic X-ray beam between the second detector $I_1$ and the third detector $I_2$, which is beyond the reference sample. The reference sample used to compare to the U $L_{III}$ edge was uranium oxide $UO_2$. The reference sample used to compare to the Ru K edge was Ru foil. The third detector measures the intensity of X-rays $I_2$ that are transmitted through the reference sample. The absorption coefficient of the reference sample is given by

$$\mu_{ref} X_{ref} = ln\Big(\frac{I_1}{I_2}\Big), \tag{2.1}$$

where $\mu_{ref}$ is the absorption coefficient of the reference sample, $X_{ref}$ is the thickness of the reference sample, $I_1$ is the intensity of the monochromatic X-rays prior to the

reference sample, and $I_2$ is the intensity of the monochromatic X-rays after they are transmitted through the reference sample. The purpose of the reference sample is to determine if the energy of the monochromatic X-ray is drifting slowly with time by comparing the absorption coefficient of the reference sample with all scans of the sample of interest. Figure 2.2 shows the experimental set up for transmission EXAFS data collection.

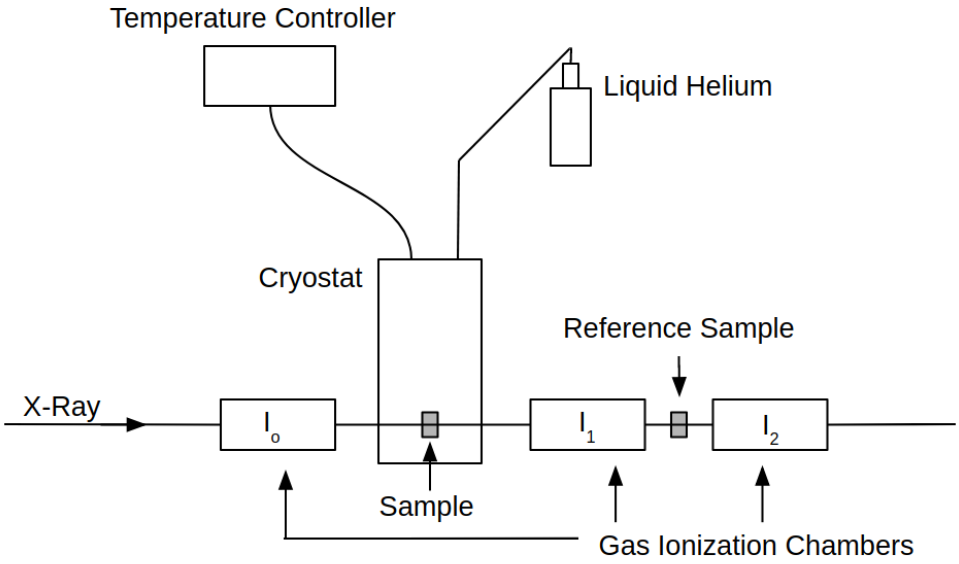


Figure 2.2: Experimental set up for transmission mode. The sample is placed in the cryostat and is perpendicular to the incoming beam of monochromatic X-rays. A continuous flow of liquid helium is able to maintain the sample at low temperatures. A reference sample is used in order to determine if the energy of the incoming monochromatic X-rays is changing. Three gas ionization chambers are used to measure the absorption coefficient of the sample and the reference sample.

The data for the U $L_{III}$ edge and the Ru K edge of $URu_{2-x}Fe_xSi_2$ were collected in transmission mode with the following concentrations x of Fe doped on the Ru site: x=0.00, x=0.05, x=0.08, x=0.10, x=0.12, x=0.15, and x=0.20. These two edges had

data collected in 3 scans at specific temperatures that range from around 10 K to 300K, with most of the data taken at low temperature in order to investigate the HO at 17.5 K.

However, due to limited beamtime, we were not able to collect data for all concentrations. For the U edge, the samples with concentrations of x=0.05 through x=0.15 have data up to 300 K. The concentration x=0.20 concentration around 10 K had four runs of data collection done, and the x=0.15 concentration at 300K only had one run of data collection. For the Ru edge, samples with the concentrations of x=0.00, x=0.08, and x=0.15 only have data up to 300 K.

## 2.3 Fluorescence Data Collection

EXAFS fluorescence experiments are used when the absorption edge height of the atom of interest is too small, usually around 0.1 to 0.15, in which case the signal for EXAFS transmission experience will contain enough noise that leads to poor data. The samples that EXAFS fluorescence experiments are performed on have a low concentration of the atom of interest. The intensity of the fluorescence that is measured is due to the radiation emitted when a higher energy state electron fills a hole left by the photoelectron.

The sample is rotated by 45° with respect to the monochromatic X-ray beam. The fluorescence detector is set next to the sample, but perpendicular to the monochromatic X-ray beam. The fluorescence does not have to pass through the fluorescence detector, so a solid state detector could be used to measure the fluorescence intensity $I_F$. The fluorescence signal F for fluorescence data collection, which is related to the absorption coefficient, is given by

$$FX = \frac{I_F}{I_o} \approx \mu X. \tag{2.2}$$

Figure 2.3 shows the experimental set up for fluorescence EXAFS data collection.

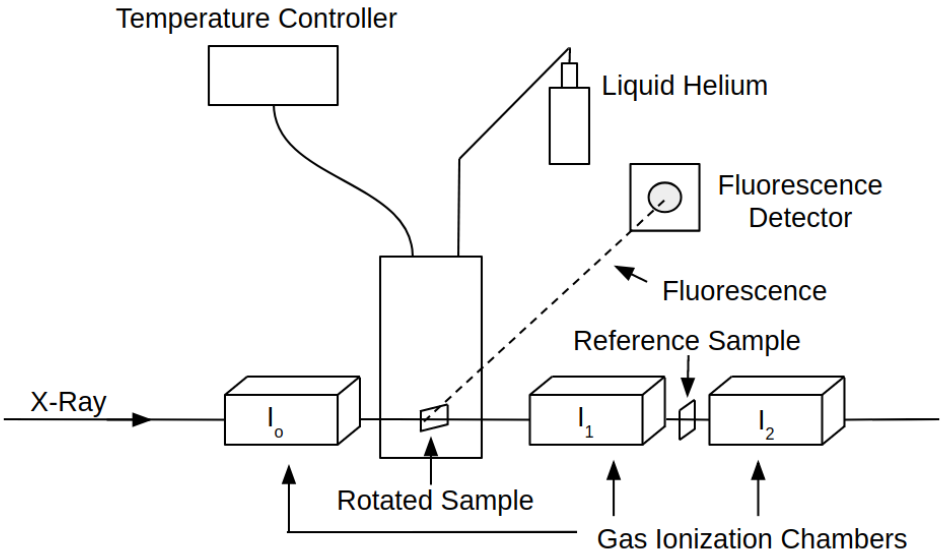


Figure 2.3: Experimental set up for fluorescence mode. The sample is placed in the cryostat, but rotated 45° with respect to the incoming monochromatic X-rays. A continuous flow of liquid helium is able to maintain the sample at low temperatures. Fe foil is used as the reference sample for the Fe K edge in order to determine if the energy of the incoming monochromatic X-rays is varying. Three gas ionization chambers are used to measure the absorption coefficient of the sample and the reference sample.

The data for the Fe edge were collected in fluorescence mode with the following concentrations of Fe doped on the Ru site: x=0.05, x=0.08, x=0.10, x=0.12, x=0.15, and x=0.20. This edge had data collected in 3 scans at set temperatures that range from around 10 K to 300K, with most of the data taken at low temperature in order to investigate the HO at 17.5 K.

# Chapter 3

# Theoretical Calculations

The variation of the absorption coefficient $\chi(k)$ may be theoretically calculated through a program called FEFF. FEFF determines the F(k) portion of the EXAFS function (Eq. 1.33), or the effective backscattering amplitude, the phase shift $\phi(k)$, as well as the mean free path of the photoelectron $\lambda(k)$. The other variables in the EXAFS equation turn into parameters in other fits (Chapter 5).

FEFF must be given the basis of the unit cell of the material of interest, as well as a maximum distance that tells the program how many atoms to consider for each $\chi(k)$ function. This necessary information is provided by an input file that designated an atom as a core atom. This core atom will represent the atom from which the photoelectron is emitted from.

Once FEFF has the correct information, it determines all possible scattering paths; this is known as a path expansion approximation. This treats the first order terms as the photoelectron scattering off of only one atom, second order terms as the pho-

toelectron scattering off of two atoms, and so on. These are known as legs, where the direct scattering off of one atom is a 2-leg path. FEFF keeps up to 4-leg paths in order to acquire an accurate calculation of $\chi(k)$.

The backscattering amplitudes are determined for each path. The output of FEFF is written in terms of many individual $\chi(k)$ functions, each corresponding to possible photoelectron scattering path that surrounds the core atom. These separate $\chi(k)$ functions are known as theoretical standards. These standard files are used to fit to the data, since they theoretical predict what $\chi(k)$ should look like where there would be no systematic disorder or multiple electron effects. This corresponds to $S_o^2 = 1$ and $\sigma = 0$ in the EXAFS equation shown by Eq. 1.33.

A simulation for each measured atomic edge was created by accounting for every standard and performing a Fourier transform over the same correspond k-space range so they may be compared to the data collected. The k-space range for each edge are given in Chapter 4. Appendix A shows each theoretical simulation in r-space for each edge, as well as each individual theoretical standard file that were used to fit each corresponding absorption edge.

# Chapter 4

# Data Reduction Procedure

This chapter will present the raw data of each investigated absorption edge in e-space. A program called REDUCE was used to convert the data into k-space and transform the data into r-space. The reduction process of each absorption edge will be discussed. The theory behind this is discussed in Section 1.8.

## 4.1 Transmission Data Reduction

The data for the Ru K edge and the U $L_{III}$ edge of $URu_{2-x}Fe_xSi_2$ were collected in transmission mode, as discussed in Section 2.2. Each absorption edge was observed at various set temperatures that ranged from around 10 K to 300 K, with most of the data focused in the low temperature region to investigate the HO phase. Figure 4.1 shows the U $L_{III}$ edge taken at 4 K with a Fe concentration x=0.00.

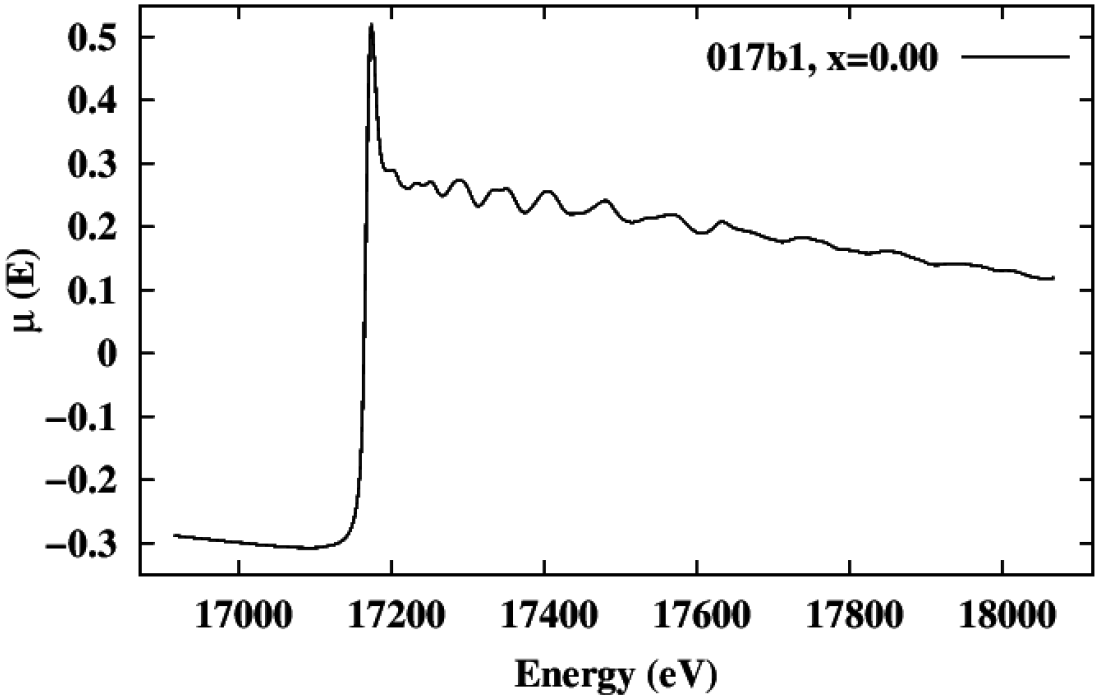


Figure 4.1: U $L_{III}$ absorption edge transmission data with no Fe concentration taken at 4 K.

Due to the experimental setup, the absorption edge of interest is not measured exactly. There are contributions from absorption effects from other atoms in the sample, the apparatus, and even from the air in between the cryostat and the detectors. These contributions are known as background effects and must be removed from the data set as best so the absorption edge of interest may be properly investigated. A polynomial is fit to the pre-edge data and is constrained above the edge using the Victoreen formula so that after this fit is subtracted the slope of $\mu(E)$ has the correct value. The Victoreen formula is given as

$$\mu = C\lambda^3 - D\lambda^4, \tag{4.1}$$

where $\lambda$ is the wavelength of the X-ray, and the coefficients C and D are known as Victoreen's coefficients. These are each based on the atomic number of the atom of interest, and they allow for the calculation of the energy dependence of specific absorption edges, such as a K edge or an L edge. This determines the slope that the data should have once all background contributions have been removed. The values for various Victoreen coefficients may be found in Appendix III of *EXAFS: Basic Principles and Data Analysis* by Boon K. Teo (1986). The pre-edge fit for the U $L_{III}$ edge is shown in Figure 4.2.

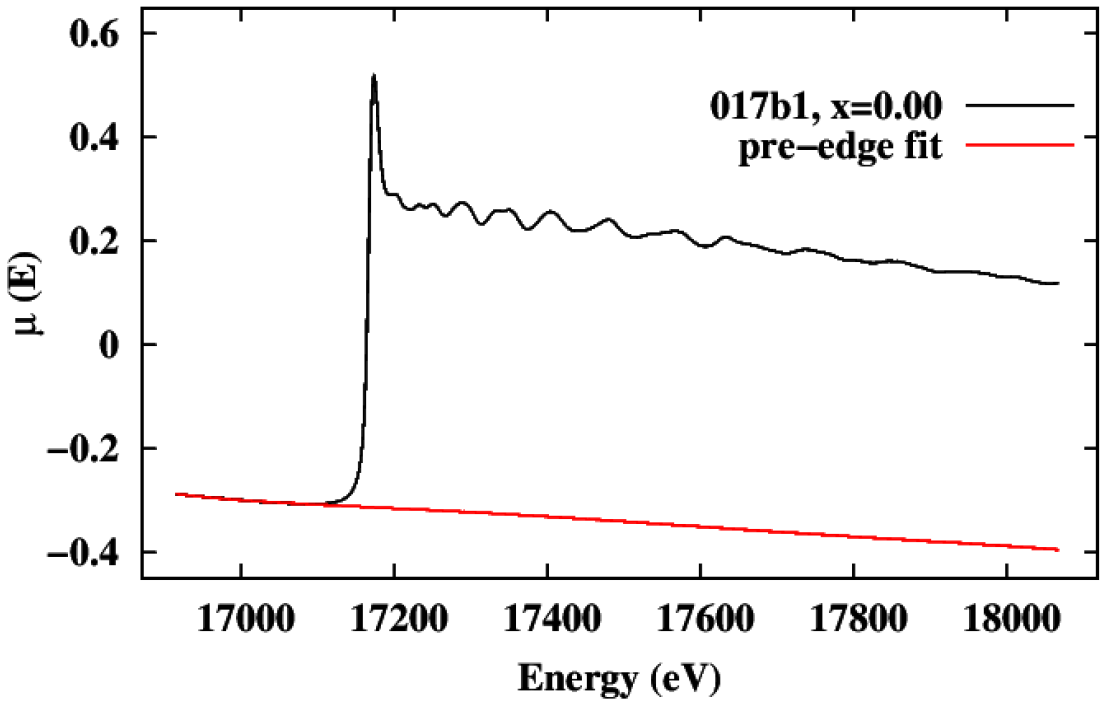


Figure 4.2: U $L_{III}$ absorption edge transmission data (black line) with no Fe concentration taken at 4 K. The pre-edge was fit to a polynomial from 16914 ev to 17060 ev and constrained above the edge using the Victoreen formula (red line).

The solid black line in Figure 4.2 represents the entire transmission data collected

for the U $L_{III}$ edge at 4 K with no Fe concentration. The solid red line in Figure 4.2 depicts the constrained Victoreen fit of the edge from 16914 eV to 17060 eV: the extrapolation above the edge is constrained to have the correct slope using the Victoreen equation.

The resulting data are then normalized to unity by the division of $\Delta\mu$(E) =$\mu$(E) - $\mu_b$(E) by the step height of the absorption edge $\mu_{E'}$, where $\mu_b(E)$ is the background absorption and is depicted as the red line in Figure 4.2. Figure 4.3 shows the normalized U $L_{III}$ edge at 4 K with no Fe concentration.

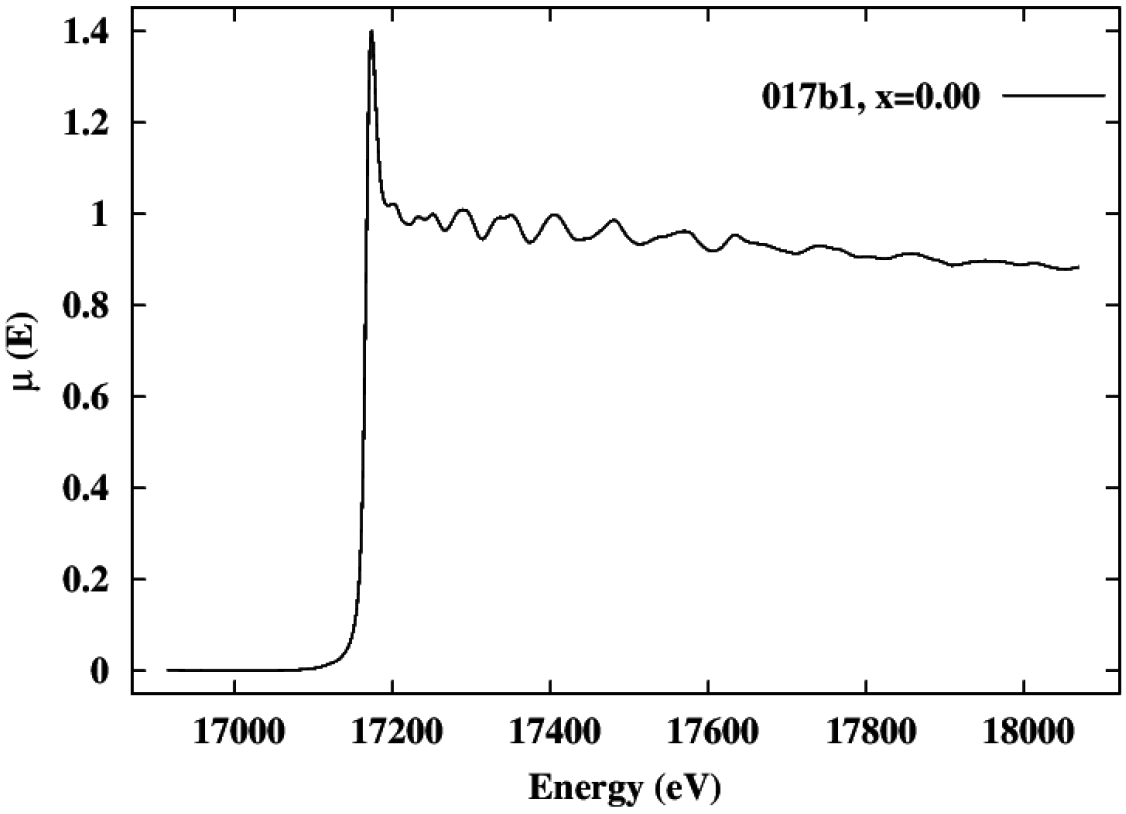


Figure 4.3: Normalized U $L_{III}$ absorption edge transmission data with no Fe concentration taken at 4 K. The background contribution at the pre-edge had been removed.

Once the background contribution had been subtracted from the pre-edge and the

data set had been normalized, another fit occurs to a region above the edge based (post-edge) on the expected slope that should be present in that region in order to extract the EXAFS oscillations $\chi$(E), where

$$\mu(E) = \mu_o(E)(1 + \chi(E)). \tag{4.2}$$

$\mu_o(E)$ is the smooth background with no fast oscillations in the EXAFS region and is represented by the red line in Figure 4.4.

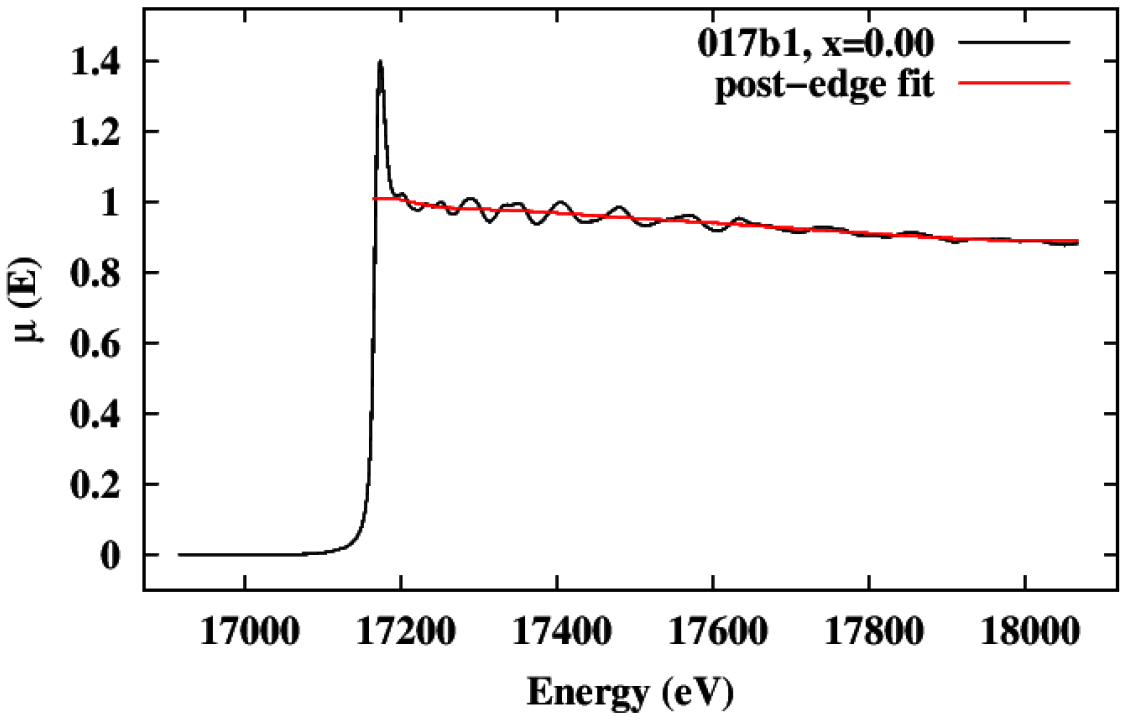


Figure 4.4: Normalized U $L_{III}$ absorption edge transmission data with no Fe concentration taken at 4 K is shown as the solid black line. The post-edge fit to high energy region is shown as the solid red line.

The extracted function $\chi$(E) was then converted into k-space by

$$k = \sqrt{\frac{2m_e}{\hbar^2}(E - E_o)}, \tag{4.3}$$

where E is the energy of the incoming X-ray beam, $E_o$ is the binding energy of one of the inner shell electrons, and $m_e$ is the mass of the photoelectron. This results in $\chi$ as a function of the wave vector k. $\chi(k)$ is often multiplied by k to some power, $k^n\chi(k)$, to amplify high k data if the signal-to-noise ratio is good. This results in the amplitudes of the oscillations to be nearly constant with k, and generates the sharpest possible peaks in r-space. For the U $L_{III}$ edge, $k = 1$ with a power of 1 was chosen. The k-space conversion of the U $L_{III}$ edge with all concentrations at 4 K is shown in Figure 4.5 below.

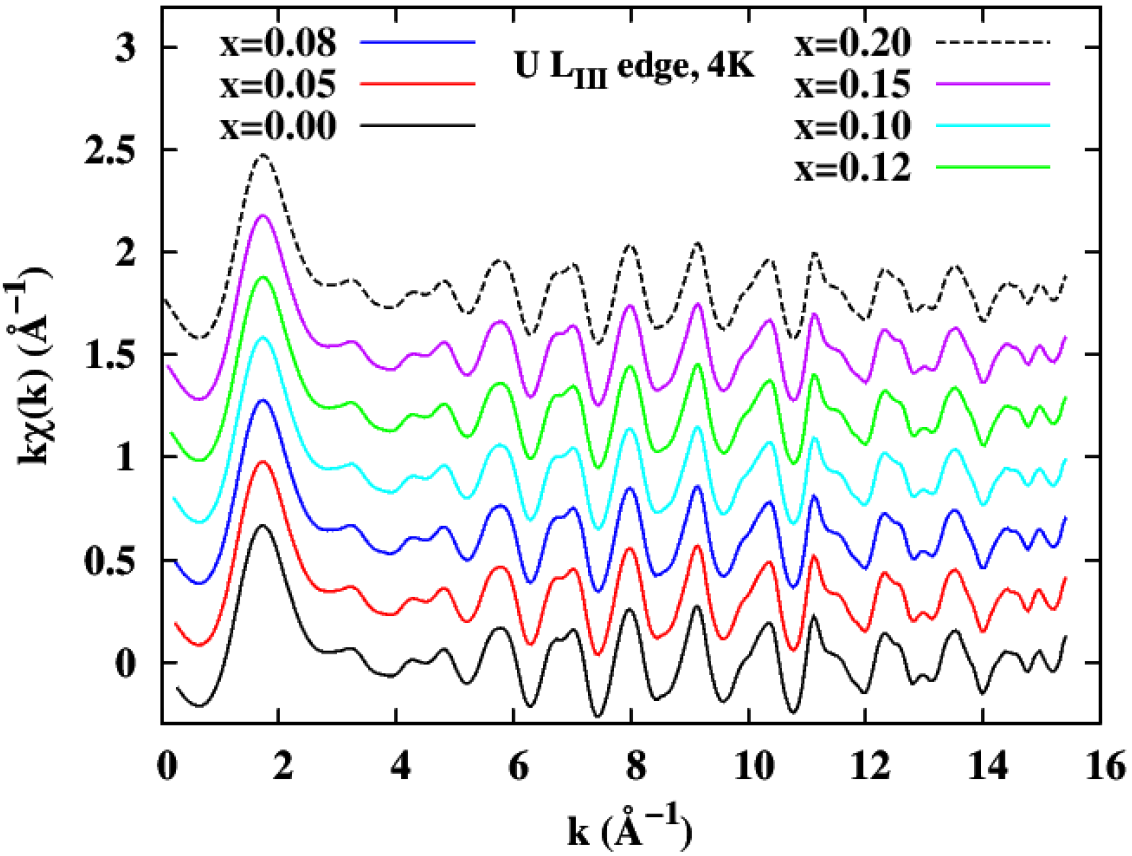


Figure 4.5: U $L_{III}$ absorption edge transmission data converted into k-space. The data depicted were taken at 4 K.

Once the data are converted from e-space to k-space, a Fourier transform was performed on $k^n\chi(k)$ over a finite k range [6]. The Fourier transform of $k^n\chi(k)$ of the U $L_{III}$ edge was performed over a k-space range from 3.5 Å$^{-1}$ to 14.8 Å$^{-1}$. Figure 4.6 shows these Fourier transforms of $URu_{2-x}Fe_xSi_2$ at various set temperatures with a Fe concentration of x=0.05.

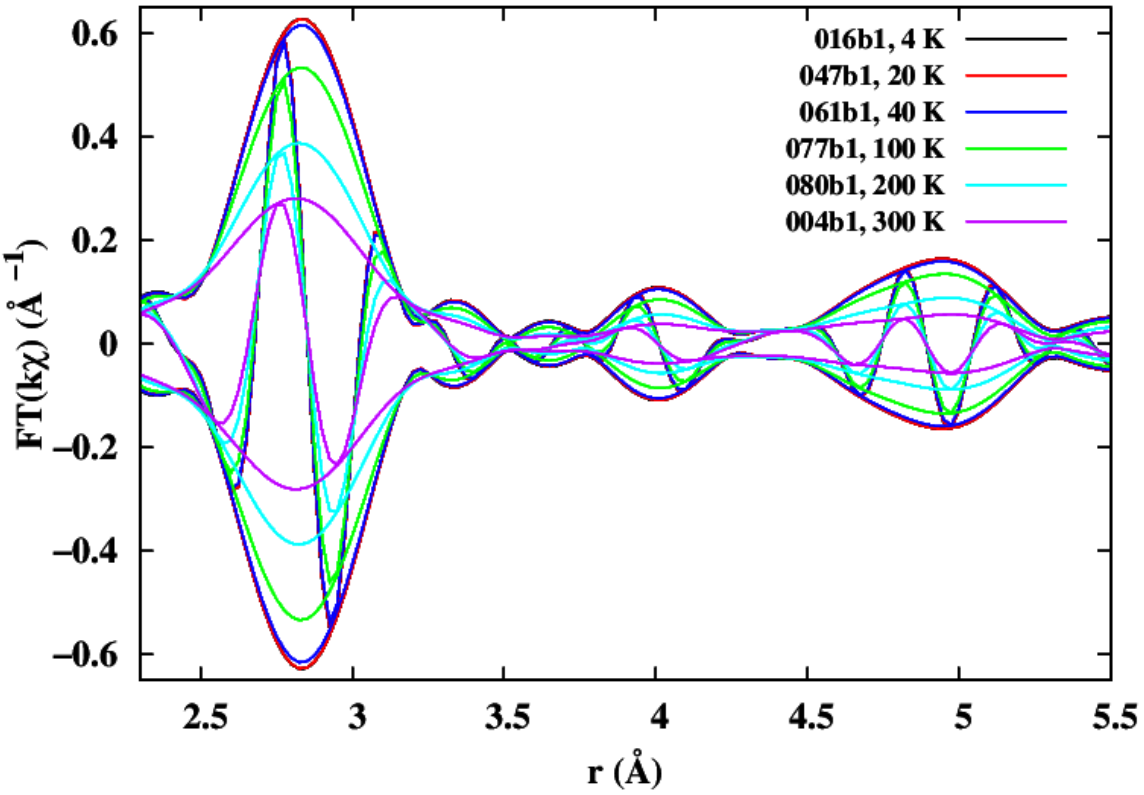


Figure 4.6: The Fourier transform of $k\chi(k)$ for the U $L_{III}$ absorption edge k-space data. The data depicted had a Fe concentration of x=0.05. The set temperatures are given in the legend.

The same process discussed above was applied to the Ru K edge data, the $UO_2$ reference sample, the Fe foil reference sample, and the Ru foil reference sample. The k-space and r-space figures for the Ru K edge may be seen in Appendix B.

## 4.2 Fluorescence Data Reduction

The data for the Fe K edge were collected in fluorescence mode, as discussed in Section 2.3. Each absorption edge was observed at various set temperatures that ranged from around 10 K to 300 K, with most of the data focused in the low tem-

perature region to investigate the HO phase. Since Fe is the dopant in $URu_{2-x}Fe_xSi_2$ at various concentrations, the signal of the Fe K absorption edge increased as the concentration of Fe increased. This effect is seen in Figure 4.7.

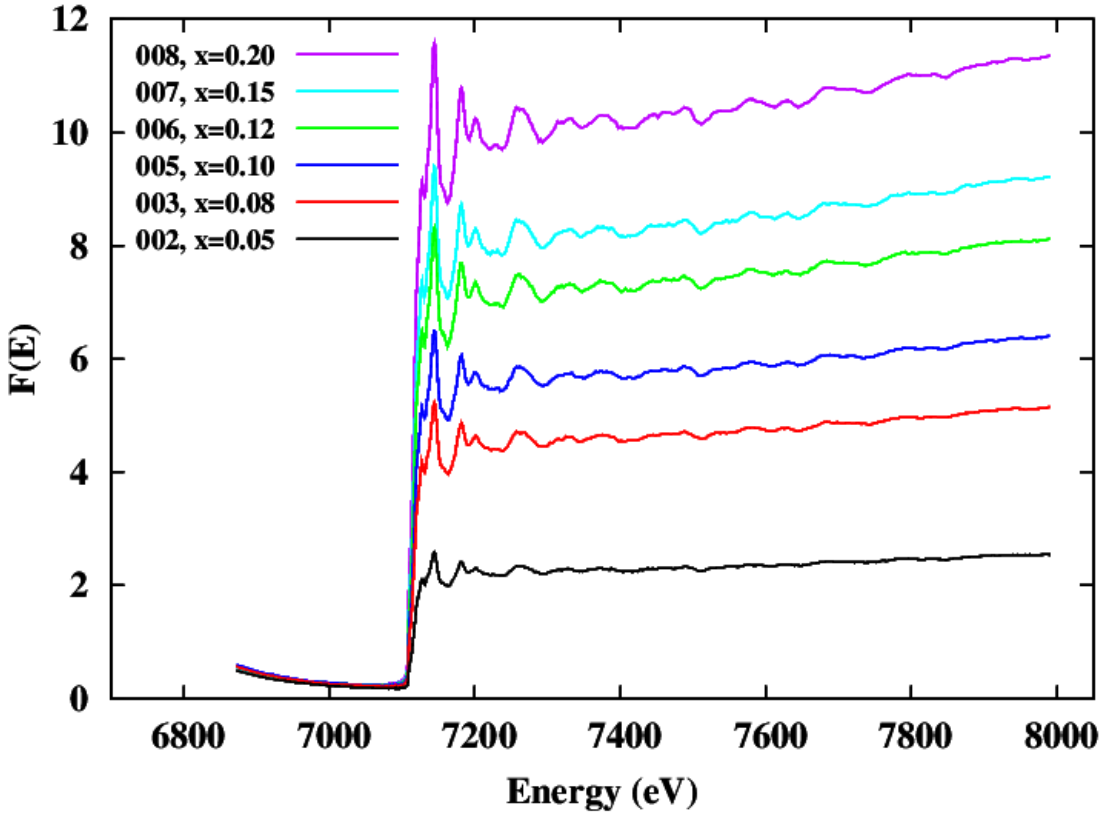


Figure 4.7: Fe K absorption edge data taken in fluorescence mode. The three data scans for each concentration were averaged in this figure due to small fluctuations caused by the low concentration of Fe. All concentrations are plotted at 9 K to show how the Fe K absorption edge signal increases as the concentration of Fe increases.

The Fe K edge data with a Fe concentration of x=0.05 taken at 9 K will be examined. These data is shown in Figure 4.8.

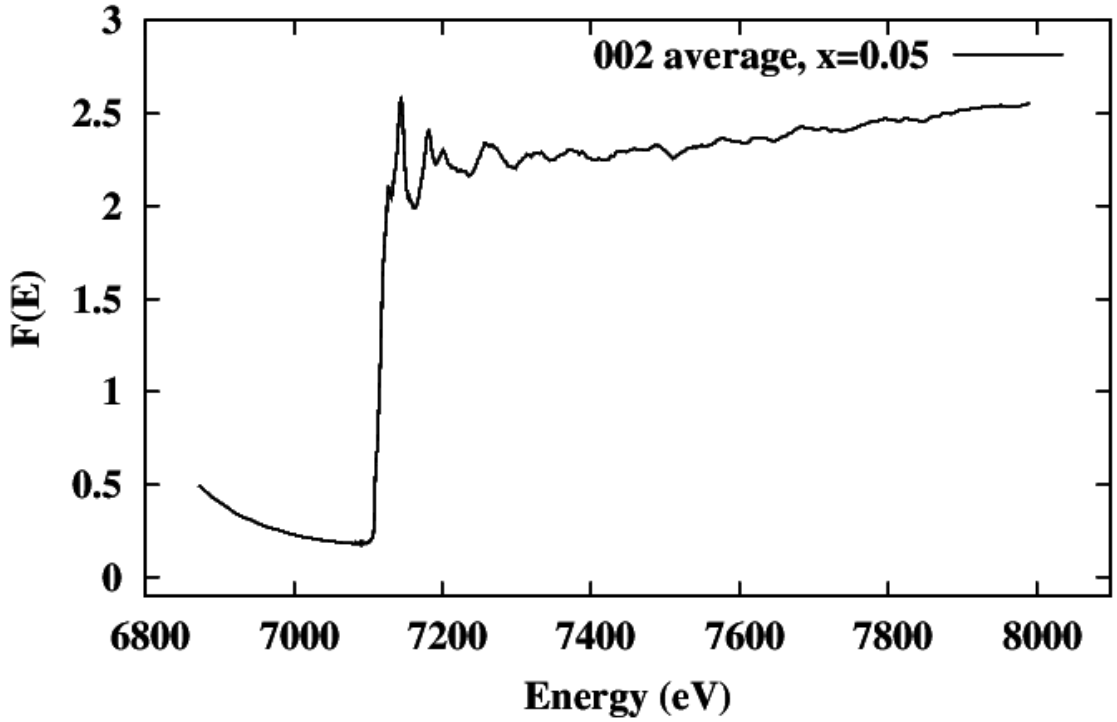


Figure 4.8: Fe K absorption edge data with a Fe concentration of x=0.05 at 9 K. This was taken in fluorescence mode.

The background contributions need to be removed. Similar to the transmission data, the pre-edge is fit to a function. However, the pre-edge for the Fe K edge was fit to an $9^{th}$ order polynomial that was extrapolated to a constant at high energy, rather than being fit using the Victoreen formula. Due to the variation in the pre-edge for each concentration, each pre-edge was fit to a $9^{th}$ order polynomial over different fit ranges along the pre-edge and was extrapolated to its own unique constant in the high energy region. This is seen in Figure 4.9

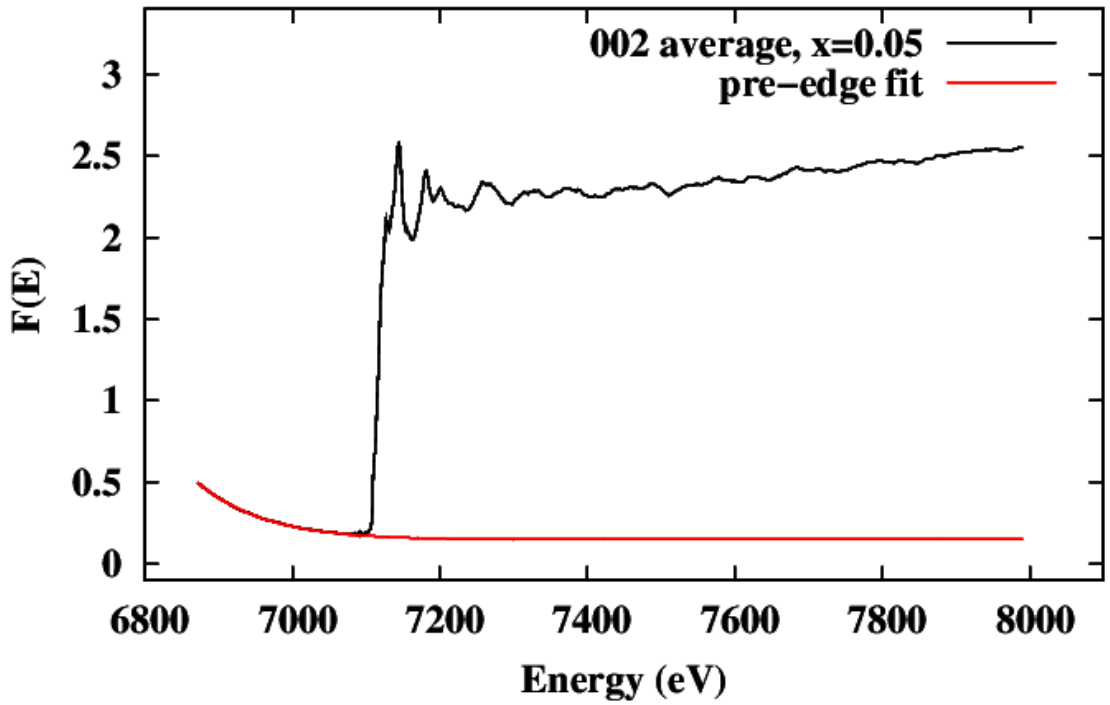


Figure 4.9: Fe K absorption edge fluorescence data (black line) with a Fe concentration of x=0.05 taken at 9 K. An 9$^{\text{th}}$ order polynomial was fit to the pre-edge region (red line) from 6872 eV to 7070 eV.

The solid line in Figure 4.9 represents the entire fluorescence data collected for the Fe K edge at 9 K with a Fe concentration of x=0.05. The solid red line in Figure 4.9 portrays the 9$^{\text{th}}$ order polynomial fit to the pre-edge. The pre-edge fit of the Fe K edge with x=0.05 at 9 K had a fit range from 6872 eV to 7070 eV and the 9$^{\text{th}}$ order polynomial was extrapolated to a constant of 0.148. This 9$^{\text{th}}$ order polynomial fit to the pre-edge is then subtracted from the total data.

The resulting data is then normalized to unity by the division of $\Delta\mu(E) = \mu(E) - \mu_b(E)$ by the step height of the absorption edge $\mu_{E'}$. Figure 4.10 shows the normalized Fe K edge at 9 K with a Fe concentration of x=0.05.

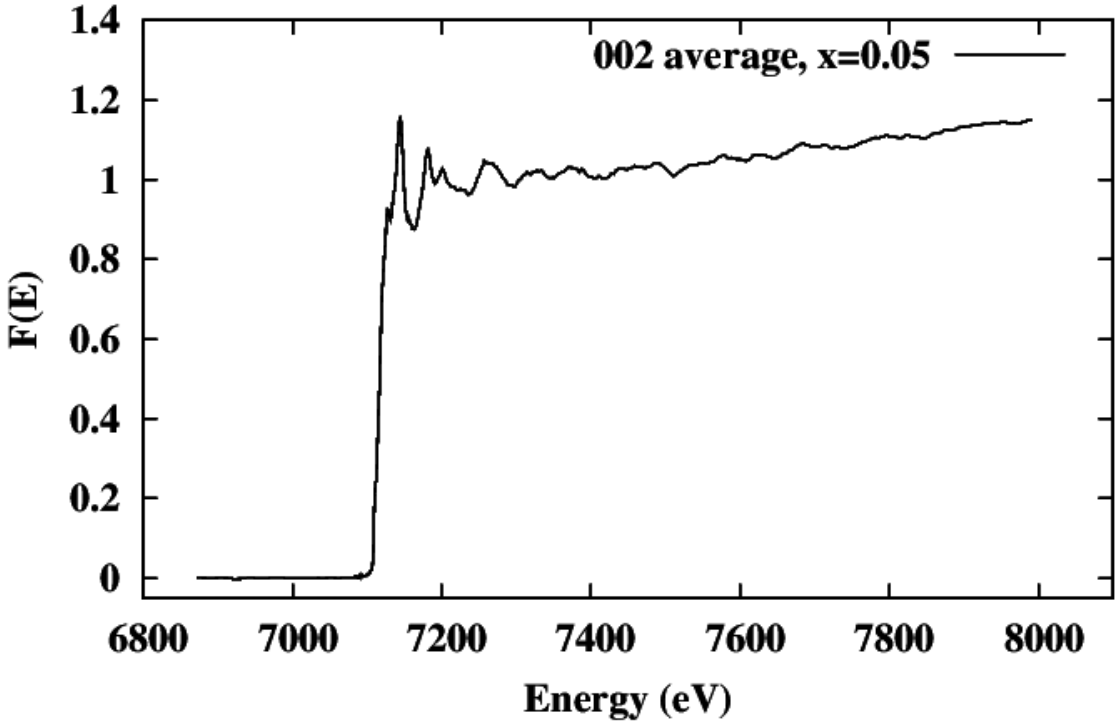


Figure 4.10: Normalized Fe K absorption edge fluorescnece data with a Fe concentration of x=0.05 taken at 9 K. The background contribution at the pre-edge had been removed.

Once the background contribution had been subtracted from the pre-edge and the data set had been normalized, we again do a post-edge background fit in order to extract the EXAFS oscillations $\chi(E)$, as done for the U $L_{III}$ edge and Ru K edge. The post-edge fit for the normalized Fe K edge fluorescence data with a Fe concentration of x=0.05 at 9 K is shown in Figure 4.11.

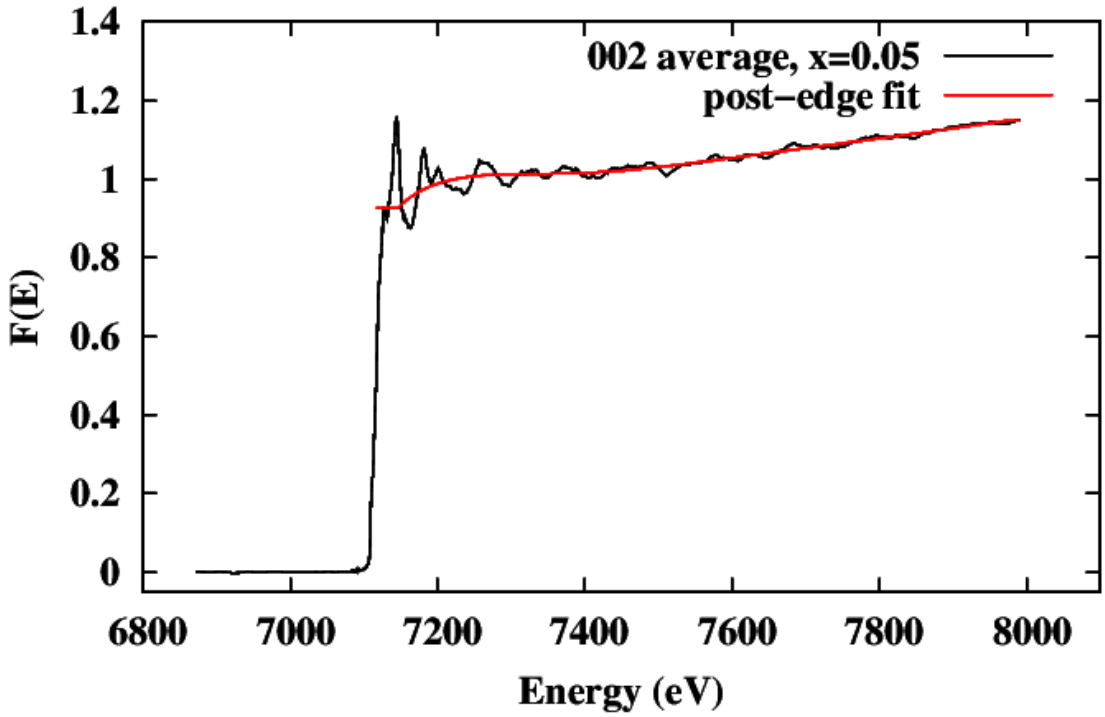


Figure 4.11: Normalized Fe K absorption edge fluorescence data with a Fe concentration of x=0.05 taken at 9 K is shown as the solid black line. The post-edge fit to high energy region is shown as the solid red line.

The normalized fluorescence data that had the background contributions removed from the pre-edge and post-edge was then converted into k-space by Eq. 4.2. This results in $\chi$ as a function of the wavevector k. For the Fe K edge, we also use k-weighting, $k^n\chi(k)$. The k-space conversion of the Fe K edge with all concentrations at 9 K is shown in Figure 4.12.

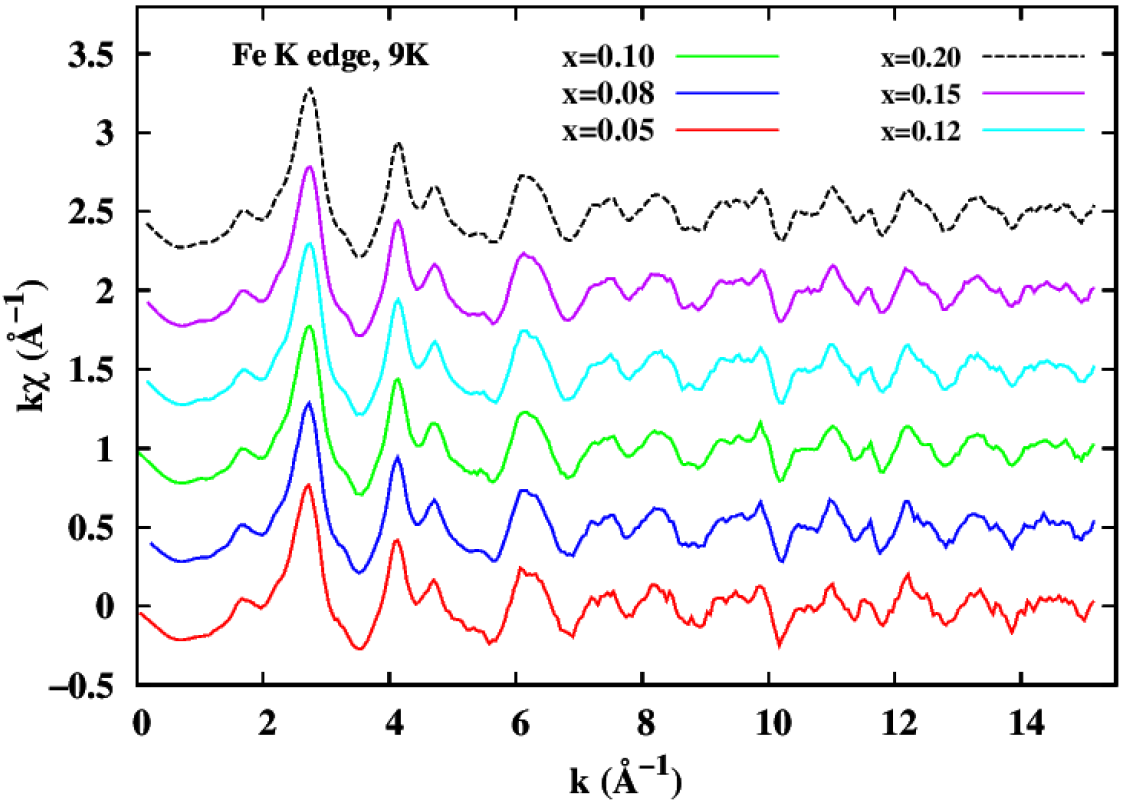


Figure 4.12: Fe K absorption edge fluorescence data converted into k-space. The data depicted were taken at 9 K, where the three scans at each concentration were averaged in order to reduce noise caused by the low concentration of Fe.

Once the data were converted from e-space to k-space, a Fourier transform was performed on $k\chi$ over a finite k range [6]. The Fourier transform of $k\chi$ of the Fe K edge was performed over a k-space range from 4.0 Å$^{-1}$ to 14.0 Å$^{-1}$. Figure 4.13 shows the Fourier transforms of $URu_{2-x}Fe_xSi_2$ at various set temperatures with a Fe concentration of x=0.05.

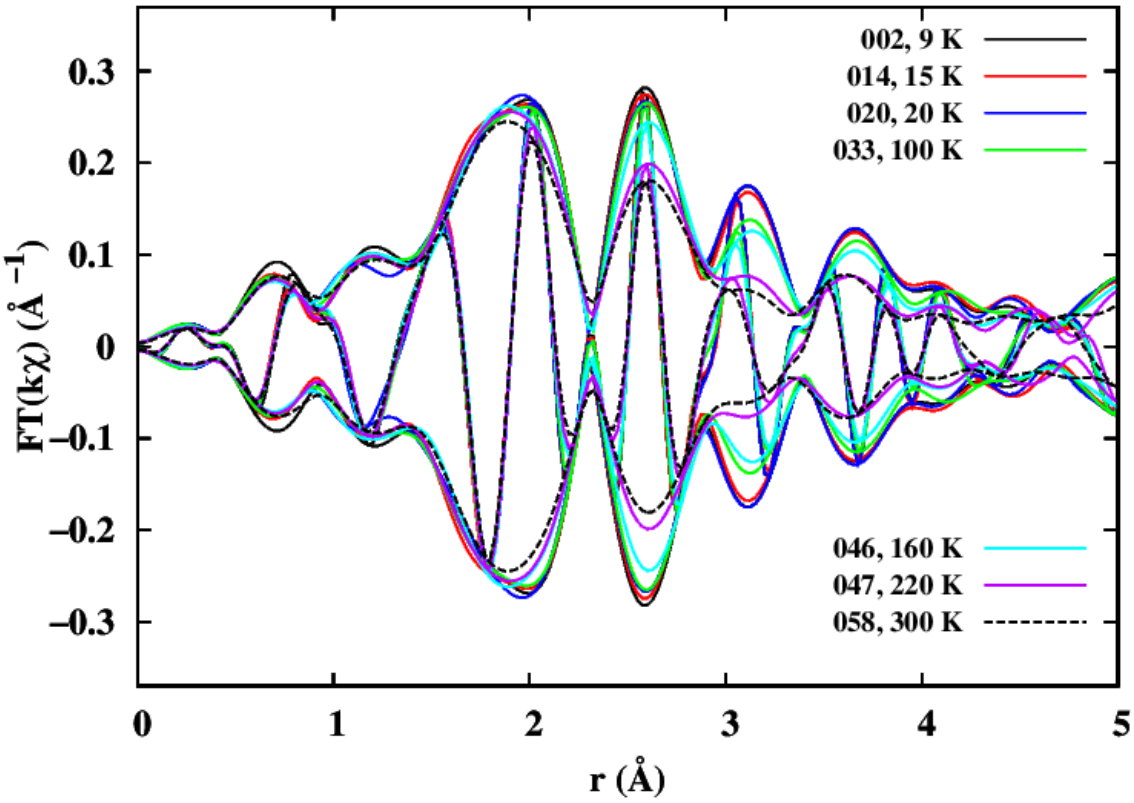


Figure 4.13: The Fourier transform of the Fe K absorption edge k-space data. The data depicted had a Fe concentration of x=0.05: all set temperatures taken are shown. The three scans at each temperature were averaged to reduce noise caused by the low concentration of Fe.

# Chapter 5

# R-space Fits

The theoretical standards that were created by the FEFF program should resemble the data well. This can be determined by fitting the theoretical standards to the experimental data in r-space through a program called RSFIT. The theoretical standards were created under the assumption of no systematic disorder, i.e. $\sigma = 0$, or no multiple electron effects. When the data is fit to a sum of theoretical standards, each standard will have to be broadened, scaled, and shifted to obtain a good fit. Both the experimental data and the theoretical standards must be Fourier transformed under the same range. The final fit results and other relevant information are written out to a file that will be used in another process.

The constraints of the amplitudes were fixed to the number of neighboring atoms with the same bond length around the core atom in the known structure – see Fig. 1.9. Since a percentage of Fe replaced Ru, the amplitude of all standard files that contained Ru, as well as Fe, had to account for the loss of Ru as the concentration of

Fe increased. This was accomplished by instituting a dummy variable D1 = $\frac{x}{2}$. The amplitudes were also constrained by another dummy variable D2, which allowed for $S_o^2$ to vary. It was found that the U edge preferred $S_o^2 = 1.0$, while the Fe edge and the Ru edge preferred $S_o^2 = 0.8$ and $S_o^2 = 0.9$, respectfully.

The first two or three peaks were allowed to shift in r-space with no constraints since these peaks have a big enough amplitude with low enough overlap with other peaks to get a good fit. The further out in r-space, the more the individual peaks constructively and destructively interfere with each other, resulting in a lower amplitude for each peak and a worse overall fit. To overcome this, the r-space shift of the standard files past the first 2 peaks were constrained to the second peak in terms of a ratio between their bond lengths. This type of constraint makes the distances to further neighbor peaks in the EXAFS data consistent with the known structure.

Every peak had no constraints on broadening, or the Debye-Waller factor $\sigma$. However, the Ru-U peak has the same bond length as the U-Ru peak in the U edge. Both of these peaks had the same $\sigma$ value that was determined from the RSFIT of the Ru-U peak since the Ru edge was the first edge to be investigated.

A plot of a fit from each edge made by RSFIT is presented in Appendix C. Recall that typically three scans were made for each edge at a set temperature, so the figures that are shown in Appendix C portrays of one of those scans.

# Chapter 6

# Results

The absorption edges at each Fe concentration around 10 K and 20 K were examined. We anticipated finding a change in electronic structure in the U $L_{III}$ edge that would be consistent with related findings, i.e. an increase in the U magnetic moment above x=0.1 in the low temperature LMAFM phase.

## 6.1 Variation in Absorption Edges

The variation in each absorption edge was determined by investigating the XANES region of the normalized absorption edge with the pre-edge subtracted off for the data taken around 10 K and for the data taken at 20 K; The temperatures that correspond to being below and above the HO phase transition. The variation of the absorption edge for each reference sample at the low temperature and 20 K were examined.

The absorption edges for the $UO_2$ reference sample, as well as for the Ru foil

reference sample, at both temperatures of interest varied slightly in energy; within 1 eV of each other. The relative shifts of the reference scans were determined to about 0.05 eV, using the x=0 sample as a fiducial scan. Using these relative shifts, the edge position for each scan was corrected for these small energy drifts. There was more variation in the absorption edge of the Fe foil reference sample; the three scans for each concentration were averaged together. The normalization of the U $L_{III}$, Fe K, and Ru K edges were modified slightly (a few percent change in amplitude) so that the XANES overlapped well at the top of the edge.

The seven U $L_{III}$ absorption edges shown in Figure 6.1 a and b overlap extremely well; the positions vary by 0.1 eV or less, as depicted by the inset plots. No change in the electronic structure is seen in the U $L_{III}$ edge of $URu_{2-x}Fe_xSi_2$ as the Fe concentration is changed, particularly in the regime above x=0.1, for which the low temperature phase is magnetic (AFM). The variation of the U $L_{III}$ absorption edge is shown in Figure 6.1.

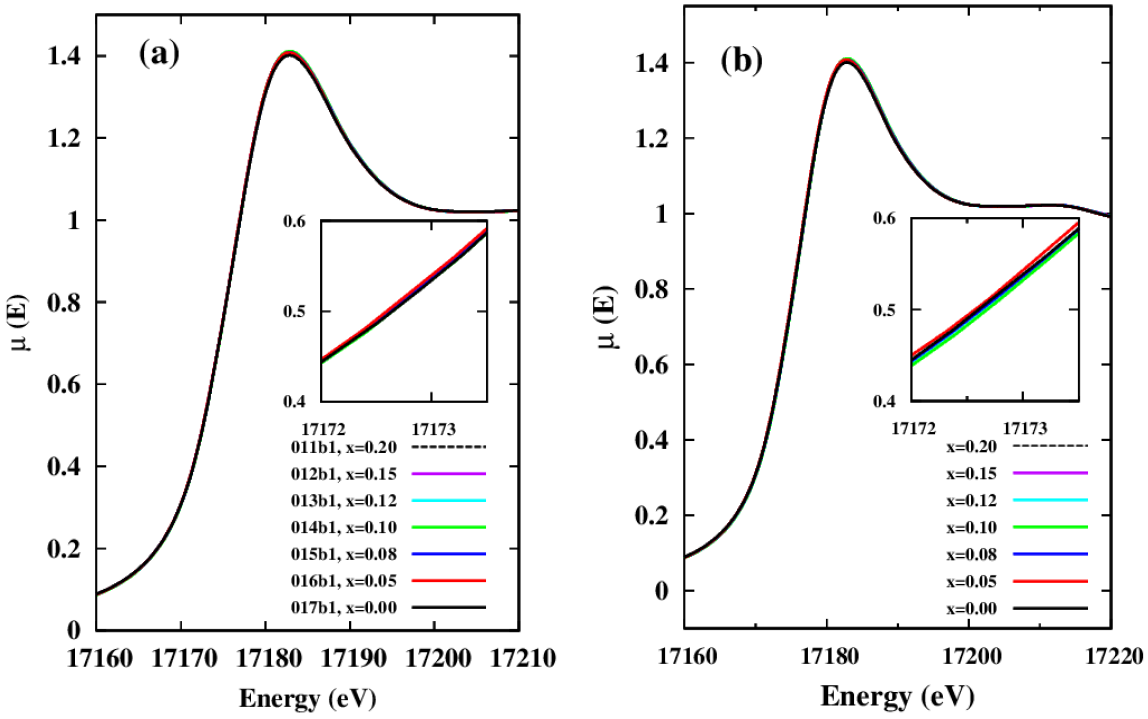


Figure 6.1: The U $L_{III}$ absorption edge at 4 K (a) and at 20 K (b) for all Fe concentrations. The inset plots focus on the variation of the U $L_{III}$ absorption edge at the half-height point. No change in electronic structure is seen.

The Fe K absorption edges of $URu_{2-x}Fe_xSi_2$ at 9 K and 20 K were correctly slightly, based on the positions of the Fe foil reference sample for each scan as done for the other edges. The amplitudes of the XANES were slightly adjusted so all curves overlap well above 7140 eV. This is seen in Figure 6.2.

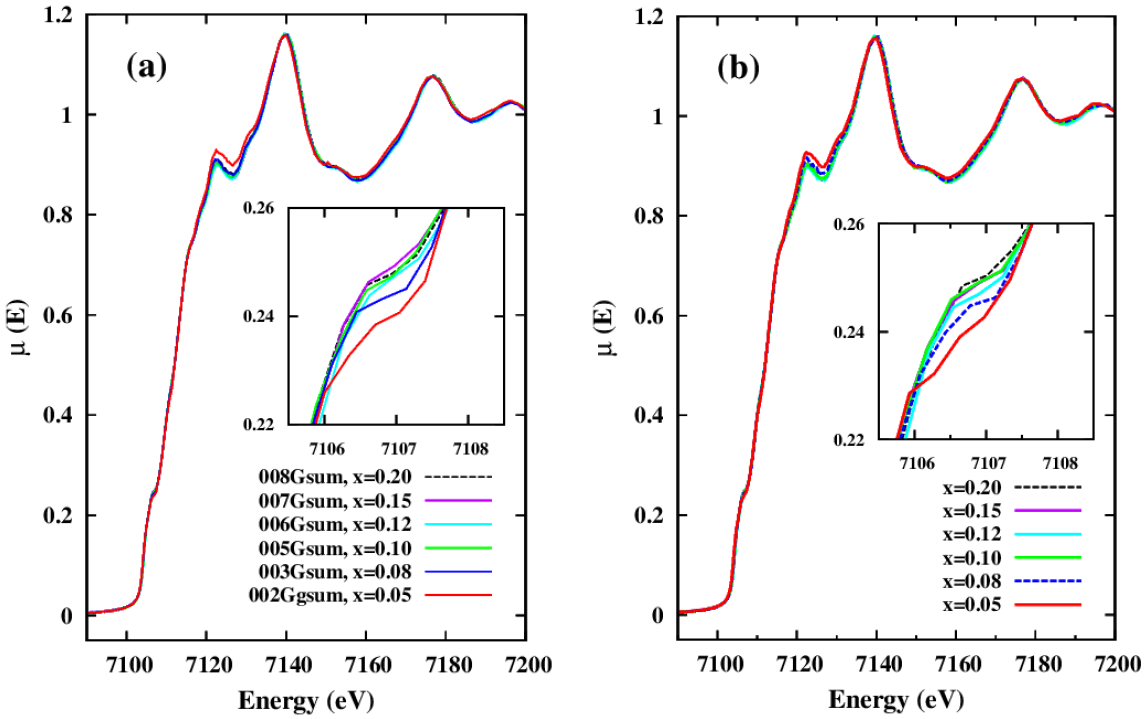


Figure 6.2: The Fe K absorption edge at 9 K (a) and at 20 K (b) for all Fe concentrations. The inset plots focus on the electronic structure that occurs in the Fe K absorption edge at 7106.5 eV, but variations are close the signal-to-noise of the Fe K edge data. At 7122 eV the x=0.05 sample differs slightly from the other samples.

The six Fe K absorption edges at both 9 K and 20 K show a couple of small anomalies in the edge. The first one occurs around $\mu(E) = 0.24$, which is portrayed by the inset plot in Figure 6.2 a and b. The change in the electronic structure at this location in the Fe K edge minimally vary. The second anomaly occurs around $\mu(E) = 0.90$, which also illustrates a larger variation in energy at the 20 K data set.

The Ru K absorption edges of $URu_{2-x}Fe_xSi_2$ at 7 K and 20 K were shifted slightly based on the positions of the Ru foil reference edges, as described above, and the normalized amplitudes were adjust slightly so all files overlap above 22150 eV. Overall the XANES for the seven samples overlap extremely well as shown in Fig 6.3, and

variations in positions are 0.1 eV or less, which is close to our reproducibility limit.

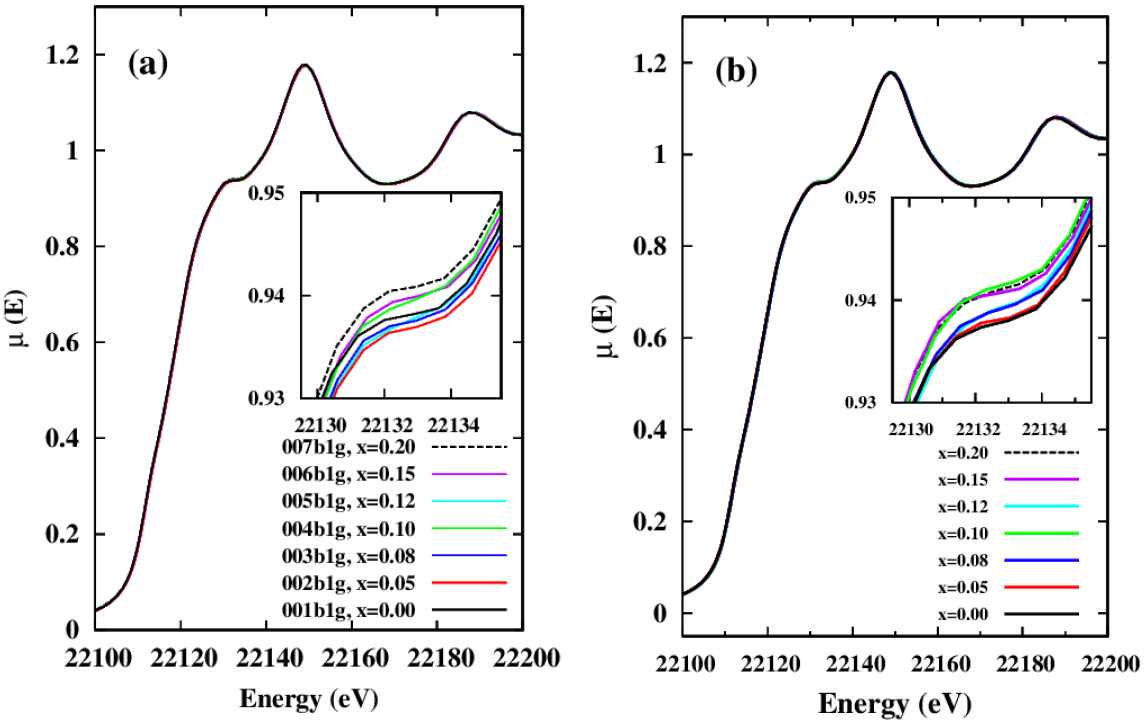


Figure 6.3: The Ru K absorption edge at 7 K (a) and at 20 K (b) for all Fe concentrations. The inset plots focus on the electronic structure that occurs in the Ru K absorption edge near 22132.5 eV; the amplitude variation is 0.5% or less at this feature.

The Ru K edge at 7 K and 20 K show a tiny anomaly in the edge that takes place around $\mu(E) = 0.94$, which can be seen by the inset plots in both Figure 6.3 a and b. The variation in amplitude is of order 0.5% for this electronic structure.

## 6.2 Pair Distance and Debye-Waller Factor Plots

Once the standard files are correctly fit to the data, a program called PPROC will read in the outfile generated from RSFIT and will compute the average and relative error for bond length and the Debye-Waller factor, $\sigma^2$, at each temperature. Each $\sigma^2$ data point will be will be represented by its own unique color according to its respected Fe concentration, which will be given in the legend of each plot. The Debye temperatures determined by the fit of each concentration at set temperatures to the Debye model will be portrayed by the same color scheme applied to the $\sigma^2$ data points. The Debye temperature will also be present in a legend in the $\sigma^2$ vs Temperature plot. If there is no excess disorder as low temperature, the $\sigma^2$ data and its corresponding Debye fit will be on the same plot, but each concentration will be offset with respect to x=0.00 so they will not overlap with each other. If there is excess disorder at low temperature, the $\sigma^2$ data and the corresponding Debye fit will be individually plotted along with an inset plot that will show the excess disorder at low temperatures. The Debye fits for concentrations that have data at 300 K will be represented by a solid line of its respectful color. The Debye fits that do not have data at 300 K will be represented by a dashed line of its respectful color. This format will be applied to each atom pair and for each edge.

We expect that the bond lengths between Fe and its nearest U, Si, and Ru neighbors to decrease as temperature decreases, consistent with thermal expansion. We expect that the Debye-Waller factor across all set temperatures for each peak will

follow the Debye model.

### 6.2.1 Pair Distance Plots

PPROC will generate the average distance between atoms with a relative error at each set temperature. Relative errors for first neighbors are typically 0.003 A or less, but absolute errors can be up to 0.01A from systematic effects. Errors for further neighbors are typically between 0.01 and 0.02 A. Each bond length was plotted as a function of temperature in order to investigate its temperature dependence. Each pair distance plots show evidence of thermal contraction as temperature decreases. The pair distances that are determined from diffraction also decrease as the temperature is lowered; However, suitable data to show this effect were not found. Instead, the pair distances from diffraction results found at 300 K are used and are portrayed by a solid red line. These plots are shown in Appendix D.

The pair distance plots of U with its nearest Si, Ru, and U neighbors decrease as temperature decreases, deviating from the distance predicted by diffraction. At high temperature, the distance of each U peak also differs from diffraction. The pair distance plot of the U-Si peak is shown in Figure 6.4. The Fe concentrations of x=0.00 and x-0.20 lack data above 100 K, and x=0.08 does not have 200K data. The U-Ru and U-U plots may be seen in Figure D.2 and Figure D.3, respectively.

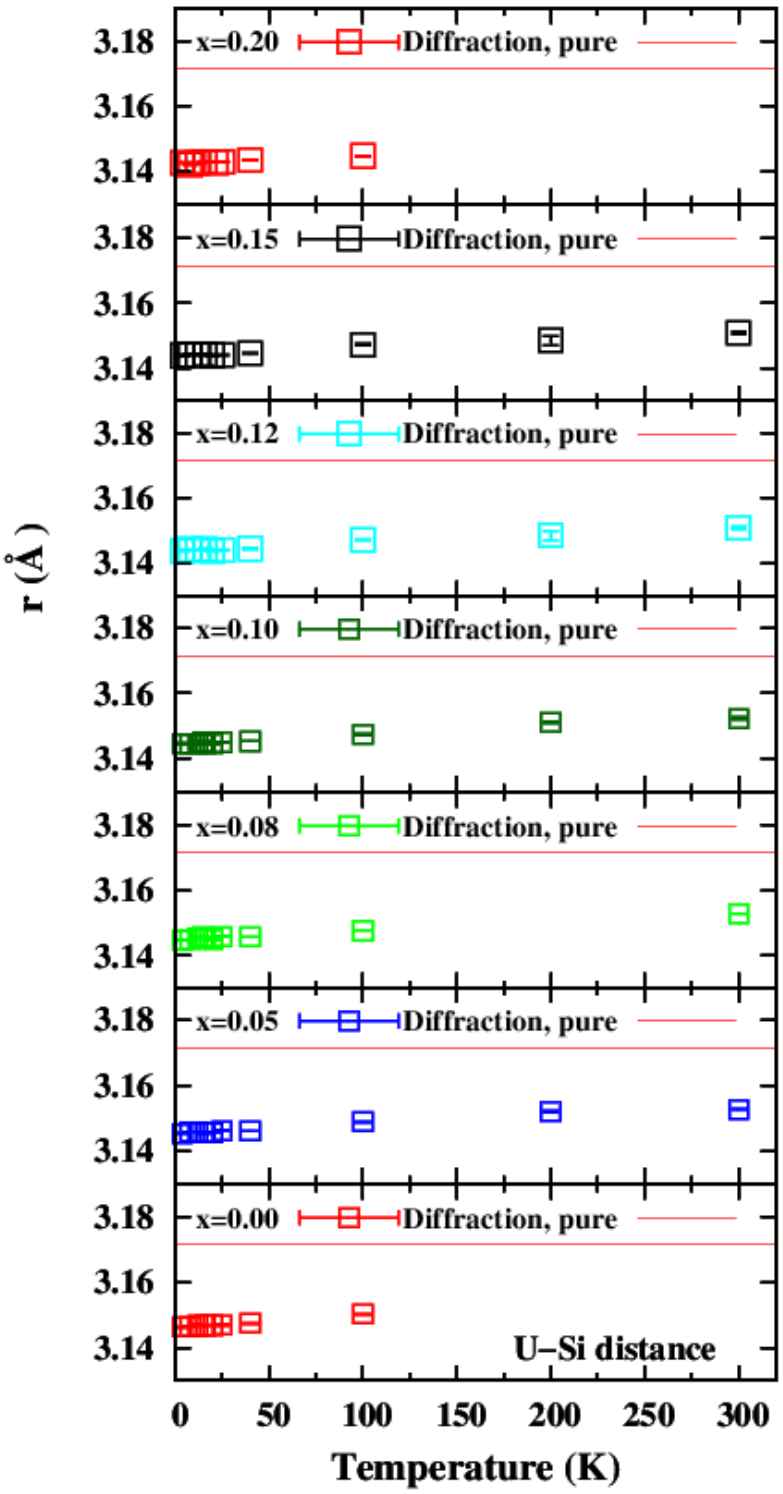


Figure 6.4: The average distance between U and its closest Si neighbor as a function of temperature. The distance between U and its closest Si neighbor was found to be 3.1715 Å based on diffraction at 300 K, and is depicted as the solid red line. There is a discrepancy in comparison with diffraction at 300K; the EXAFS distances are about 0.02 A shorter.

The pair distance plots of Fe with its nearest Si, Ru, and U neighbors is shorter compared to the Ru-X pair distances at 300 K that is depicted by the red line in Figure 6.5. The deviation from the Ru-X pair distances for each corresponding Fe-X distance is evidence of the doping of Fe on Ru site acting as a chemical pressure. A clear decrease in position as temperature decreases is observed as expected for thermal contraction. Figure 6.5 shows the Fe-Si peak position plot. The remaining Fe-Ru and Fe-U plots may be seen in Figure D.5 and Figure D.6, respectfully.

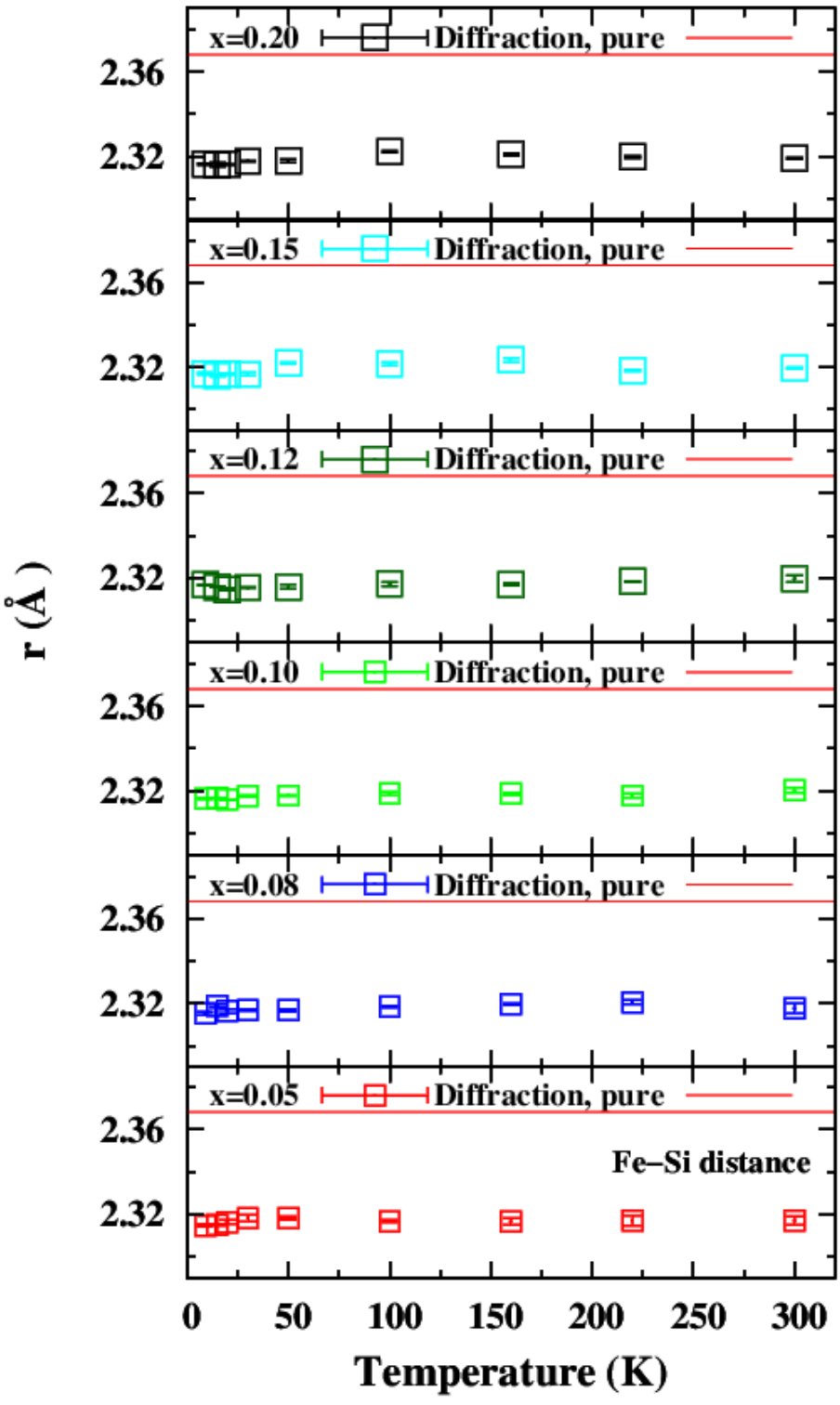


Figure 6.5: The average distance between Fe and its closest Si neighbor as a function of temperature. The distance between Fe and its closest Si neighbor was found to be 2.3683 Å based on diffraction at 300 K, and is depicted as the solid red line. The Fe-Si bond is significantly shorter by roughly 0.05A compared to Ru-Si, which agrees the concept of chemical pressure.

The pair distance plots of Ru with its closest Si, Ru, and U neighbors remain constant as temperature decreases, as well as x increases. They are also close to the distance predicted by diffraction at 300 K. Figure 6.6 shows the Ru-Si position plot where the solid red line portrays the distance from diffraction at 300 K. The remaining pair distance plots of Ru with its closest Ru and U neighbor may be seen in Figure D.8 and Figure D.9, respectfully.

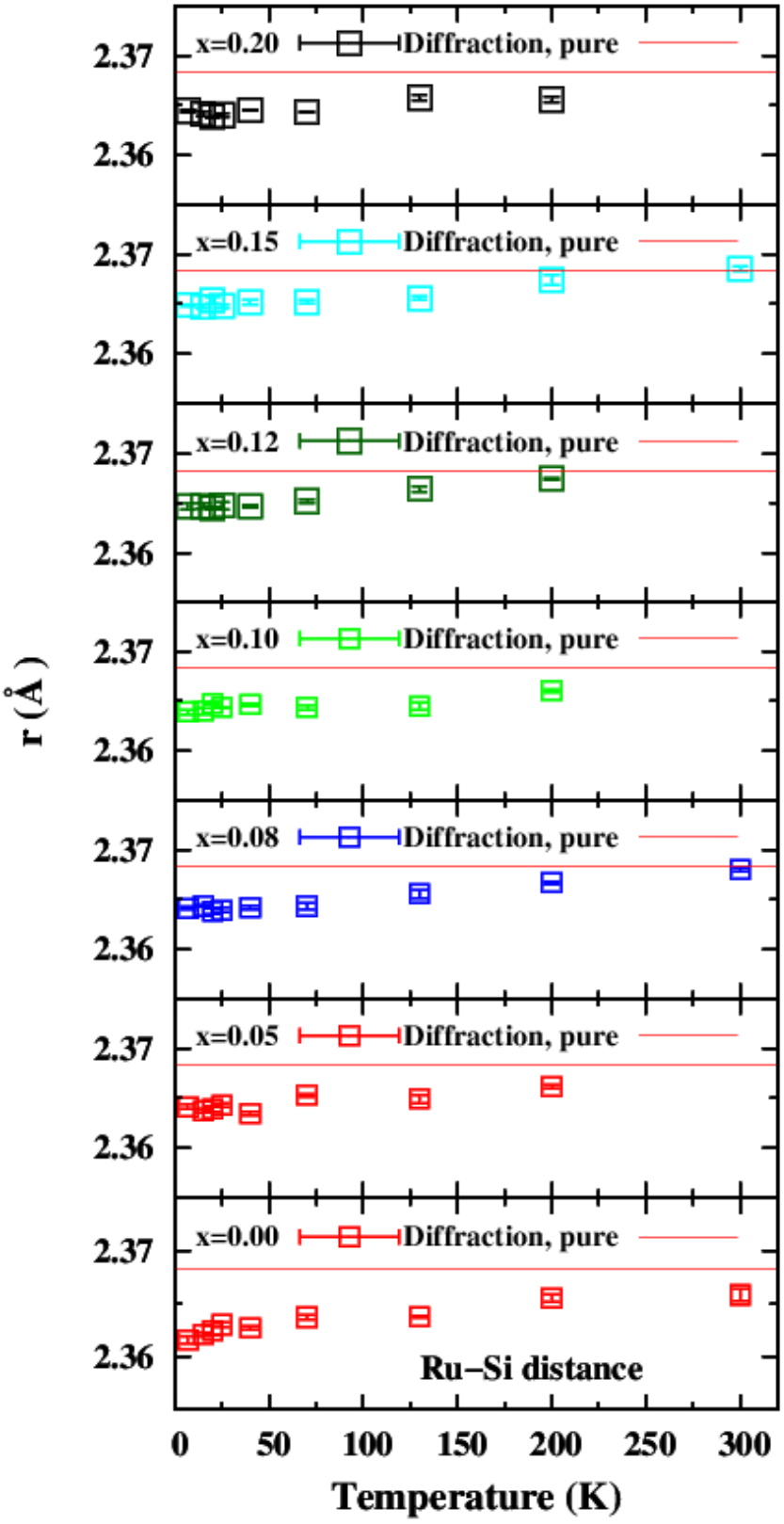


Figure 6.6: The average distance between Ru and its closest Si neighbor as a function of temperature. The distance between Ru and its closest Si neighbor was found to be 2.3683 Å based on diffraction at 300 K, and is depicted as the solid red line.

### 6.2.2 Debye-Waller Factor Plots

PPROC will similarly extract and calculate the average $\sigma^2$ with its relative error at each set temperature. There are also systematic errors - e.g from choice of $S_o^2$, of order 0.0004 Å$^2$. The relative errors are smaller, typically on the order of 0.0002 Å$^2$. For each concentration, the $\sigma^2$ results for each pair were fit to the Debye model, from which a corresponding Debye temperature was determined. However, the U $L_{III}$ edge data and the Ru K edge did not have high temperature data for every concentration. The concentrations that do not have data up to 300 K have been given in Section 2.2.

To overcome this, the Debye temperature was found for the concentrations that had data through 300 K. A plot of x vs Debye Temperature was created, where a line was fit through the data, from which the Debye temperature of the concentration with no high temperature data was found. These plots are shown in Appendix E.

#### Ru K Edge Debye-Waller Factor Plots

The Debye fit for the Ru-Si $\sigma^2$ vs temperature plot was done from 100 K - 320 K for all concentrations. This range was determined due to excess disorder that develops below 70 K. The data are plotted in Figure 6.7 and have the unusual feature that $\sigma^2$ actually increases below roughly 70K. Note the very high correlated Debye temperature for this pair, 713-786 K: this is the stiffest bond in the system.

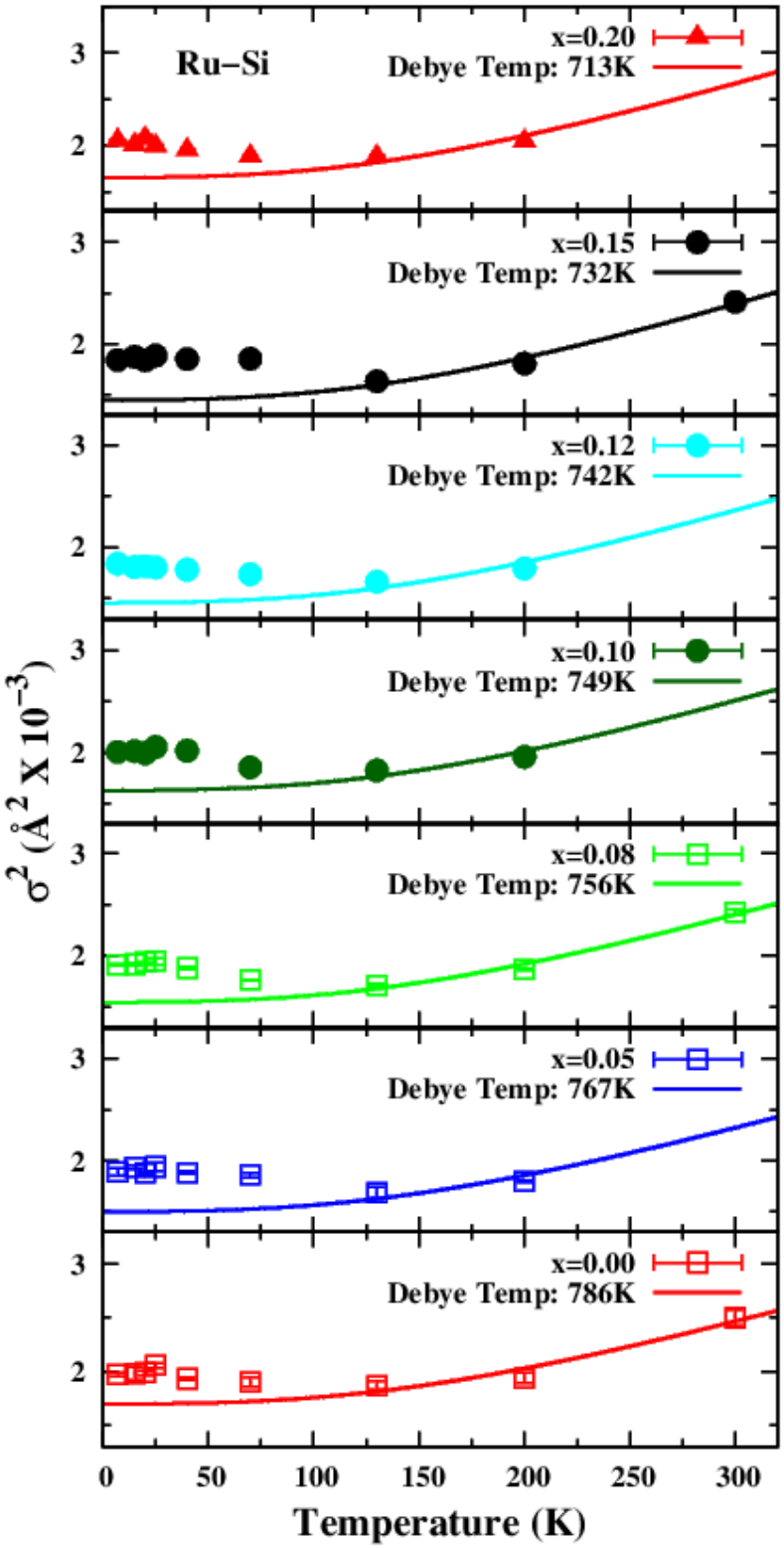


Figure 6.7: The Debye-Waller factor for each concentration of the first Ru-Si peak fit to the Debye model. The Debye curve was fit across all data points from 100 K to 320K. The Debye curve deviates from the low temperature data, providing evidence of excess static disorder.

The difference was taken between the $\sigma^2$ data points and the Debye curve at each concentration, which is shown in Figure 6.8.

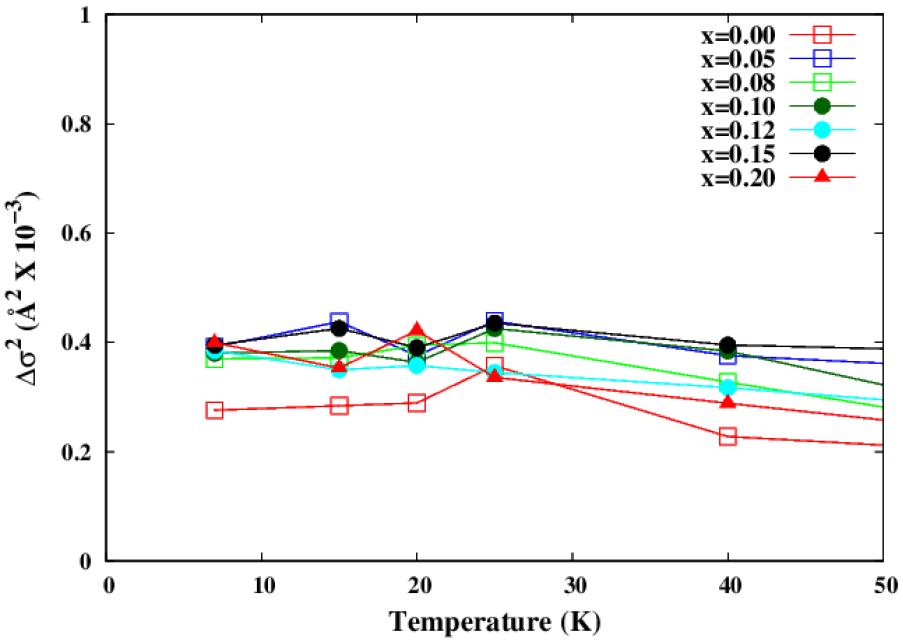


Figure 6.8: Difference between the $\sigma^2$ data points from the Ru-Si peak and the Debye curve fit to them.

The excess disorder appears to begin around 70 K and increases until around 20 K where it begins to decrease slightly. For samples with a 300 K data point, the Debye curve fits the high temperature data points well.

The Debye fit for the Ru-Ru $\sigma^2$ vs temperature plot was fit from 0 K - 320 K for all concentrations. The Debye fits for the Ru-Ru peaks at each concentration are shown in Figure 6.9 and the data fit the Debye model within error with no excess disorder at low temperature.

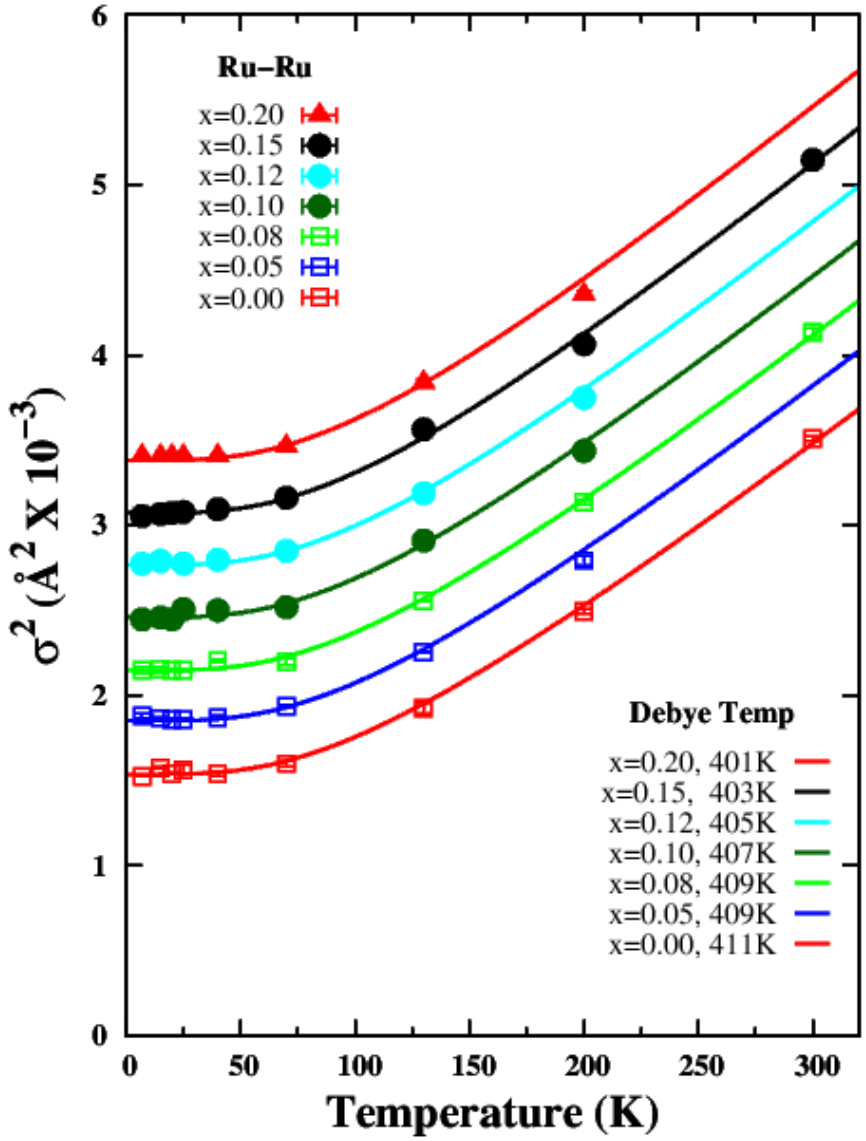


Figure 6.9: The Debye-Waller factor for each concentration of the first Ru-Ru peak fit to the Debye model. The Debye curve was fit across all data points from 0 K to 320 K, and fit the low temperature data within the error of the data. No excess static disorder is seen.

The Debye fit for the Ru-U $\sigma^2$ vs temperature plot was fit from 100 K - 320 K for all concentrations. This range was again determined due to static disorder at low temperature. The Debye fits for the Ru-U peaks at each concentration are shown in

Figure 6.10. The magnitude of the excess disorder is comparable to that for Ru-Si. However, the low correlated Debye temperature that is around 210 K implies that the Ru-U thermal contribution is large, implying a small relative change. Ru-U is the third peak for the Ru edge data, while the corresponding U-Ru peak in U edge data is the second peak; we will use the U-Ru results discussed in next section for this pair.

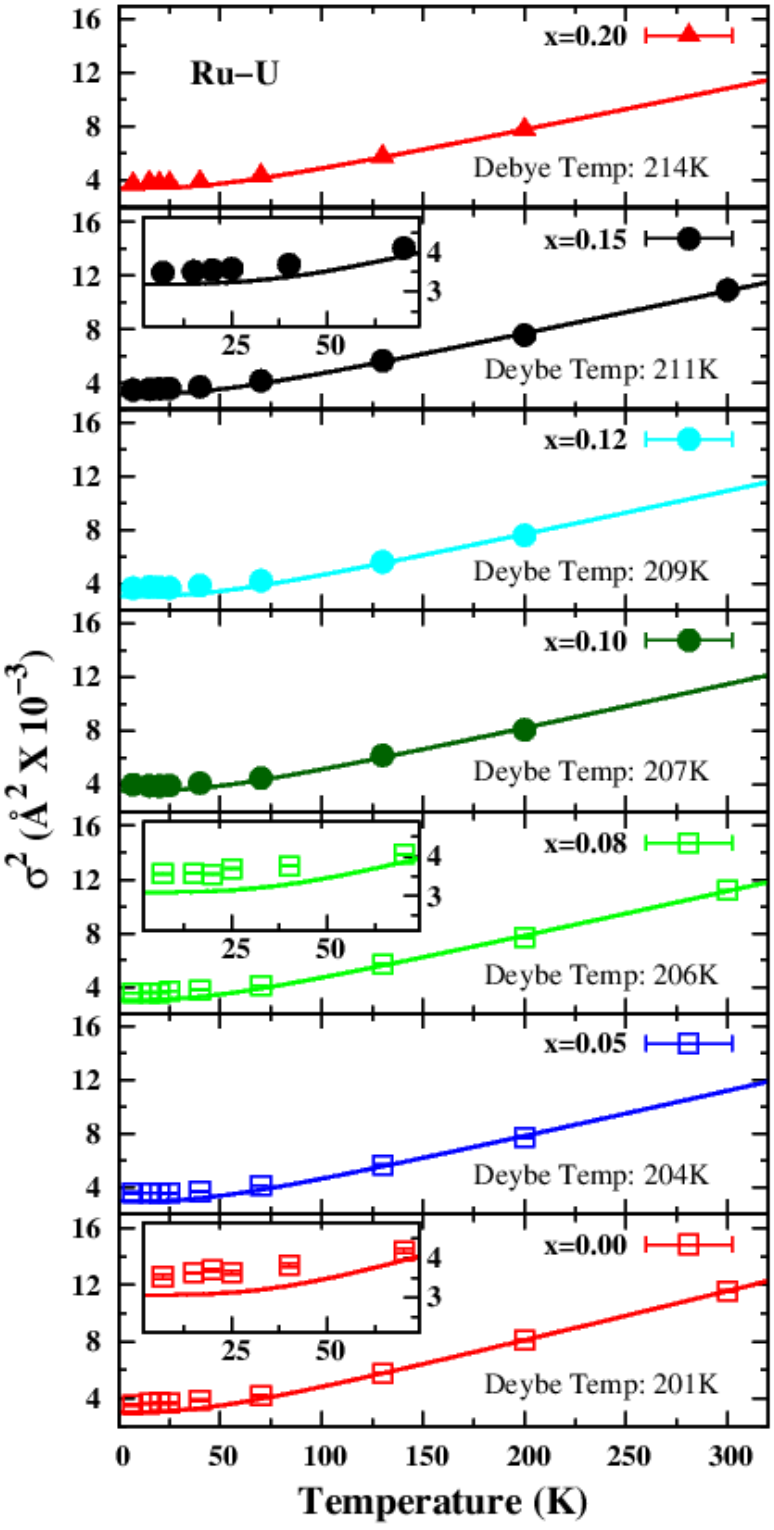


Figure 6.10: The Debye-Waller factor for each concentration of the Ru-U peak fit to the Debye model. The Debye curve was fit across all data points from 100 K to 320K. The Debye curve deviates from the low temperature data for concentrations with data up to 300 K, providing evidence of excess static disorder.

The Debye temperature for each concentration is given in the legend that is located in the bottom right corner of each panel in Figure 6.10. The Debye curve fits the high temperature data points well, but excess disorder is present at low temperatures. Inset plots were made for the concentrations that had data up to 300K in order to show the static disorder at low temperature. The difference was taken between the $\sigma^2$ data points and the Debye curve only for concentrations with data up to 300 K, which is shown in Figure 6.11.

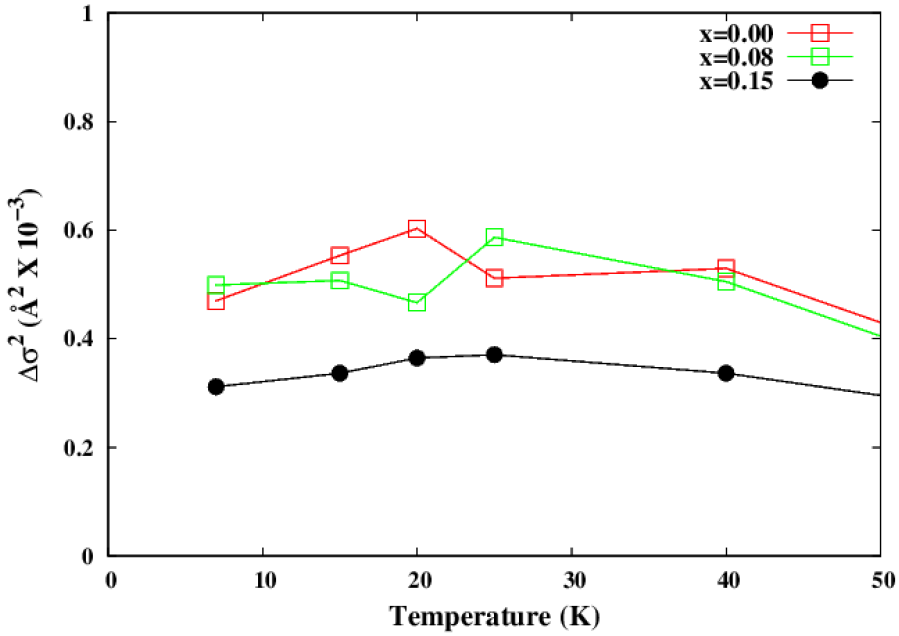


Figure 6.11: Difference between the $\sigma^2$ data points up to 300 K from the Ru-U peak and the Debye curve fit to them.

The excess disorder continues to increase as the temperature is lowered down to 20 K, similar to that for the Ru-Si peaks in Figure 6.7.

### U $L_{III}$ Edge Debye-Waller Factor Plots

The Debye fit for the U-Si $\sigma^2$ vs temperature plot for all concentrations were done from 0 K - 320 K. The concentrations x=0.00 and x=0.20 only had data up to 100 K, so a good Debye fit was not able to be attained. Instead, the Debye temperature from x=0.05 was used for x=0.00, and the Debye temperature from x=0.15 was used for x=0.20. This method will be applied to the $\sigma^2$ vs temperature plots for the U-Ru pair and U-U pair. These Debye fits are represented by the dashed red lines. Within the error of each data point, the Debye curve fits through all of the data nicely. The Debye fits for the U-Si peaks at each concentration are shown in Figure 6.12. The correlated Debye temperature is again very high ($\approx$ 600K), and the thermal contribution to $\sigma^2$ is therefor low; consequently the relative scatter appears high.

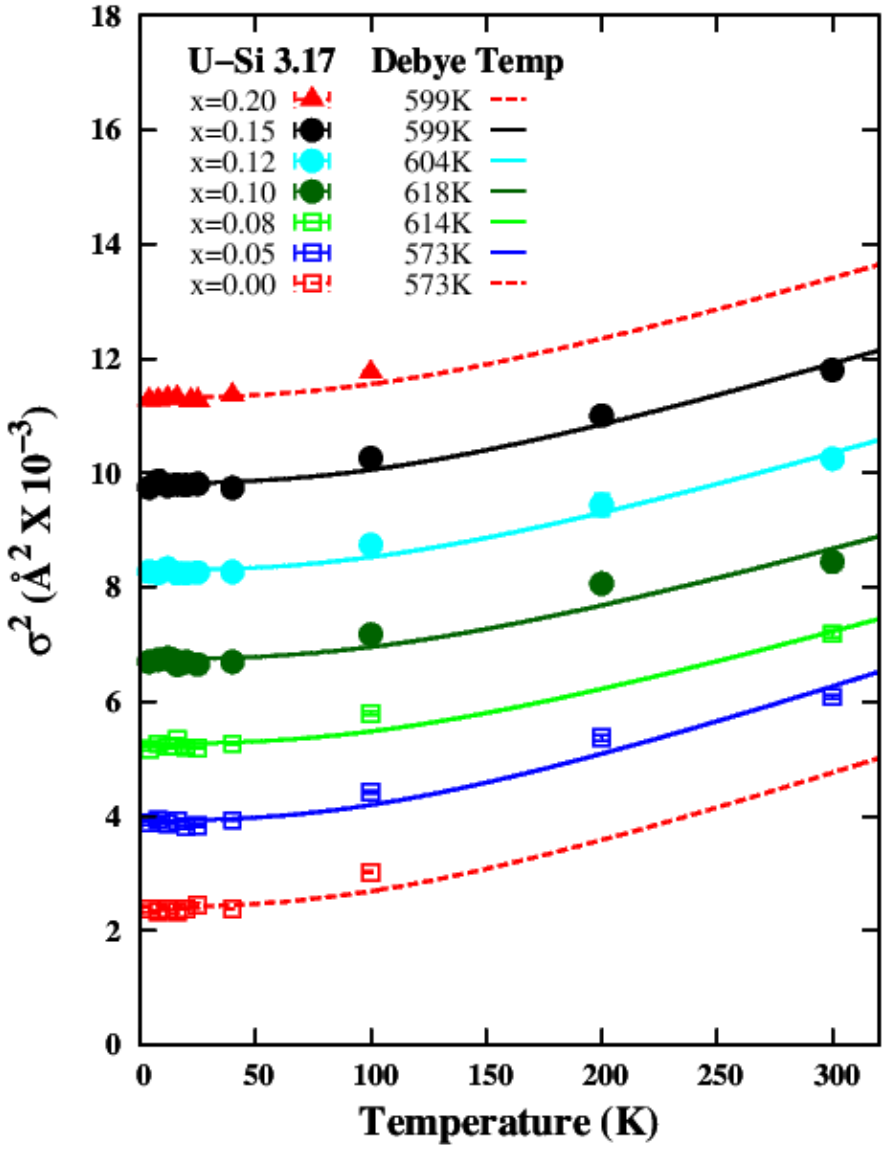


Figure 6.12: The Debye-Waller factor for each concentration of the first U-Si peak fit to the Debye model. The Debye curve was fit across all data points, and fit the low temperature data within the error of the data. No excess static disorder is seen.

The Debye fit for the U-Ru $\sigma^2$ vs temperature plot for all concentrations was fit from 90 K - 320 K. For a fit over entire temperature range, the 100 K and 200 K data points were below the Debye curve while the 300 K data point was always above the Debye curve. This is shown in Figure 6.13.

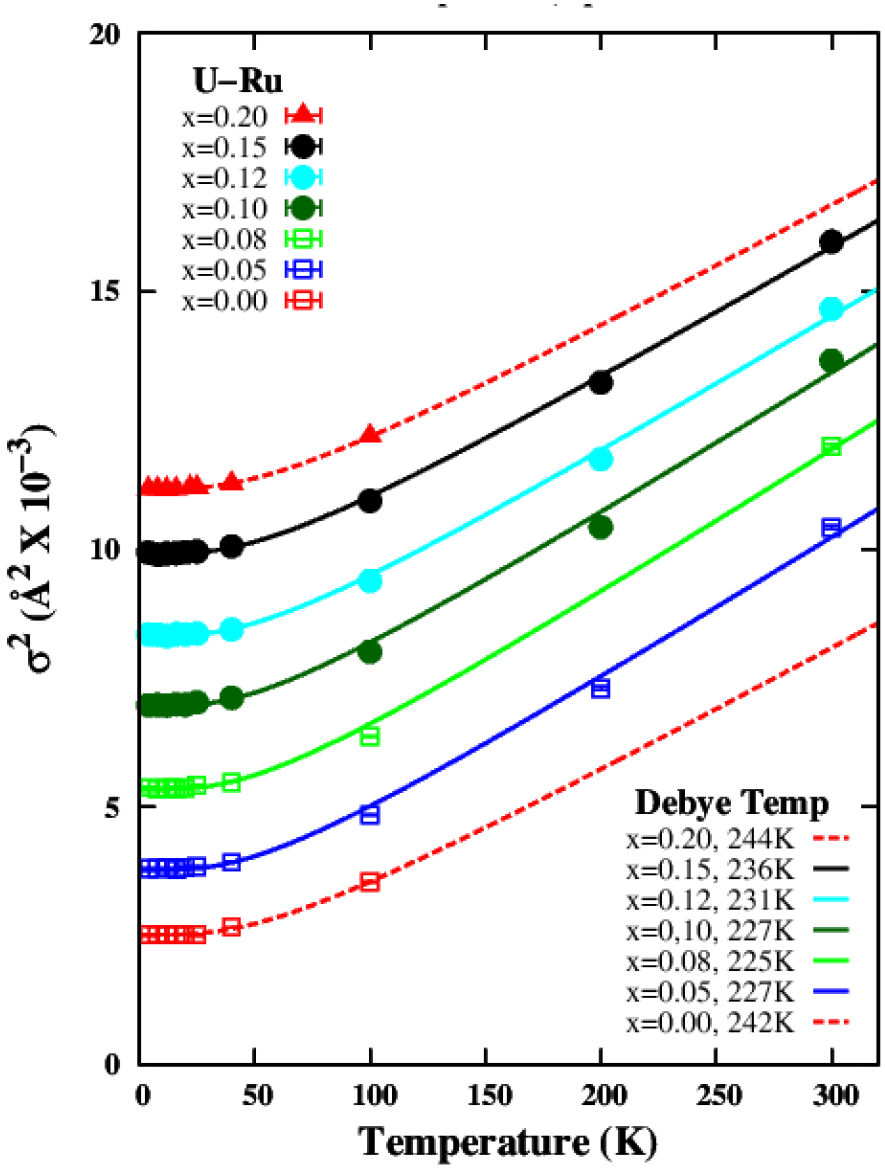


Figure 6.13: The Debye-Waller factor for each concentration of the first U-Ru peak fit to the Debye model from 0 K to 300 K. The 100 K and 200 K data points for each concentration are below the Debye curve and the 300 K data point for each concentration was always above the Debye curve.

The data were then fit to the Debye model in the range of 90 K to 320 K for the U-Ru peak at each concentration, as seen in Figure 6.14.

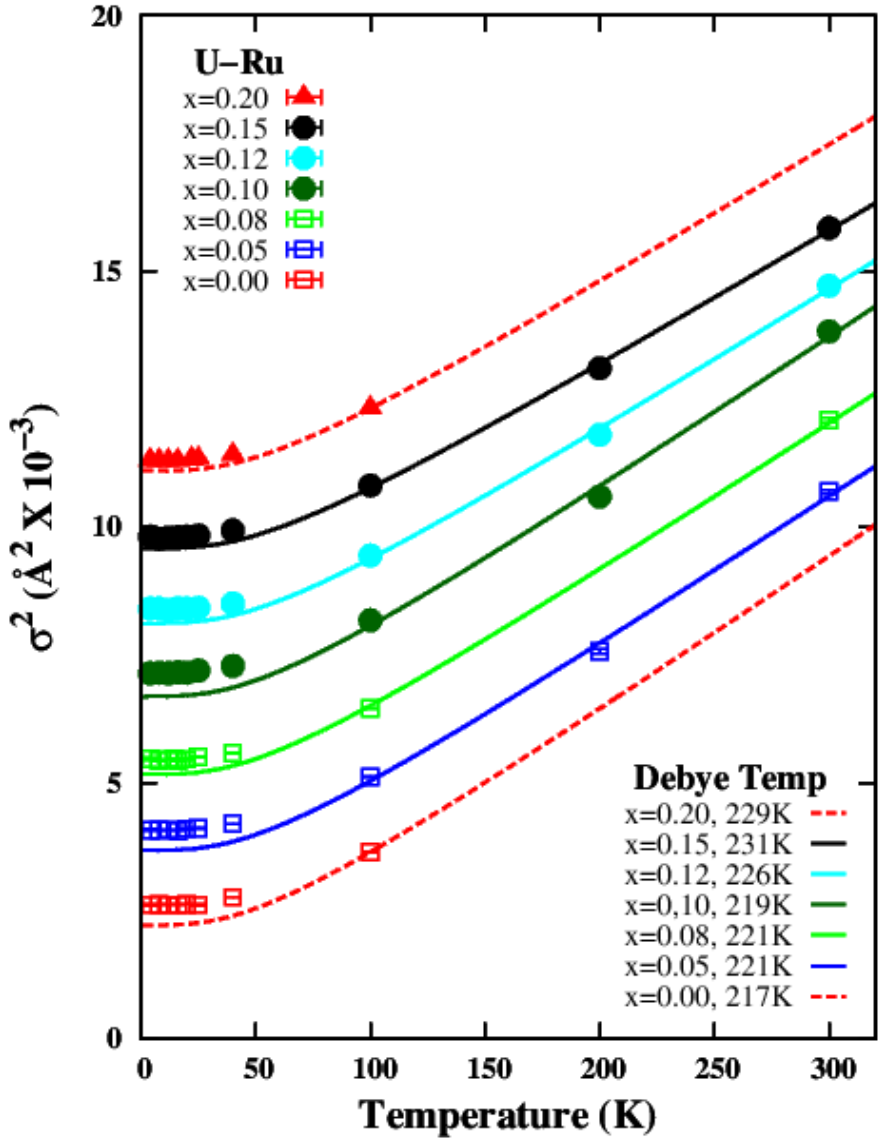


Figure 6.14: The Debye-Waller factor for each concentration of the first U-Ru peak fit to the Debye model. The Debye curve was fit across all data points from 90 K to 320K. The Debye curve deviates from the low temperature data, providing evidence of excess static disorder.

The Debye curve fits through all of the high temperature data nicely, within the error of each data point. However, the high temperature fit range again revealed some excess disorder that developed below roughly 70K; this in excess of the value $\sigma^2_{static}$

in Eq. 1.34. The Debye temperature for each concentration is given in the legend that is located in the bottom right corner of Figure 6.14.

The difference was taken between the $\sigma^2$ data points and the Debye curve at each concentration that has a 300 K data point, which is shown in Figure 6.15.

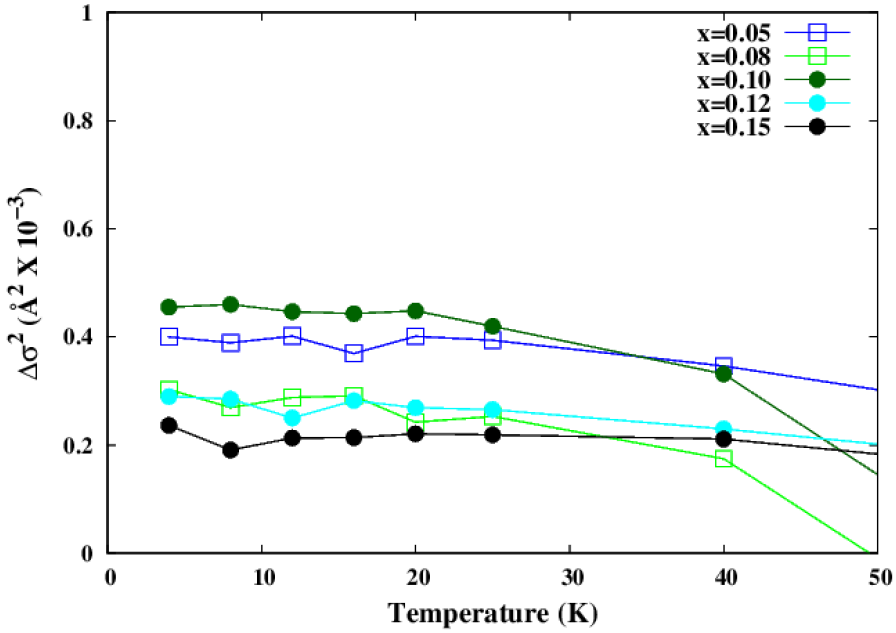


Figure 6.15: Difference between the $\sigma^2$ data points from the U-Ru peak and the Debye curve fit to them from 90 K to 320 K.

The excess disorder continuously increases as the temperature decreases, although very slightly below 25 K.

There were two Debye fits for the U-U $\sigma^2$ vs temperature plot. One of the fit ranges was from 0 K - 220 K. The Debye fits for the U-U peaks at each concentration for the fit range of 0 K - 220 K are shown in Figure 6.16. The variation of the data about the fit is similar to that for U-Ru and Ru-U.

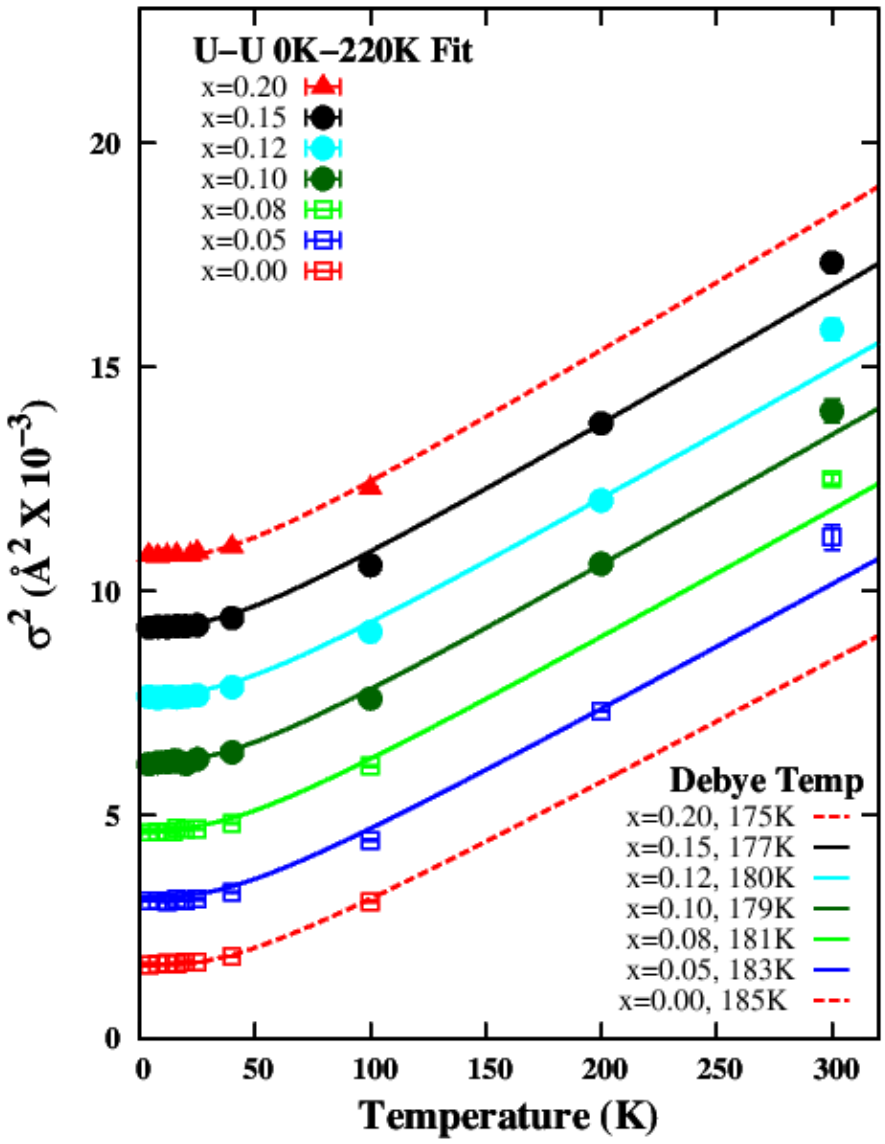


Figure 6.16: The Debye-Waller factor for each concentration of the first U-U peak fit to the Debye model. The Debye curve was fit across all data points from 0 K to 220 K, and fit the low temperature data within the error of the data.

The data point at 100 K tends to always be below the Debye fit, while the 300 K data point is above. This prompted a Debye fit done from 90 K to 320 K. The Debye fits for the U-U peaks at each concentration over this fit range is shown in Figure 6.17.

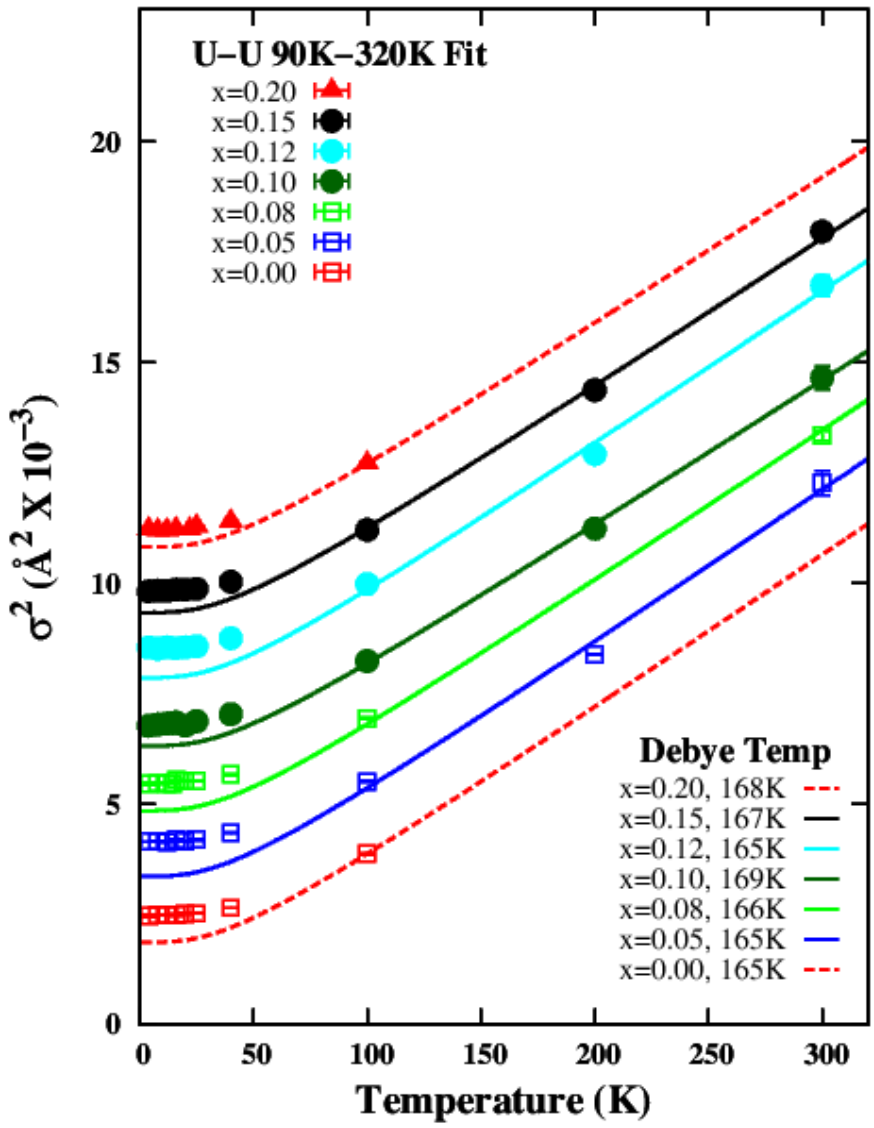


Figure 6.17: The Debye-Waller factor for each concentration of the first U-U peak fit to the Debye model from 90 K to 320K. The Debye curve follows the high T data well but deviates significantly below about 70K, indicating additional excess disorder.

The Debye curve fits the high temperature well, within the error of each data point. However, the excess disorder of the system that develops below 70 K as shown in Figure 6.17 is similar to the U-Ru Debye fit in Figure 6.14. The difference was taken between the $\sigma^2$ data points and the Debye curve at each concentration that has

a 300 K data point and is plotted in Figure 6.18.

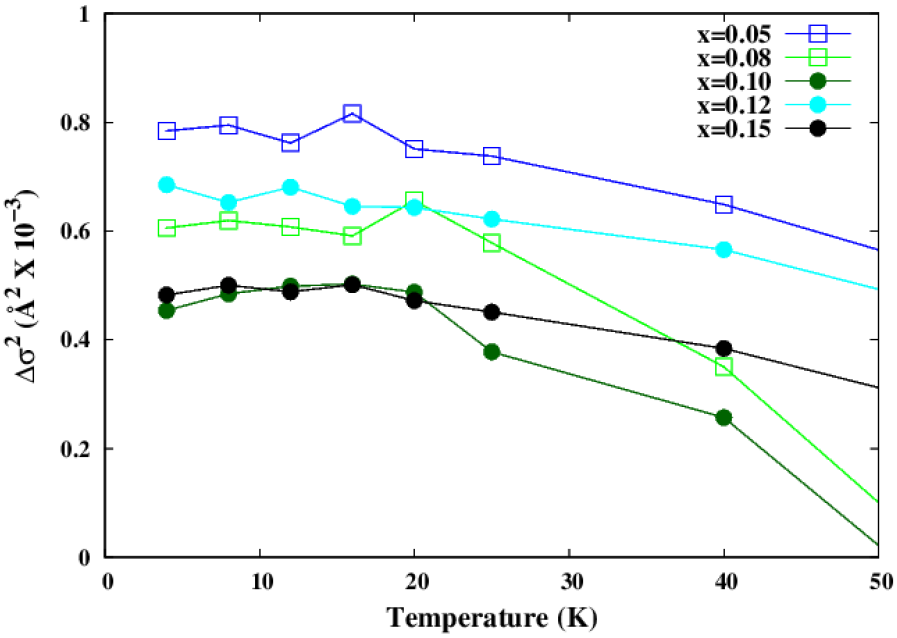


Figure 6.18: Difference between the $\sigma^2$ data points from the U-U peak and the Debye curve fit to them from 90 K to 320 K.

The excess disorder increases until around 15 K, where it levels off.

### Fe K Edge Debye-Waller Factor Plots

The Debye fit for the Fe-Si $\sigma^2$ vs temperature plot was fit from 0 K - 320 K for all concentrations. It is important to note that the Fe K edge data have much more scatter due to the poorer signal-to-noise ratio because of the low concentration of Fe. These Debye fits for Fe-Si are shown in Figure 6.19.

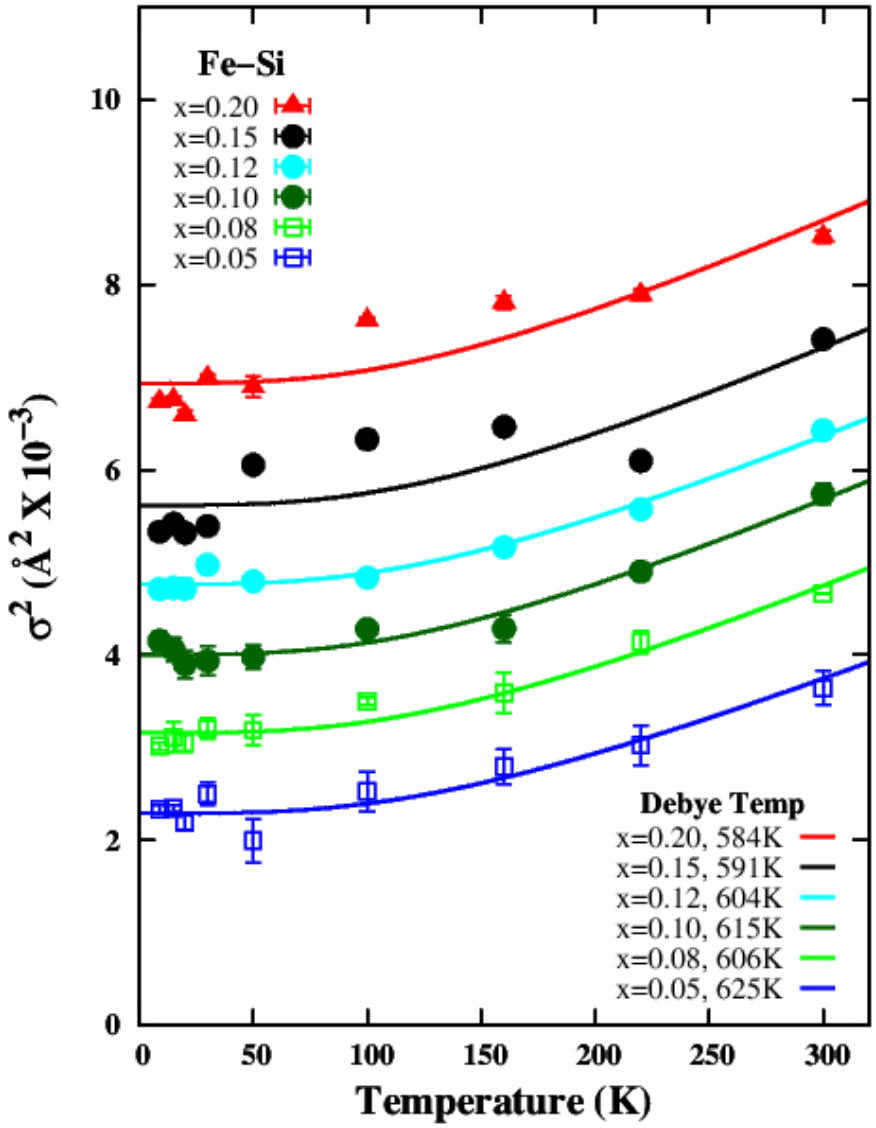


Figure 6.19: The Debye-Waller factor for each concentration of the first Fe-Si peak fit to the Debye model. The Debye curve was fit across all data points from 0 K to 320 K. The Debye curve fits the low temperature data within the scatter of the data.

The data for x=0.15 and x=0.20 are noisy and have large fluctuations where the cause for these have been undetermined. Despite the scatter in the data, the Debye curve fits reasonably over the entire temperature range. The Debye temperature for each concentration is given in the legend that is located in the bottom right corner of Figure 6.19. The correlated Debye temperature for the Fe-Si fluctuates around 600 K, while the Ru-Si correlated Debye temperature is over 700 K. This indicates that there is more thermal contribution in the Fe-Si pair than the Ru-Si pair, although both being stiff bonds.

The Debye fit for the Fe-Ru $\sigma^2$ vs temperature plot was fit from 0 K - 320 K for all concentrations. These Debye fits are shown in Figure 6.20.

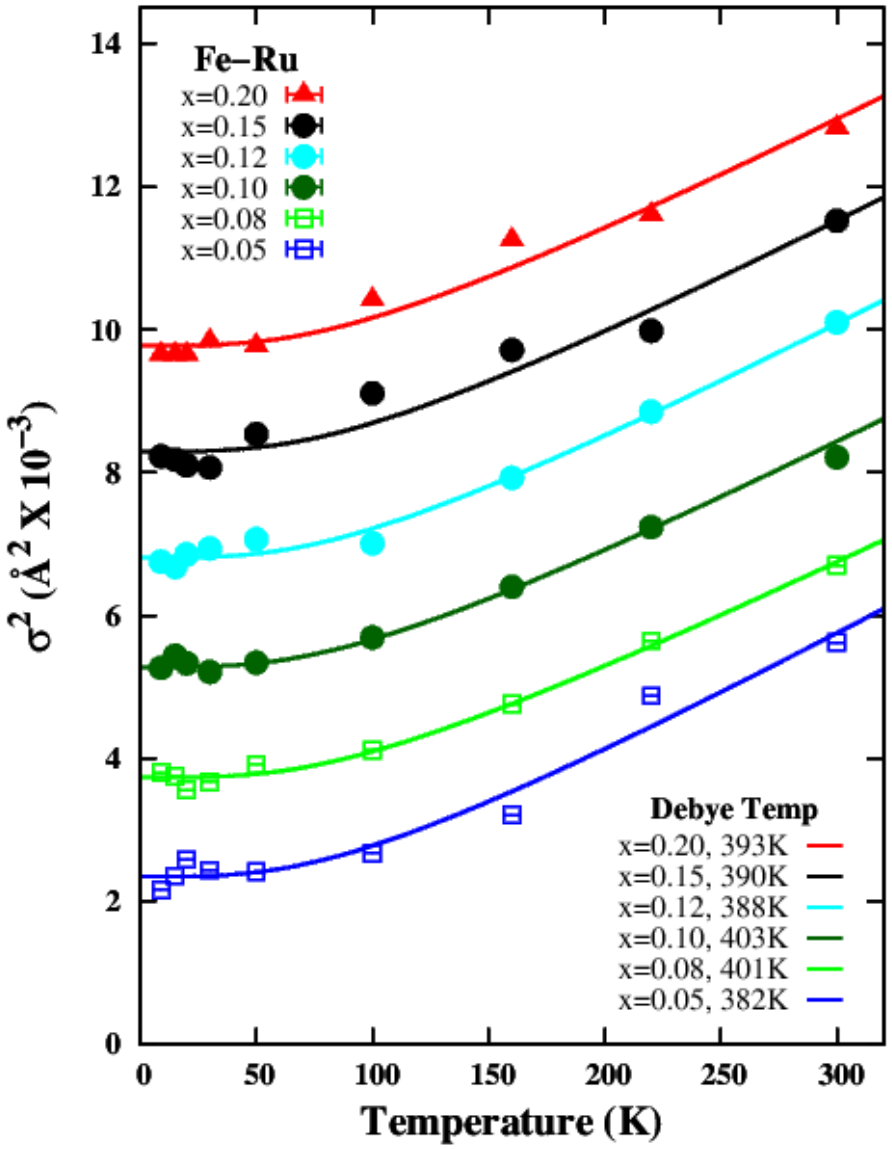


Figure 6.20: The Debye-Waller factor for each concentration of the first Fe-Ru peak fit to the Debye model. The Debye curve was fit across all data points from 0 K to 320 K. The Debye curve fits the low temperature data within the scatter of the data.

The low concentration of Fe in the samples result in considerable scatter in the data. The data for x=0.15 and x=0.20 are noisy and have large fluctuations, but not as much fluctuation as seen in the Fe-Si peaks. The Debye curve fits through all of the data points within the scatter and the Debye temperature for each concentration

is given in the legend that is located in the bottom right corner of Figure 6.20.

The Debye fit for the Fe-U $\sigma^2$ vs temperature plot was also fit from 0 K - 320 K for all concentrations, as shown in Fig 6.21. The 300 K data point for x=0.08 was significantly below the Debye curve fit, which caused the low temperature data to not be fit properly. The Debye fit for x=0.08 was done over the temperature range of 0 K to 240 K. The 220 K and 300 K data points had significant scatter for the Debye curve. These two data point were excluded in the Debye fit done for x=0.15. The Debye fits for the Fe-U peaks at each concentration are shown in Figure 6.21.

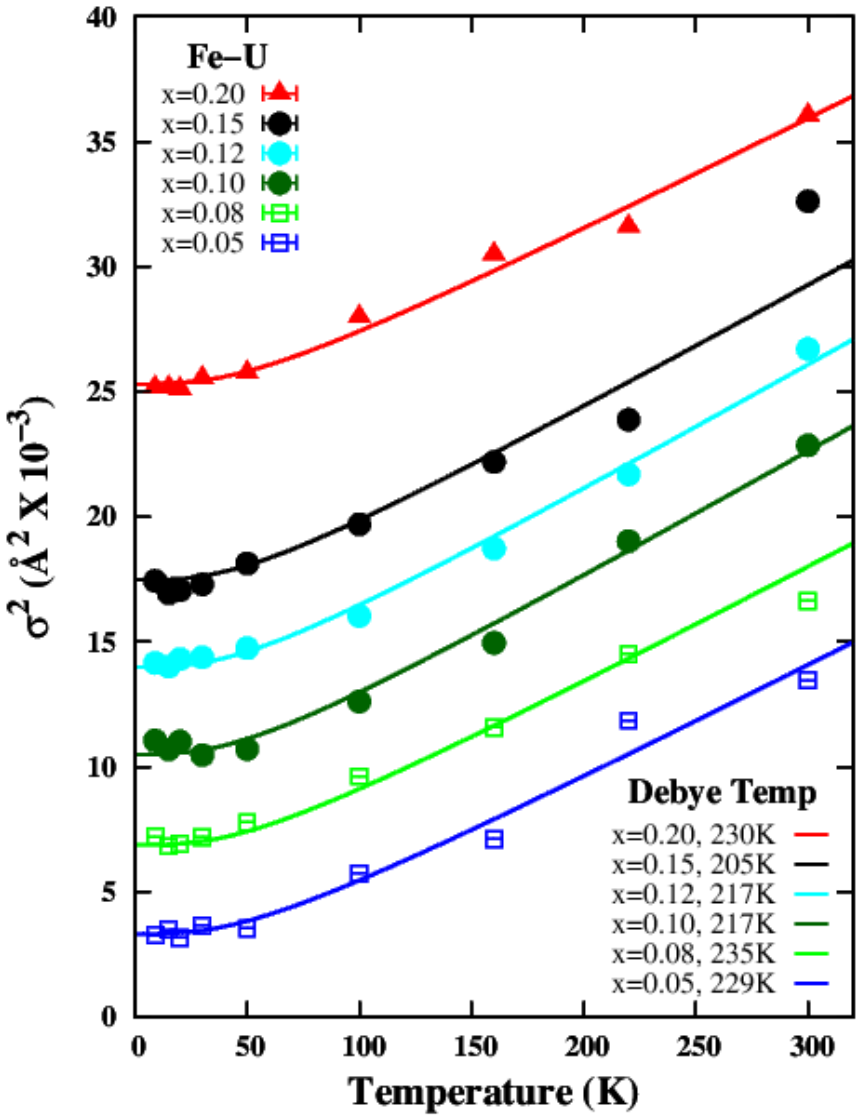


Figure 6.21: The Debye-Waller factor for each concentration of the first Fe-U peak fit to the Debye model. The Debye curve was fit across all data points from 0 K to 320 K. The Debye curve fits the low temperature data within the scatter of the data.

There is still some scatter due to a low concentration of Fe. The Debye curve fits through all of the data points within the scatter, and no excess disorder is seen. The Debye temperature for each concentration is given in the legend that is located in the bottom right corner of Figure 6.21.

# Chapter 7

# Discussion

We expected that the electronic structure that lead to the formation of a large localized U moment would appear in the U $L_{III}$ edge since the sample becomes AFM above a Fe concentration of x=0.1. However, the variation of the U $L_{III}$ edge in $URu_{2-x}Fe_xSi_2$ shows no clear change in the electronic configuration of U electrons as a function of x, both at low T and at 20 K, as seen in Figure 6.1. Any shift in the edge that is less than 0.1 eV is at the limit of our resolution.

Based on the small structure found in the Ru K edge XANES region, it might be that Ru plays a larger role in the HO/LMAFM phase than previously thought. The Fe edge in $URu_{2-x}Fe_xSi_2$ also depicts two possible anomalies that indicate small changes in the electronic structure about the Fe defect atoms.. Fe and Ru belong to the same group in the periodic table and show similar patterns in their electron configuration and in the XANES. This is seen by the anomaly that occurs around $\mu(E) \approx 0.94$ in both the Fe K edge and Ru K edge in Figure 6.2 and Figure 6.3, respectfully.

However, these changes in both absorption edges are close to the observational limit of the apparatus, and the Fe K edge has a poorer signal-to-noise ratio due to the low concentration of Fe.

The pair distance plots, which are given in Appendix D, reveal some useful information. The distance between U and each of its 3 nearest neighbors decreases by approximately 0.008 Å as temperature decreases from 300 K to around 10 K, as expected. The U-Si distance is found to be 0.02 Å below 3.1715 Å, the result from diffraction, while the other two remaining U pairs agree with the diffraction distance. A small effect due Fe doping on the Ru site is observed. The distance across all U-X pairs decrease by approximately 0.003 Å as the Fe concentration increases. At low temperatures, this distance varies for each U-X pair as the Fe concentration increases. The U-Si pair distance decreases by 0.004 Å, while the U-Ru and the U-U pair distances decrease by 0.003 Å. These effects are depicted in Figure D.1 - D.3

The pair distance plots of the Fe edge with its 3 nearest neighbors (Si, Ru, U) are seen in Figures D.4 - D.6. The distances are significantly shorter than the corresponding distances of Ru with its 3 nearest neighbors, since Fe is a smaller atom than Ru. The solid red line in Figures D.4 - D.6 portray the distance of Ru-X pairs at 300 K to show this result. At 300 K, the Fe-Si pair distance was 0.05 Å below the distance for Ru-Si, while both the Fe-Ru pair distance and the Fe-U pair distance were approximately 0.02 Å below the distance found by diffraction for the corresponding Ru-Ru bond and the Ru-U bond. This deviation from the Ru-X pair distances is evidence of the doping of Fe on Ru site acting as a chemical pressure [21]. Also, each Fe peak

exhibits thermal expansion since the distance between Fe and its 3 nearest neighbors decrease as temperature decreases. The $\sigma^2$ plots for the Fe K edge also confirm that Fe is on the Ru site since the Debye model fits reasonably.

The distance between Ru and its three nearest neighbors agree with the distance based on diffraction across all Fe concentrations at 300 K. Each Ru pair shows evidence for thermal contraction as temperature decreases. No noticeable change in pair distances is observed as the Fe concentration is increased. These pair distance plots are given by Figures D.7 - D.9.

The Ru-Si peak in the Ru K edge data has a high Debye temperature that decreases from 786 K to 713 K as x increases from 0 to 0.2. The Debye model fits the high temperature data well, but deviates from the low temperature data with an unusual excess static disorder of 0.0004 Å$^2$. For this pair, the $\sigma^2$ *increases* as temperature is lowered until around 25 K, whereas in all thermal vibration models, $\sigma^2$ must decrease as T is lowered. This indicates a split Ru-Si peak with two slightly different positions for the Ru atom.

The Ru-Ru peak in the Ru K edge data has an intermediate Debye temperature that changes little as x increases from 0 to 0.2. This is comparable to the Fe-Ru peak in the Fe K edge data, but about 15 K higher. The Debye curve fits through all the data well, with no evidence of excess disorder developing at low temperatures.

The Ru-U peak in the Ru K edge data has a low Debye temperature that is nearly constant as x increases from 0 to 0.2. The Debye curve fits the high temperature data well for the concentrations that have high temperature data through 300 K, but shows

excess static disorder of 0.0005 Å$^2$ at low temperatures. This indicates that the Ru-U peak is also likely split.

The U-Si peak in the U $L_{III}$ edge has a high Debye temperate that increases from 573 K to 599 K as x increases from 0 to 0.2. This high Debye temperature indicates a stiff bond between U and its nearest Si neighbor. The Debye curve fits reasonably well through all of the data, indicating no significant increase in local disorder for U-Si. Any structural distortion would keep this bond length nearly constant due to the very strong U-Si bond.

The U-Ru peak in the U $L_{III}$ edge has a fairly low Debye temperature that increases from 217 K to 229 K as x increases from 0 to 0.2. This indicated that there is a weak bond between U and its nearest Ru neighbor. The Debye curve fit the high temperature data well, but consistently deviates from the low temperature data by nearly the same amount for each sample. This indicates that there is excess static disorder in the system of 0.0004 Å$^2$, which implies that the U-Ru peak is slightly split.

The U-U peak in the U $L_{III}$ edge had a Debye fit done from 90 K to 320 revealed a low Debye temperature that is very consistent as x increases from 0 to 0.2, which indicates a weak effective bond between U atoms. The Debye model fits the high temperature data well, but deviates from the low temperature data with excess disorder developing below 70 K of 0.0005 Å$^2$. This again would imply that the U-U pair distribution is also slightly split.

The Fe-Si peak in the Fe K edge has a high Debye temperature that decreases

from 625 K to 584 K as x increases from 0 to 0.2, which is lower than the Debye temperature for from the corresponding Ru-Si peak in the Ru K edge by about 150 K. There is scatter in the data caused by the low concentration of Fe in each sample; However, the Debye curve fits the data quite well when considering the larger scatter for the Fe edge. There is no significant excess static off-set at low temperature. The x=0.15 and x=0.20 concentrations are noisy and have large fluctuations at the 100 K and 160 K data points. This might be caused by the incident monochromatic X-ray beam not being centered on the sample. However, this also could possibly be a physical effect of the system. This could be resolved with more high temperature data of the Fe K edge.

The Fe-Ru peak in the Fe K edge data has a Debye temperature that increases from 382 K to 393 K as x increases from 0 to 0.2. This is comparable to the Debye temperature of the Ru-Ru peak in the Ru K edge. There is scatter in the data that is due to the low concentration of Fe in each sample. The Debye curve fits through all of the data points well, without showing any evidence of excess disorder at low temperature.

The Fe-U peak in the Fe K edge data has a low Debye temperature that fluctuates as x varies from 0 to 0.2. This is comparable to the Ru-U peak in the Ru K edge, but slightly higher. The Debye model fits well to this peak, with no evidence of static disorder in the system.

The Debye temperature for each peak was determined from fitting the $\sigma^2$ data points to the Debye model, which allows for the effective spring constant for atom

pairs to be found, as discussed in Section 1.6 and Section 1.7. The Debye fit for each Ru K edge and U $L_{III}$ edge pair was extended to cover the range from 0K to 1500K in order to obtain the slope at high T. The bond strength was determined from this slope by

$$\kappa = \frac{k_B T}{\sigma^2} \tag{7.1}$$

where $k_B$ is the Boltzmann constant, T is the temperature and $\sigma^2$ is the Debye-Waller factor.

The effective spring constant of the Ru-Si pair dominates the dynamics of the local structure compared to the other effective spring constants of the other atom pairs. The Ru-Si effective spring constant also decreases as the Fe concentration increases. This is attributed to the replacement of Ru with Fe in the system. The Ru-Ru pair remains almost constant, aside from the slight decrease due to the replacement of Fe on Ru sites in the structure. The effective spring constants of the Ru-Si, Ru-Ru, and Ru-U pairs are given in Table 7.1.

Table 7.1: Ru Effective Spring Constant to Nearest Neighbors

| Concentration | Ru-Si Effective Spring Constant (eV/Å$^2$) | Ru-Ru Effective Spring Constant (eV/Å$^2$) | Ru-U Effective Spring Constant (eV/Å$^2$) |
|---|---|---|---|
| 0.00 | 11.3 | 7.0 | 2.4 |
| 0.05 | 10.6 | 6.9 | 2.4 |
| 0.08 | 10.4 | 6.9 | 2.5 |
| 0.10 | 10.3 | 6.9 | 2.5 |
| 0.12 | 10.0 | 6.8 | 2.5 |
| 0.15 | 9.7 | 6.8 | 2.6 |
| 0.20 | 9.3 | 6.7 | 2.7 |

The effective spring constant of the U-Si pair appears to vary around 6.1 eV/Å$^2$.

The effective spring constant increases from x=0.00 until it reaches a maximum value at x=0.10, where it then decreases. The lack of high temperature data at x=0.00, x=0.08, and x=0.20 may be the cause this variation. The effective spring constant of the U-Ru pair and of the Ru-U pair are comparable to one another. The values of the U-X effective spring constants are given in Table 7.2.

Table 7.2: U Effective Spring Constant to Nearest Neighbors

| Concentration | U-Si Effective Spring Constant (eV/Å$^2$) | U-Ru Effective Spring Constant (eV/Å$^2$) | U-U Effective Spring Constant (eV/Å$^2$) |
|---|---|---|---|
| 0.00 | 5.7 | 2.7 | 2.3 |
| 0.05 | 5.6 | 2.8 | 2.3 |
| 0.08 | 6.5 | 2.8 | 2.4 |
| 0.10 | 6.6 | 2.7 | 2.5 |
| 0.12 | 6.2 | 2.9 | 2.4 |
| 0.15 | 6.1 | 3.0 | 2.4 |
| 0.20 | 6.0 | 3.0 | 2.5 |

The effective spring constant of the Fe-Si pair decreases as more Fe is introduced into the system. This is similar behavior for the effective spring constant of the Ru-Si pair. The effective spring constant of the Fe-Ru pair remains consistent around 5 ev/Å$^2$. Compared to that of the Ru-Ru pair, the Fe-Ru pair is slightly weaker, but appears to follow the same trend of increasing from x=0.00 to x=0.10, then decreasing. Table 7.3 shows the effective spring constant for Fe and its 3 nearest neighbors.

Table 7.3: Fe Effective Spring Constant to Nearest Neighbors

| Concentration | Fe-Si Effective Spring Constant (eV/Å$^2$) | Fe-Ru Effective Spring Constant (eV/Å$^2$) | Fe-U Effective Spring Constant (eV/Å$^2$) |
|---|---|---|---|
| 0.05 | 7.4 | 4.7 | 1.9 |
| 0.08 | 6.8 | 5.1 | 1.8 |
| 0.10 | 7.0 | 5.1 | 1.7 |
| 0.12 | 6.7 | 4.7 | 1.7 |
| 0.15 | 6.5 | 4.8 | 1.7 |
| 0.20 | 6.4 | 4.9 | 1.9 |

The effective spring constant of the U-Ru pair and of the Ru-U pair are comparable to one another. Also, the core atoms that have U as its nearest neighbor also have the weakest effective spring constant. This implies that these pairings will be distorted when some excess disorder is in the system.

The $\sigma^2$ vs temperature plots allow for distortions of the local structure of $URu_{2-x}Fe_xSi_2$ to be observed. The Ru-Ru pair and the U-Si pair do not have excess disorder at low temperature. The Ru-Si pair has a significant increase in $\sigma^2$ at low temperature below 70 K which continues to increase until 20 K and the excess disorder at low temperatures shows evidence of a split Ru-Si peak. The Ru-U, U-Ru, and U-U pairs show a comparable increase in disorder at low temperature. A model of the local structure distortion must accommodate these observations.

First, one needs a distortion that does not significantly change the Ru-Ru or U-Si pair distances; these distortions must be accommodated by bond angle bending. A distortion that will do this is an orthorhombic distortion in which the b-axis is lengthened and the a-axis shortened, or vice versa. An example is shown in Fig 7.1 for the Ru-Ru pairs and U-Si pairs, where the displacements of the Ru or U

atoms relative to the center of the square cross-section of the original tetragonal unit cell. The displacements of Ru along the c-axis would be perpendicular to the Ru-Ru distance and would also not change the Ru-Ru distance. Note that an orthorhombic distortion at 45 deg would not work as it would require for example a compression of two Ru-Ru distance and a lengthening of the other two.

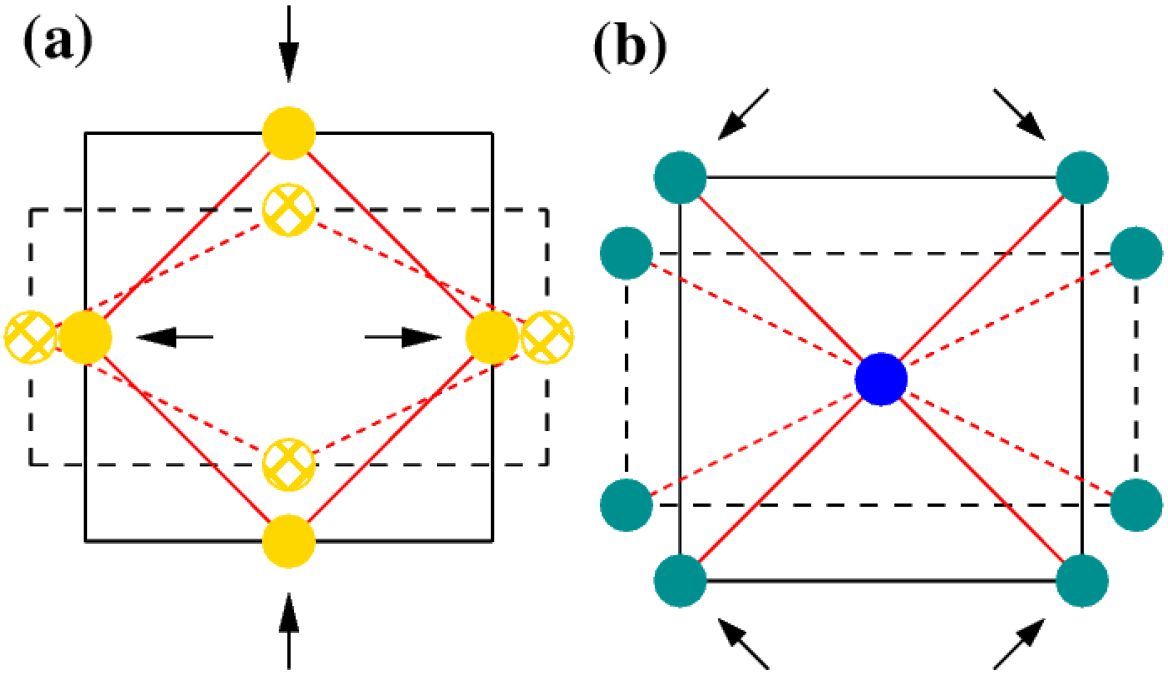


Figure 7.1: Orthorhombic distortion of the Ru-Ru pair (a) and the U-Si pair (b). The distance between the nearest Ru-Ru pair and the nearest U-Si remain constant.

This same orthorhombic distortion must be maintained for the Ru-Si pair. The stiff Ru-Si bond, which is given in Table 7.1, suggests that the Ru atom may move up or down along the c-axis. There are two Ru-Si bonds in the a-c plane and two in the b-c plane. See Figure 1.11. Figure 7.2 depicts the two different possibilities for the local distortion of the Ru atom.

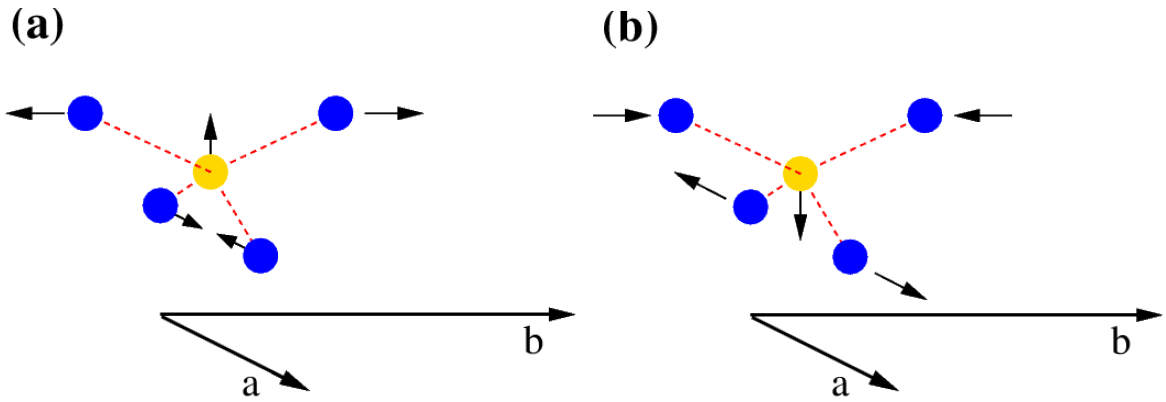


Figure 7.2: Orthorhombic distortion of the Ru-Si pair. The Si atoms (blue) will either move together or move apart which dictates the displacement of the Ru atom (yellow) along the c-axis. (a) shows the two Si atoms along the a-axis (a-c plane) to move together, pushing the Ru atom up; similarly the separation of Si atoms along the b-axis also shifts the Ru atom up. (b) shows the case to cause the Ru atom to shift down along the c-axis.

The two Ru-Si bonds below the local Ru atom will either compress (move closer together) or be under tension (move apart), while the two Ru-Si pairs above the local Ru atom will have the opposite behavior. Figure 7.2a shows the bottom two Ru-Si pairs under compression where the two Si atoms move closer together, and the top two Ru-Si pairs under tension where the Si atoms move further apart. This will cause the Ru atom to be displaced upwards on the c-axis. Figure 7.2b shows the opposite distortion that causes the Ru atom to be distorted downwards on the c-axis. Thus the local structure is distorted from a tetragonal local structure to an orthorhombic local structure where two slightly different Ru-Si bond lengths are expected. Note that this orthorhombic distortion also produces a splitting of the U-U distances, two pairs become shorter and two longer.

From the results discussed above, a model of the distortion of the system was able

to be constructed where the top half of the unit cell is depicted in Figure 7.3 below.

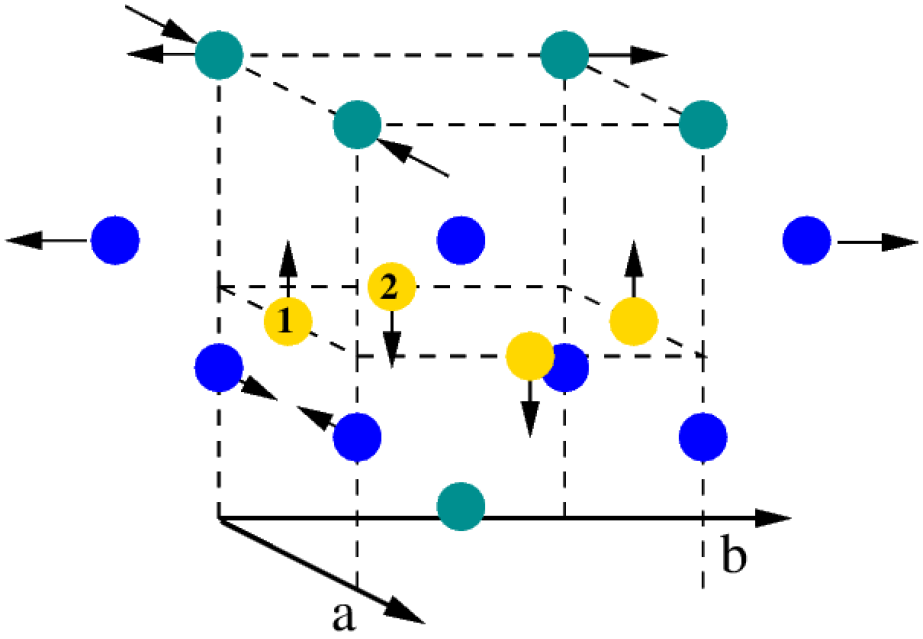


Figure 7.3: Top half of the unit cell for $URu_2Si_2$. The green spheres represent U. The yellow spheres represent Ru. The blue spheres represent Si. The arrows dictate the direction where each atom will travel as the temperature decreases, based on the long axis of the orthorhombic distortion – here the b-axis. This results in a shift in the ab-plane from a square to a rectangle. The elongation of the unit cell may occur in either the a-axis or the b-axis.

If this were to occur locally in an ordered way, the left and right Ru atom (Ru 1) in Figure 7.3 would move in the same direction, up, while the front and back Ru atoms (Ru 2) would move in the opposite direction, down. This is similar to distortion of the Ru and Si atoms due to the $B_{1g}$ phonon mode found by Buhot et al. (2015) [25]. We don't know if all Ru-Si bonds become split or only a fraction of them. The up and down displacements break 4-fold rotation symmetry which has been reported in Raman experiments such as that by Buhot et al. 2015. When there are two possible positions for an atom which are occupied randomly, that introduces entropy $k_B$ ln(2)

per atom. If all entropy were removed then the change in entropy at low temperature per mole would be 2R ln(2). The observed change for x = 0.00 is about 0.2 R ln(2) and it increases to about 0.4 R ln(2) [21]. Figure 7.3 clearly shows how the a-b plane will evidently shift from a square to a rectangle on local scale. The U-U pair will have excess disorder in this model, which is seen in Figure 6.17. Therefore two U will move together while the other two will move apart. In Figure 7.3, the U-U pair in the b-c plane will move apart and the U-U pair in the a-c plane will move together. The cause of this distortion is unknown. However, a random mix of these distorted unit cells on the scale of a few nanometers may still cause the sample to appear tetragonal in X-ray diffraction experiments.

# Chapter 8

# Conclusion

The XANES study of $URu_{2-x}Fe_xSi_2$ shows that no clear evidence for significant changes in the electronic structure were observed for all three atomic edges; However, there are tiny changes in the electronic structure for the Fe K edge and the Ru K edge. These anomalies suggest that Ru might play a larger role in the LMAFM phase transition than previously expected. More data will be taken to investigate the structure found in the Ru K edge and the Fe K edge.

The Ru K edge pair distance plots as a function of temperature showed that the distance between Ru with its three nearest neighbors (Si, Ru, and U) remained consistent with the distances determined by diffraction. The Fe K edge pair distances are shorter than the corresponding pair distances for Ru and its 3 nearest neighbors. For example the Fe-Si bond distance is about 0.05 Å shorter than Ru-Si bond distance. This shortening of the Fe-X distances is consistent with the concept of a chemical pressure effect. In addition, as the temperature decreases, the distance between the

Fe atom and its three nearest neighbors (Si, Ru, and U) all decreases as expected for thermal contraction. The U $L_{III}$ edge pair distances also decrease as temperature decreases, but deviate slightly from the distances found by diffraction.

Evidence of excess disorder was found in the Ru-Si, Ru-U, U-Ru, and U-U pairs. The Ru-Si pair had a significant increase in $\sigma^2$ at low temperature from around 70 K to around 25 K, which provides evidence of a split Ru-Si peak. The Ru-Ru and U-Si pairs did not show any evidence of excess disorder at low temperatures, indicating that their bond lengths stay essentially constant as the local structure is distorted. Based on these results, a distortion model of $URu_{2-x}Fe_xSi_2$ was created. It was found that the tetragonal structure distorted into an orthorhombic structure, where the square a-b plane changed into a rectangular base. However, the determination of whether the a-axis lengthens or contracts is unable to be determined since EXAFS focuses on only the local structure of the material. If this occurs randomly, the material would still appear to have a tetragonal structure in X-ray diffraction experiments.

Some concentrations in the U edge data and the Ru edge data lacked data in the high temperature range. We plan to collect more data for all absorption edges discussed in this thesis in the near future, especially in the high temperature range. More high temperature data would determine more accurate fits to the Debye model for the $\sigma^2$ data, especially regarding the U-U pair to better determine the observed excess disorder at low temperature. This could also possibly help determine if the fluctuations in the Fe K edge data in the intermediate temperature range were caused by excess noise during the data collection process, or if it is a real effect.

# Appendix A

# Theoretical Simulations

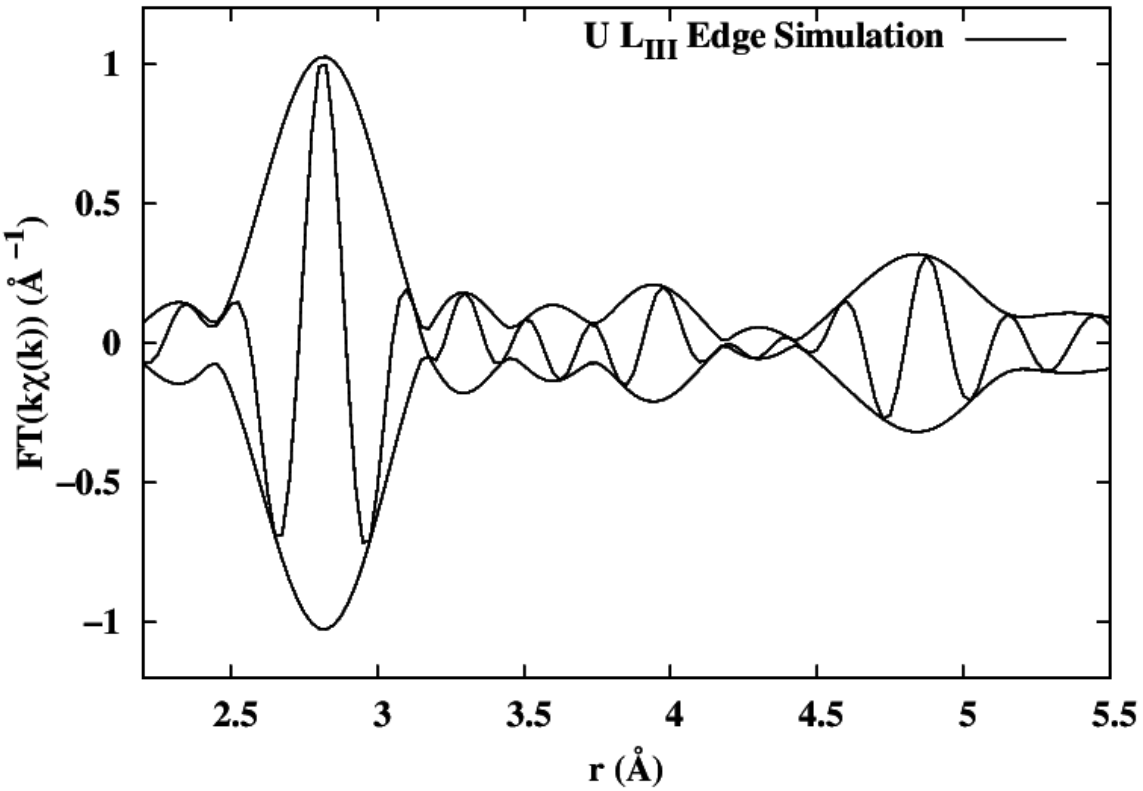


Figure A.1: Theoretical simulation of the U $L_{III}$ absorption edge created by the FEFF program.

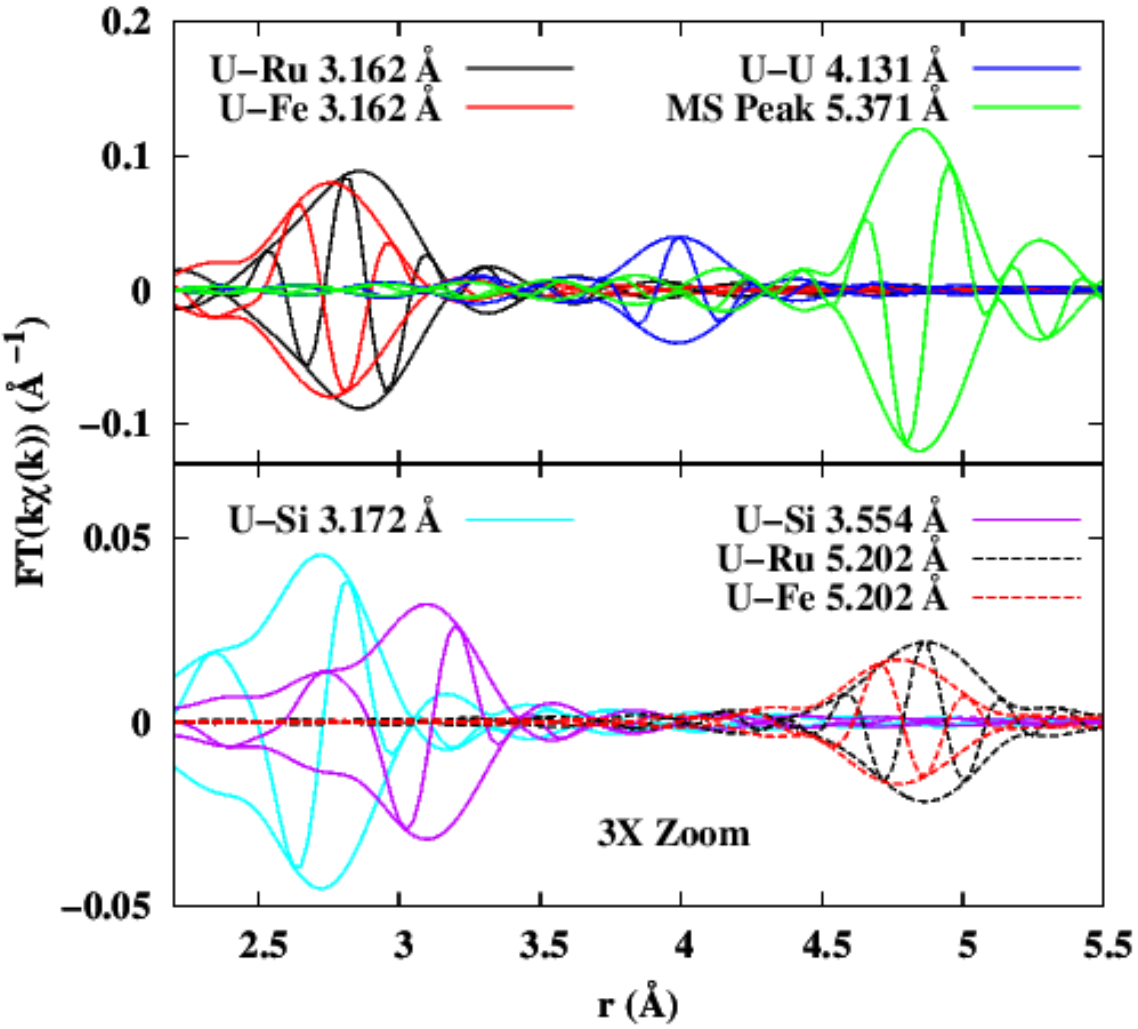


Figure A.2: The 8 standard files used to fit the transmission data of the U edge. The U-Ru peak at 3.162 Å is depicted as the solid black line. The U-Fe peak at 3.162 Å is depicted as the solid red line. The U-U peak at 4.131 is depicted as the solid blue line. A multiscattering (MS) peak at 5.371 Å, where the photoelectron scatters first off of Si, then off of Ru, is depicted as the solid green line. The U-Si peak at 3.172 Å is depicted as the solid cyan line. The U-Si (second closest Si neighbor) at 3.554 Å is depicted as the solid magenta line. The U-Ru (second closest Ru neighbor) at 5.202 Å is depicted as the dashed black line. The U-Fe (second closest Fe neighbor) at 5.202 Å is depicted as the dashed red line. Except for the MS peak, all plotted peaks are for one neighbor.

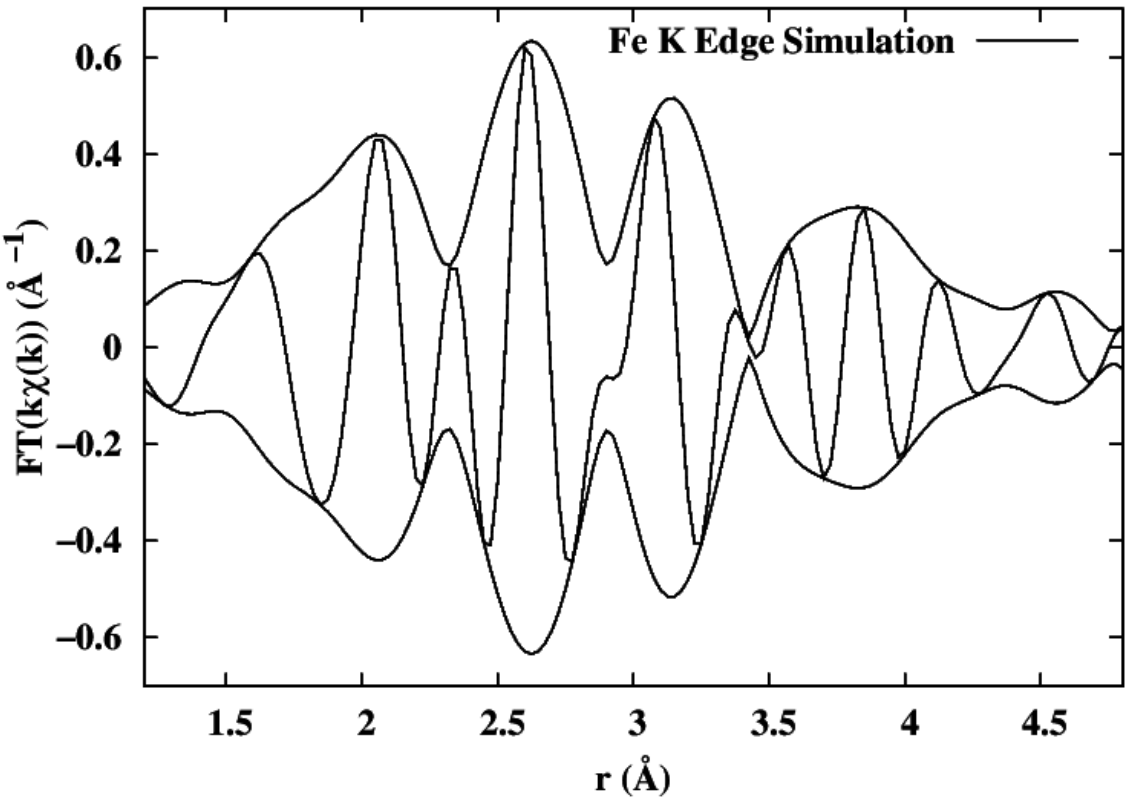


Figure A.3: Theoretical simulation of the Fe edge created by the FEFF program.

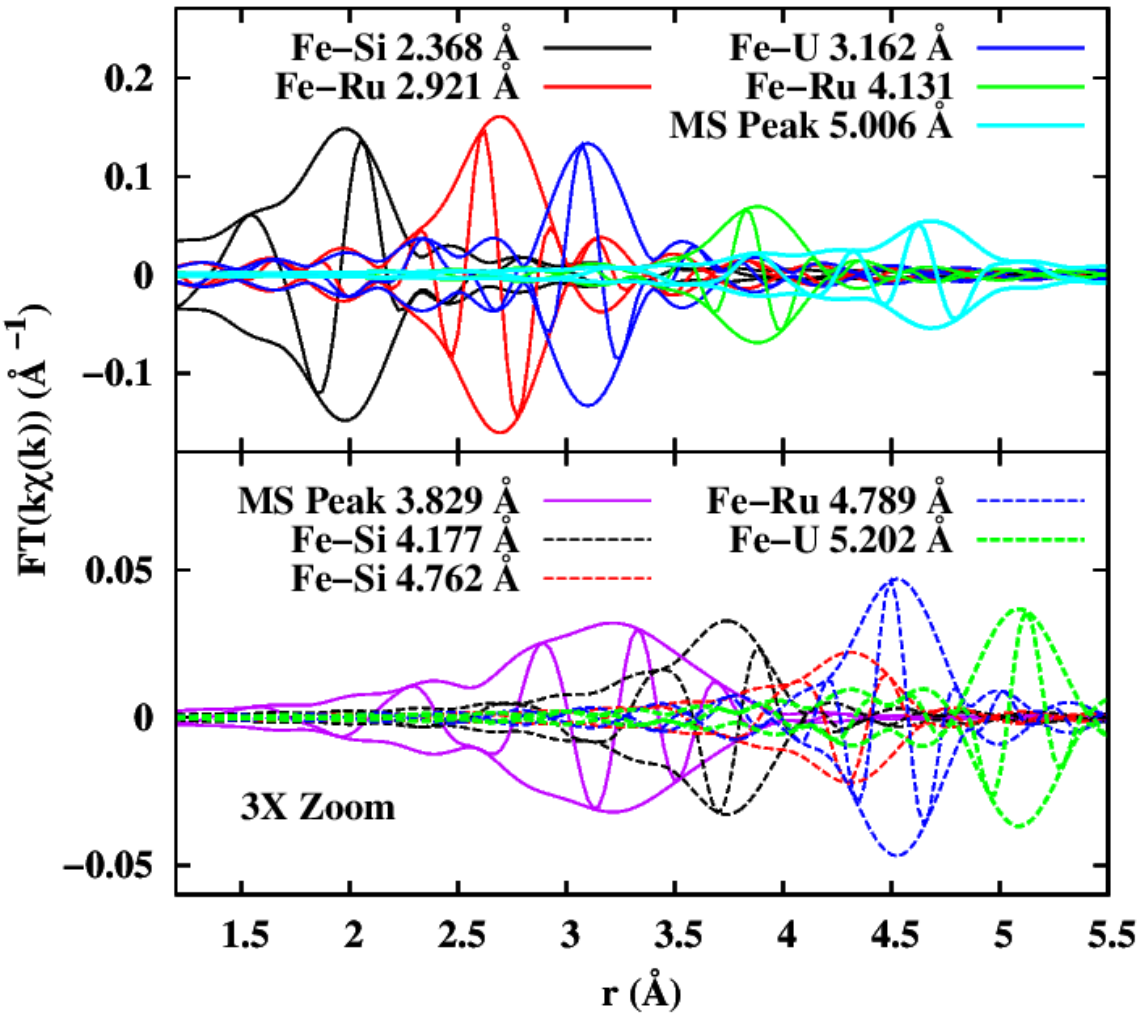


Figure A.4: The 10 standard files used to fit the fluorescence data of the Fe edge. The Fe-Si peak at 2.368 Å is depicted as the solid black line. The Fe-Ru peak at 2.921 Å is depicted as the solid red line. The Fe-U peak at 3.162 Å is depicted as the solid blue line. The Fe-Ru peak at 4.131 Å (second closest Ru neighbor) is depicted as the solid green line. A combination of two muliscattering (MS) peaks located at 5.006 Å is depicted as the solid cyan line. A MS peak at 3.829 Å, where the photoelectron scatters first off of Si, then off of Ru, is depicted as the solid magenta line. The Fe-Si peak at 4.177 Å (second closest Si neighbor) is depicted as the dashed black line. The Fe-Si peak at 4.762 Å (third closest Si neighbor) is depicted as the dashed red line. The Fe-Ru peak at 4.789 Å (third closest Ru neighbor) is depicted as the dashed blue line. The Fe-U peak at 5.202 Å (second closest U neighbor) is depicted as the dashed green line. Except for the MS peaks, all plotted peaks are for one neighbor.

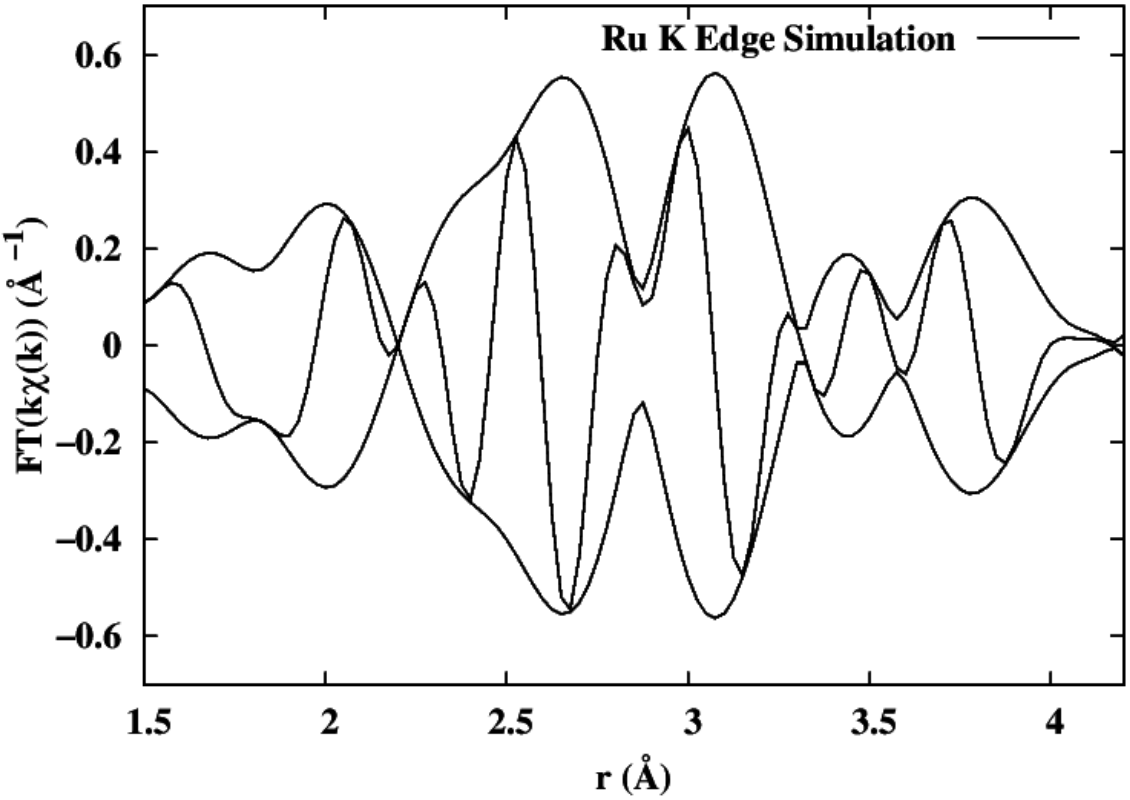


Figure A.5: Theoretical simulation of the Ru edge created by the FEFF program.

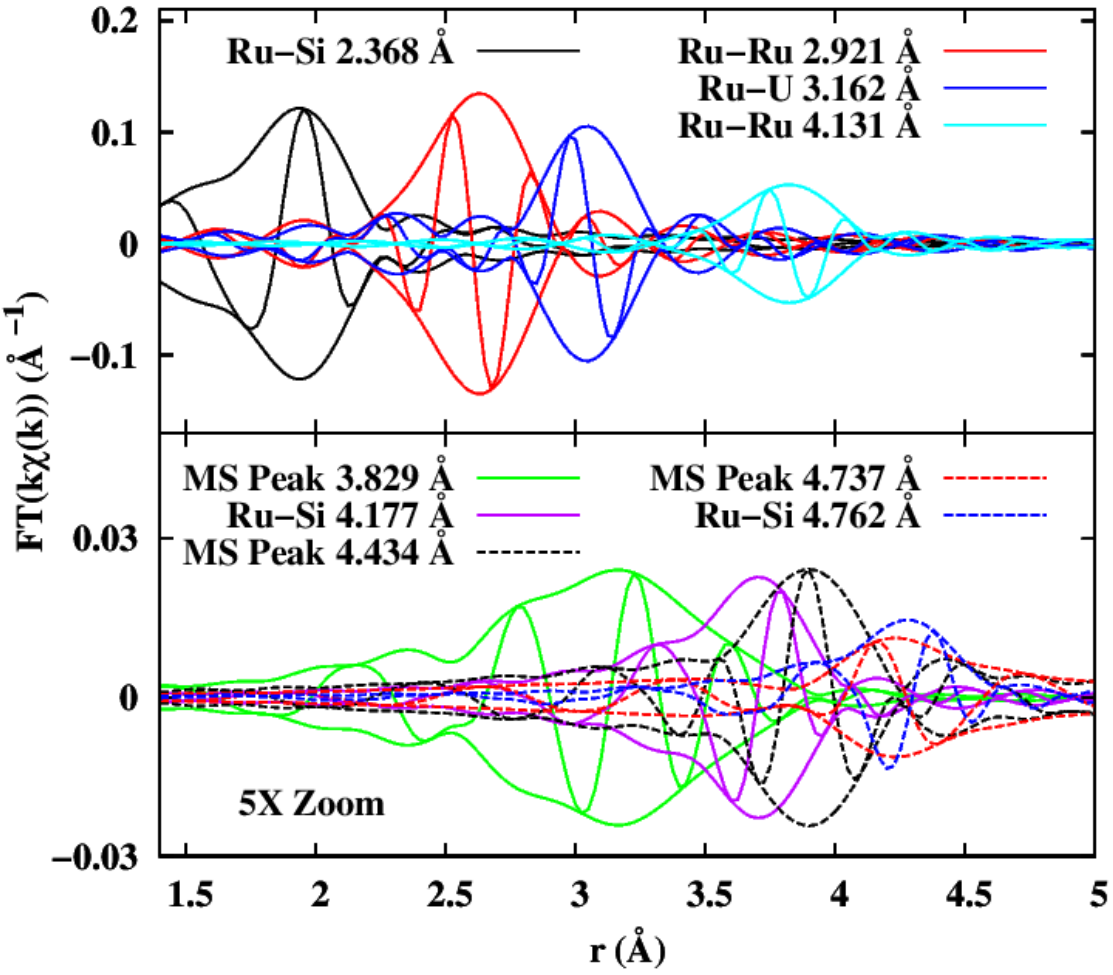


Figure A.6: The 9 standard files used to fit the transmission data of the Ru edge. The Ru-Si peak at 2.368 Å is depicted as the solid black line. The Ru-Ru peak at 2.921 Å is depicted as the solid red line. The Ru-U peak at 3.162 Å is depicted as the solid blue line. The Ru-Ru peak at 4.131 Å (second closest Ru neighbor) is depicted as the solid cyan line. A muliscattering (MS) peak at 3.829 Å, where the photoelectron scatters first off of Si, then off of Ru, is depicted as the solid green line. The Ru-Si peak at 4.177 Å (second closest Si neighbor) is depicted as the solid magenta line. A MS peak at 4.434 Å, where the photoelectron scatters first off of Si, then off of Ru, is depicted as the dashed black line. A MS peak at 4.737 Å, where the photoelectron scatters first off of Si, then off of Ru, then finally off of Si is depicted as the dashed red line. The Ru-Si peak at 4.762 Å (third closest Si neighbor) is depicted as the dashed blue line. Except for the MS peak, all plotted peaks are for one neighbor.

# Appendix B

# Data Reduction of the Ru K Edge

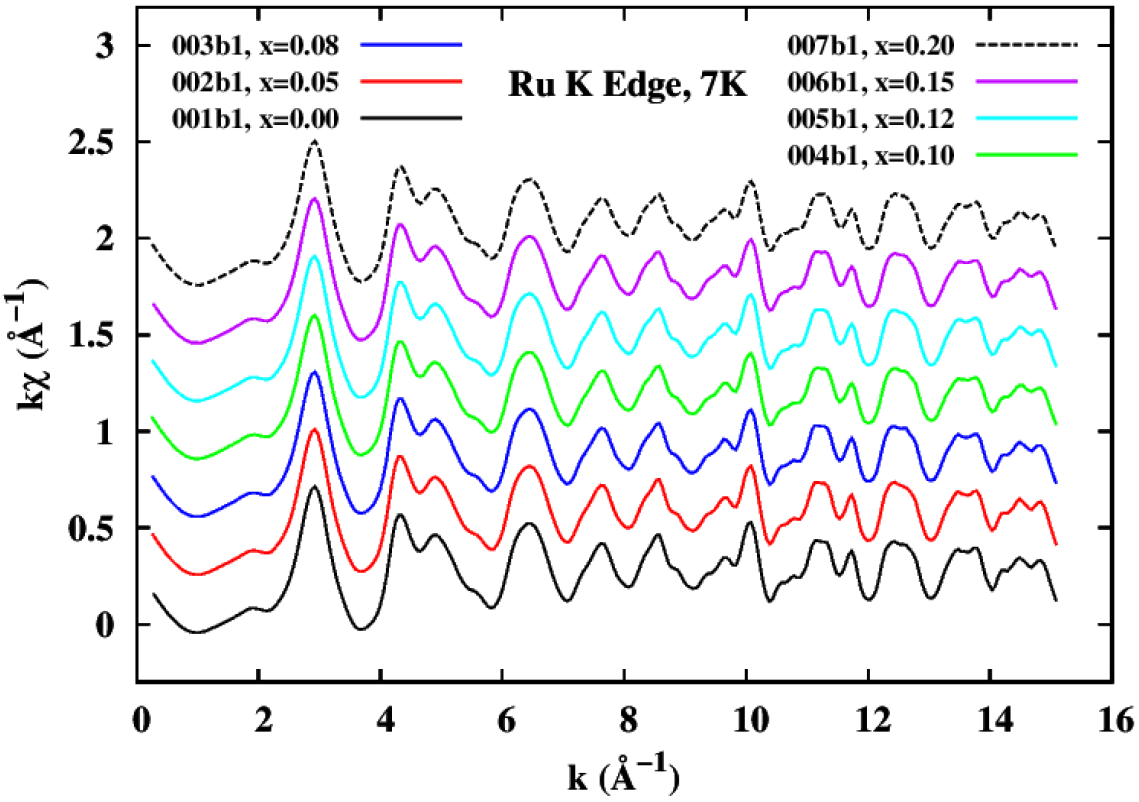


Figure B.1: Ru K absorption edge transmission data converted into k-space. This procedure is discussed in Section 4.1. The data depicted was taken at 7 K with no Fe concentration.

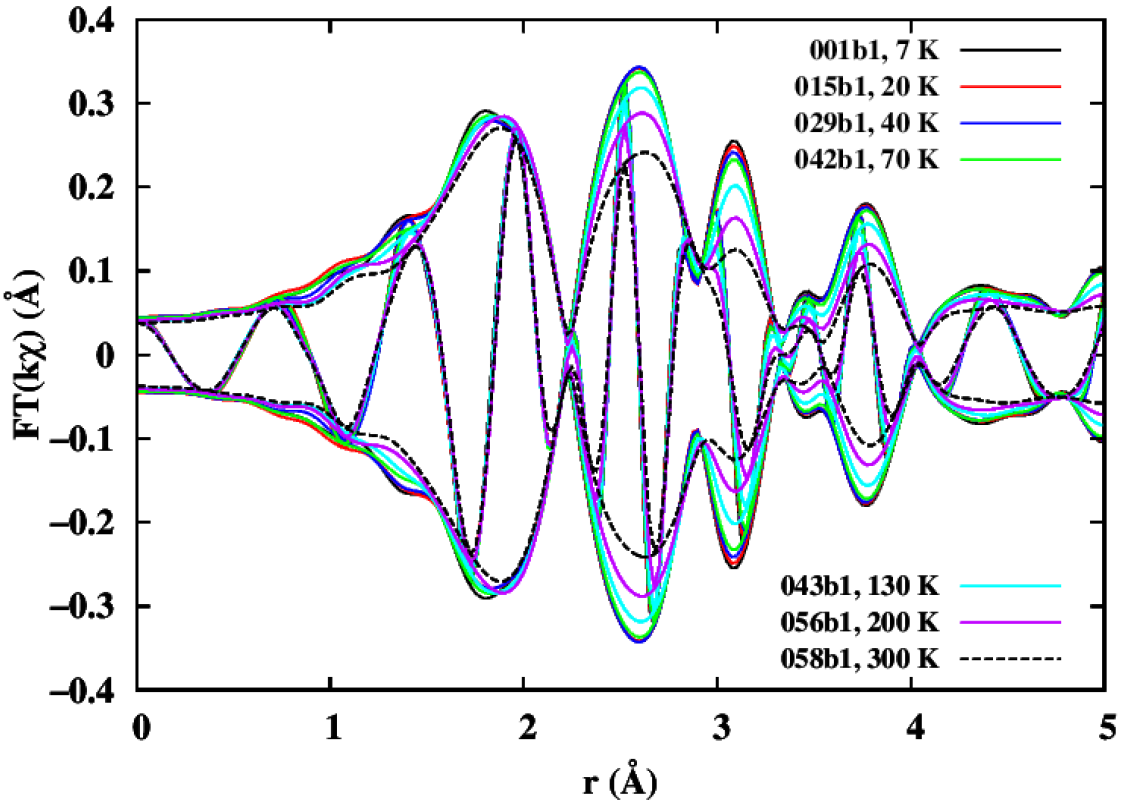


Figure B.2: The Fourier transform of the Ru K absorption edge k-space data. The data depicted had no Fe concentration at all set temperatures.

# Appendix C

# RSFIT Fits

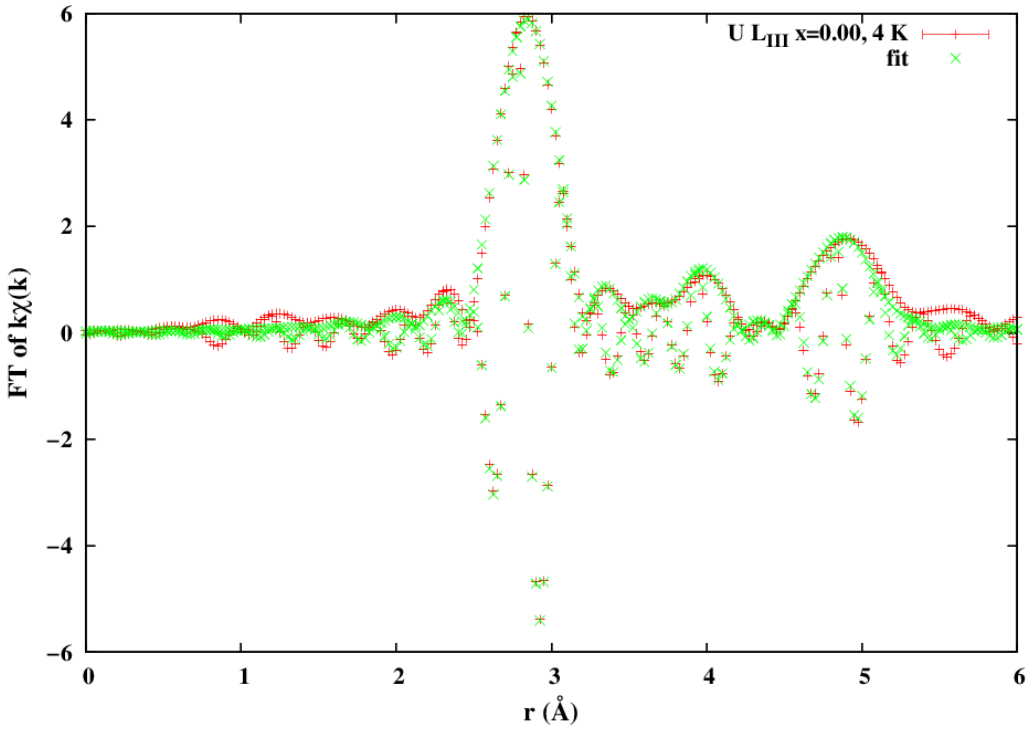


Figure C.1: The 8 standard files for the U $L_{III}$ edge are used to fit the transmission data of the U edge with no Fe concentration at 4 K by the RSFIT program. The red plus symbols represent the U edge transmission data. The green line represents the fit of the 8 standard files. The data were fit to the 8 standards from 2.5 Å to 5.3 Å.

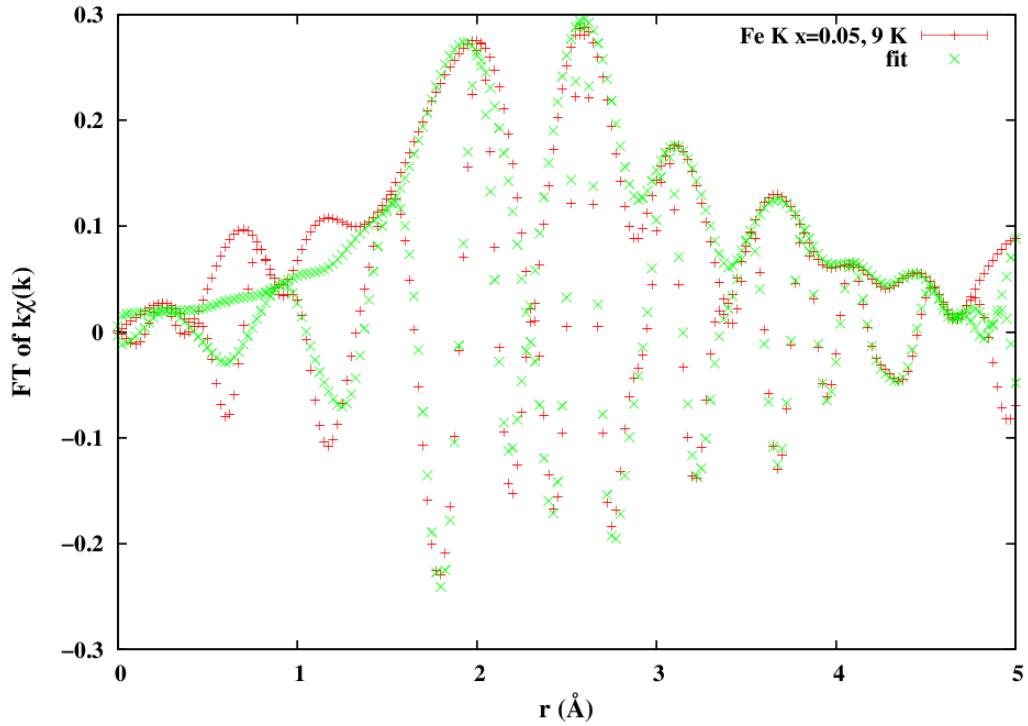


Figure C.2: A fit of the Fe K edge EXAFS data to a sum of 10 standard files for the fluorescence data by the RSFIT program. The red plus symbols represent the Fe edge fluorescence data. The green line represents the fit of the 10 standard files. The data were fit to the 10 standards from 1.8 Å to 4.5 Å.

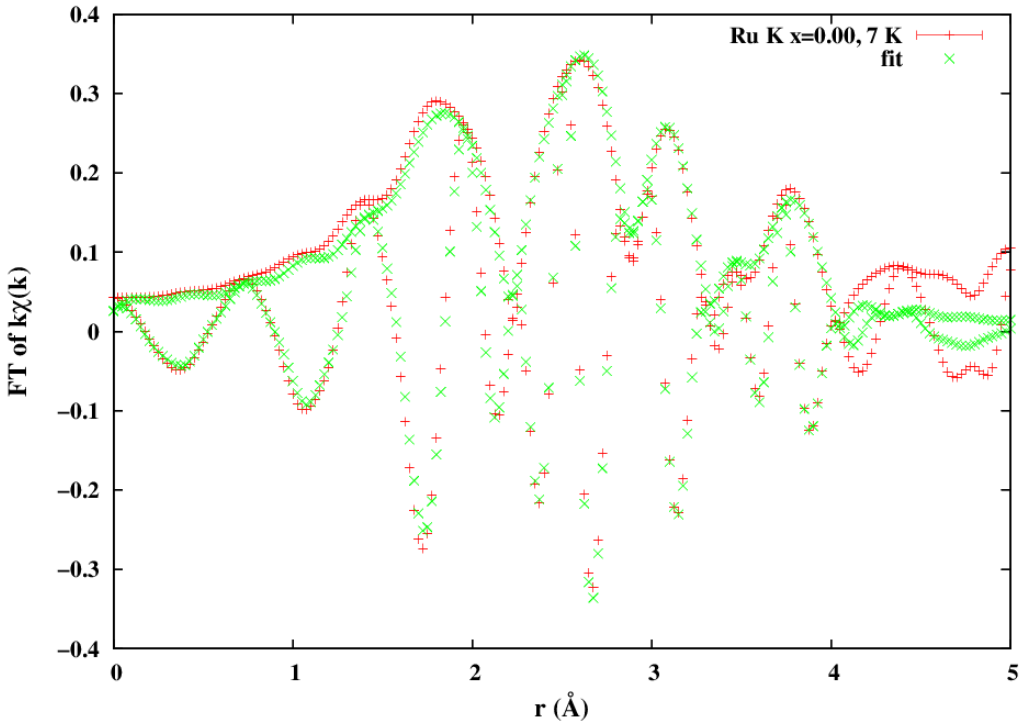


Figure C.3: A similar fit of the Ru K edge EXAFS data to a sum of 9 standard FEFF files using the RSFIT program. The red plus symbols represent the Ru edge transmission data. The green line represents the fit of the 9 standard files. The data were fit to the 9 standards from 1.8 Å to 4.0 Å.

# Appendix D

# Position Plots

## D.1 U Edge Position plots

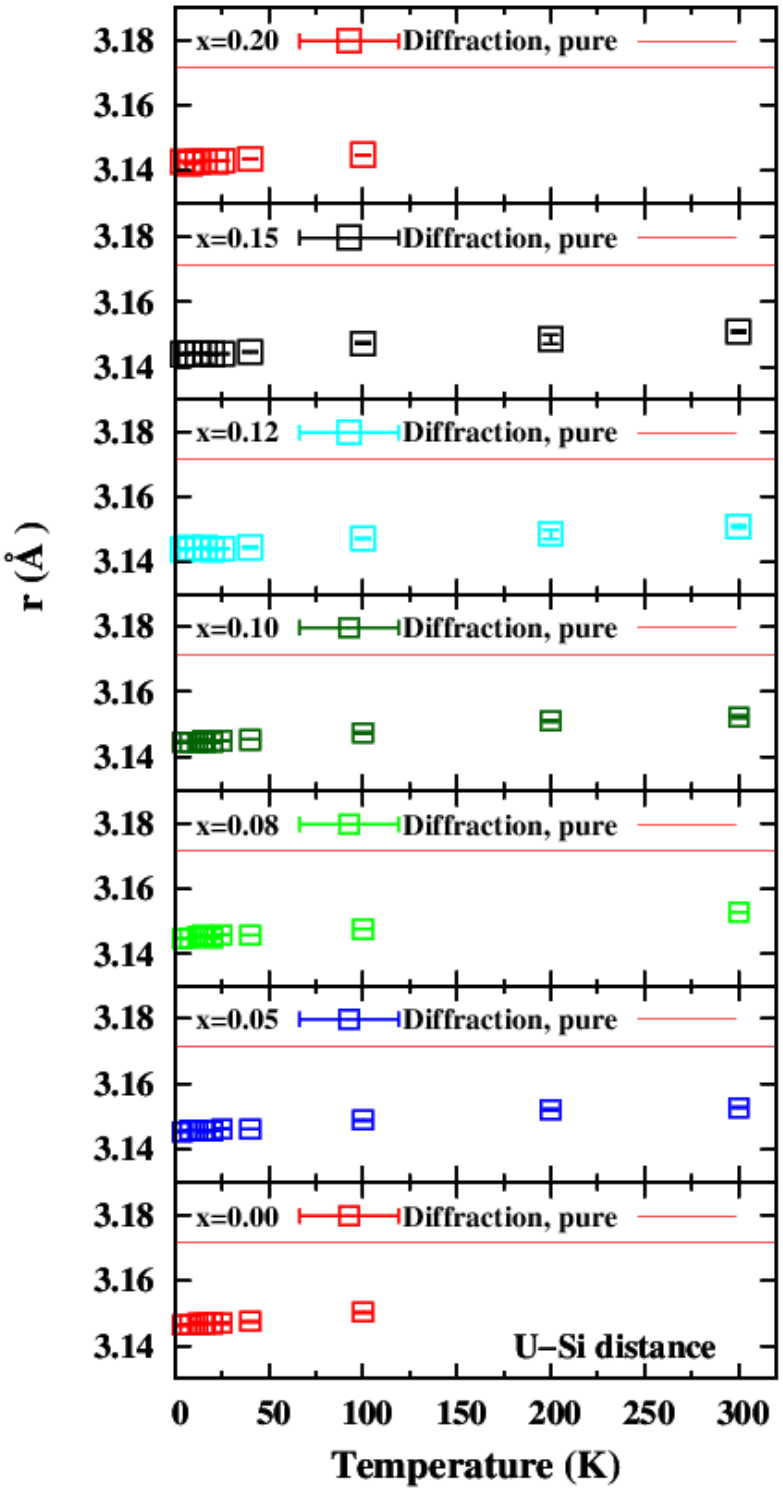


Figure D.1: The average distance between U and its closest Si neighbor as a function of temperature. The distance between U and its closest Si neighbor was found to be 3.1715 Å based on diffraction at 300 K, and is depicted as the solid red line. There is a discrepancy in comparison with diffraction at 300 K; the EXAFS distances are about 0.02 Å shorter.

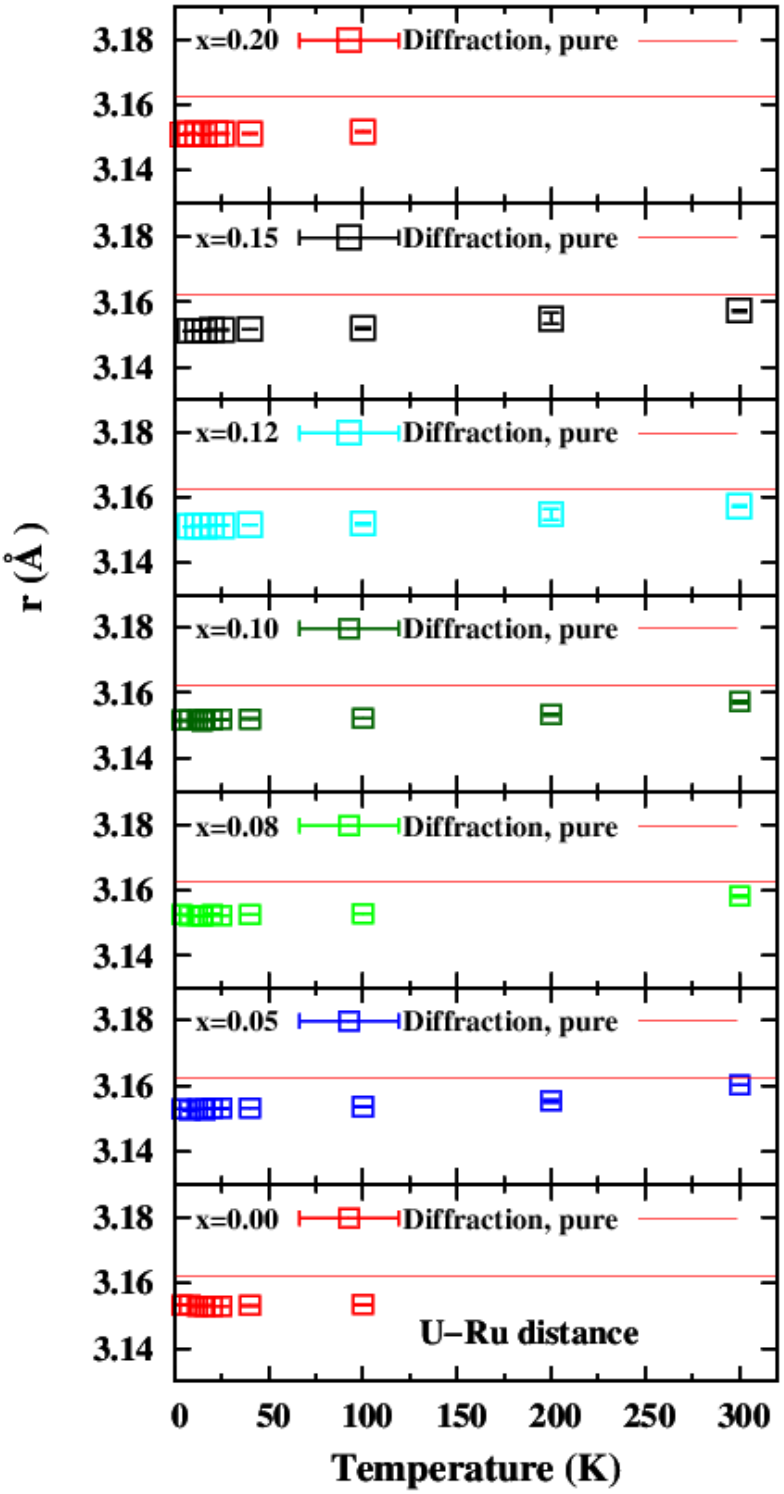


Figure D.2: The average distance between U and and its closest Ru neighbor as a function of temperature. The distance between U and its closest Ru neighbor was found to be 3.1623 Å based on diffraction at 300 K, and is depicted as the solid red line. The EXAFS distances are comparable to that of diffraction at 300 K.

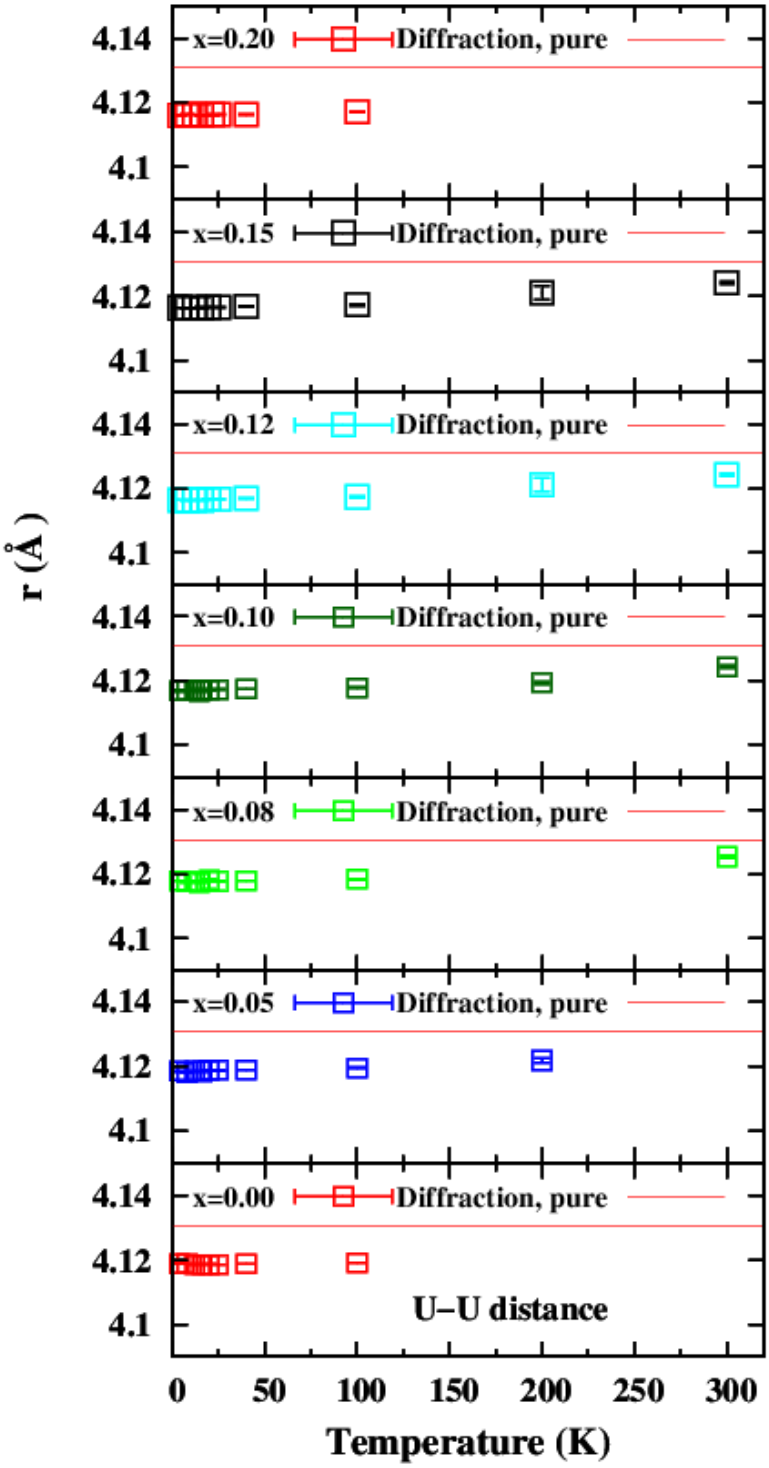


Figure D.3: The average distance between U and its closest U neighbor as a function of temperature. The distance between U and its closest U neighbor was found to be 4.1308 Å based on diffraction at 300 K, and is depicted as the solid red line. The EXAFS distances at 300 K is about 0.006 Å less than diffraction distance results at 300 K.

## D.2 Fe Edge Position plots

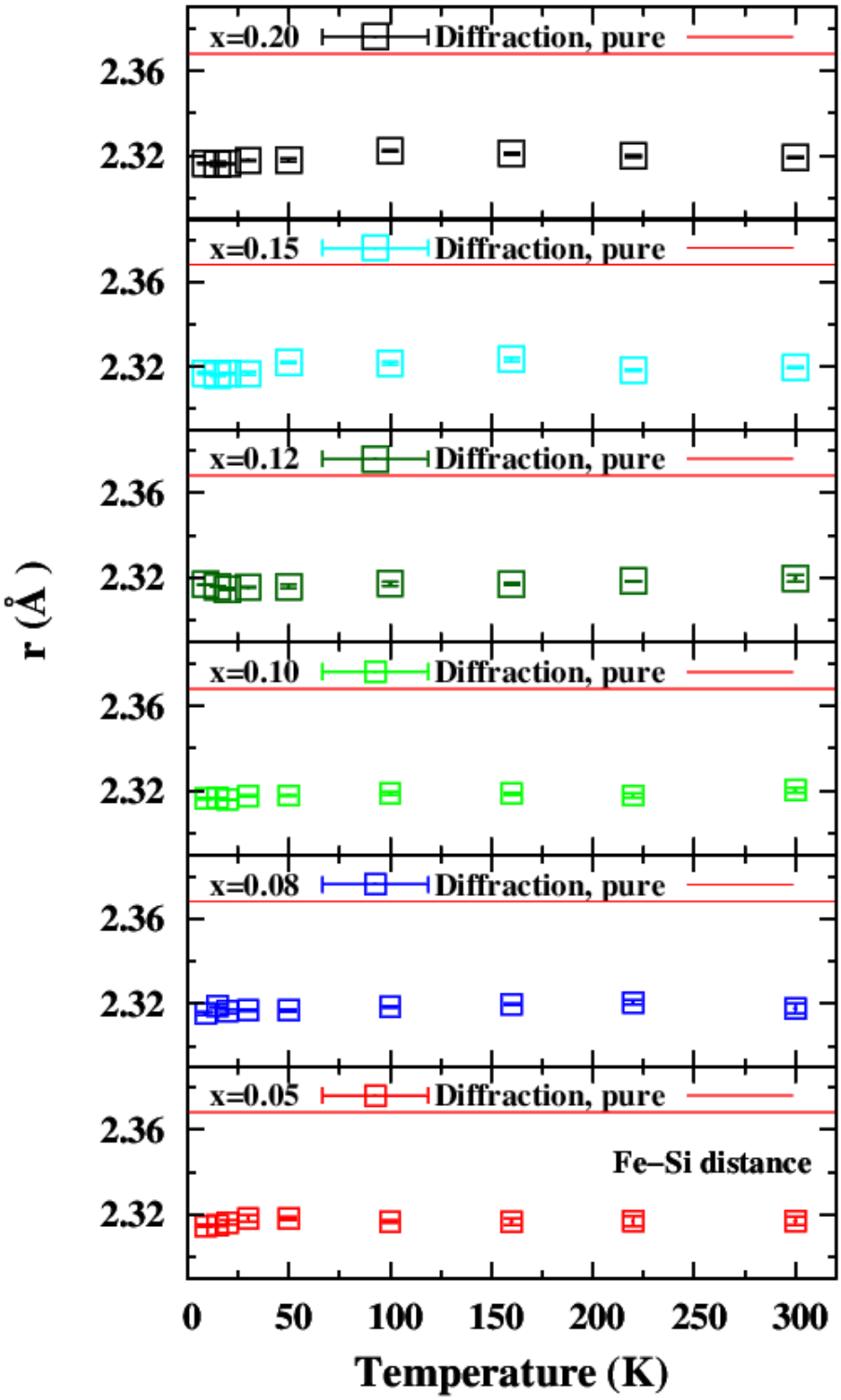


Figure D.4: The average distance between Fe and its closest Si neighbor as a function of temperature. The solid red line resembles the distance of 2.3683 Å between Ru and Si that is based on diffraction at 300 K. The Fe-Si bond is significantly shorter by roughly 0.05 Å compared to Ru-Si, which agrees with the concept of chemical pressure.

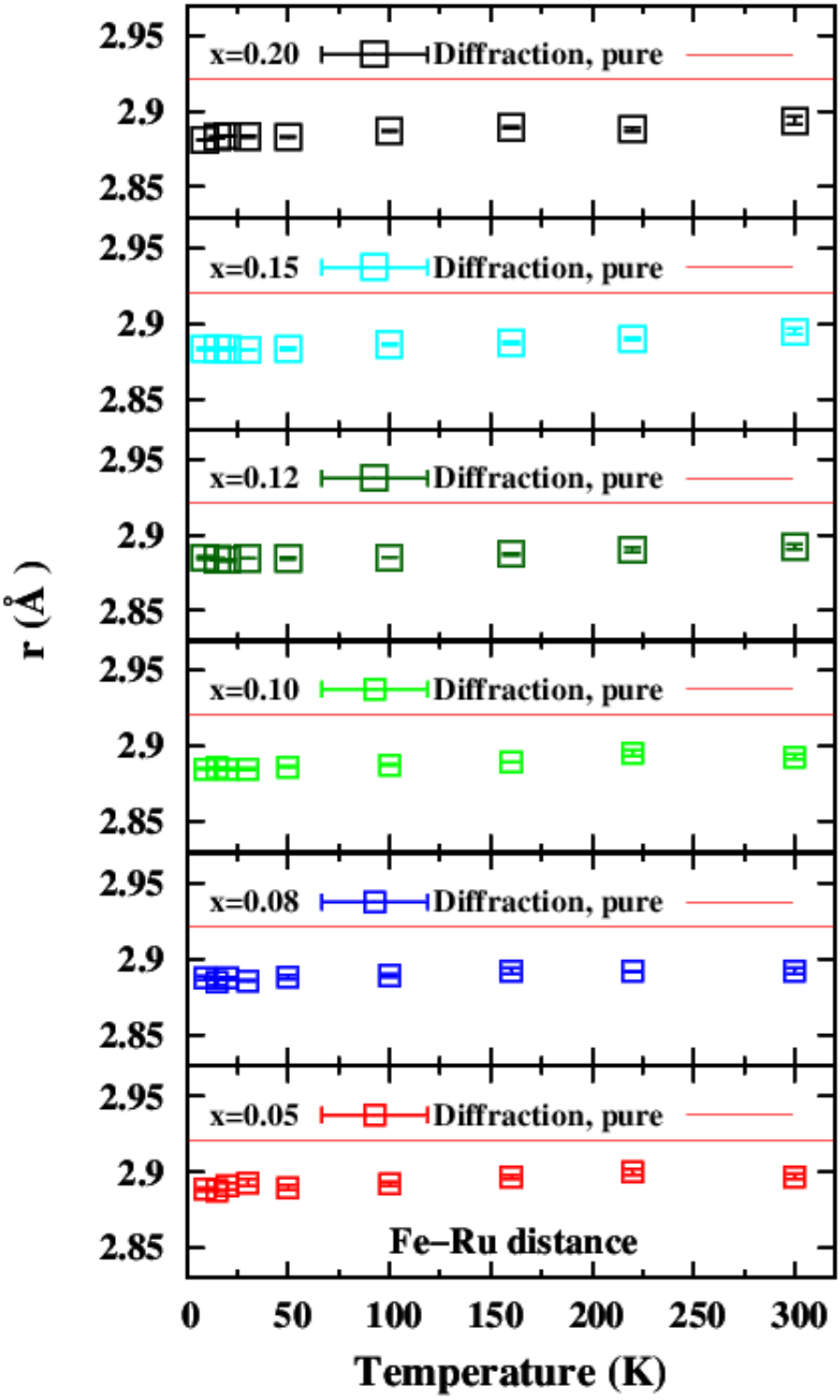


Figure D.5: The average distance between Fe and its closest Ru neighbor as a function of temperature. The solid red line resembles the distance of 2.9209 Å between Ru and Ru that is based on diffraction at 300 K. The Fe-Ru bond is shorter than the Ru-Ru distance based on diffraction at 300 K by approximately 0.03 Å, which agrees with the concept of chemical pressure. 130

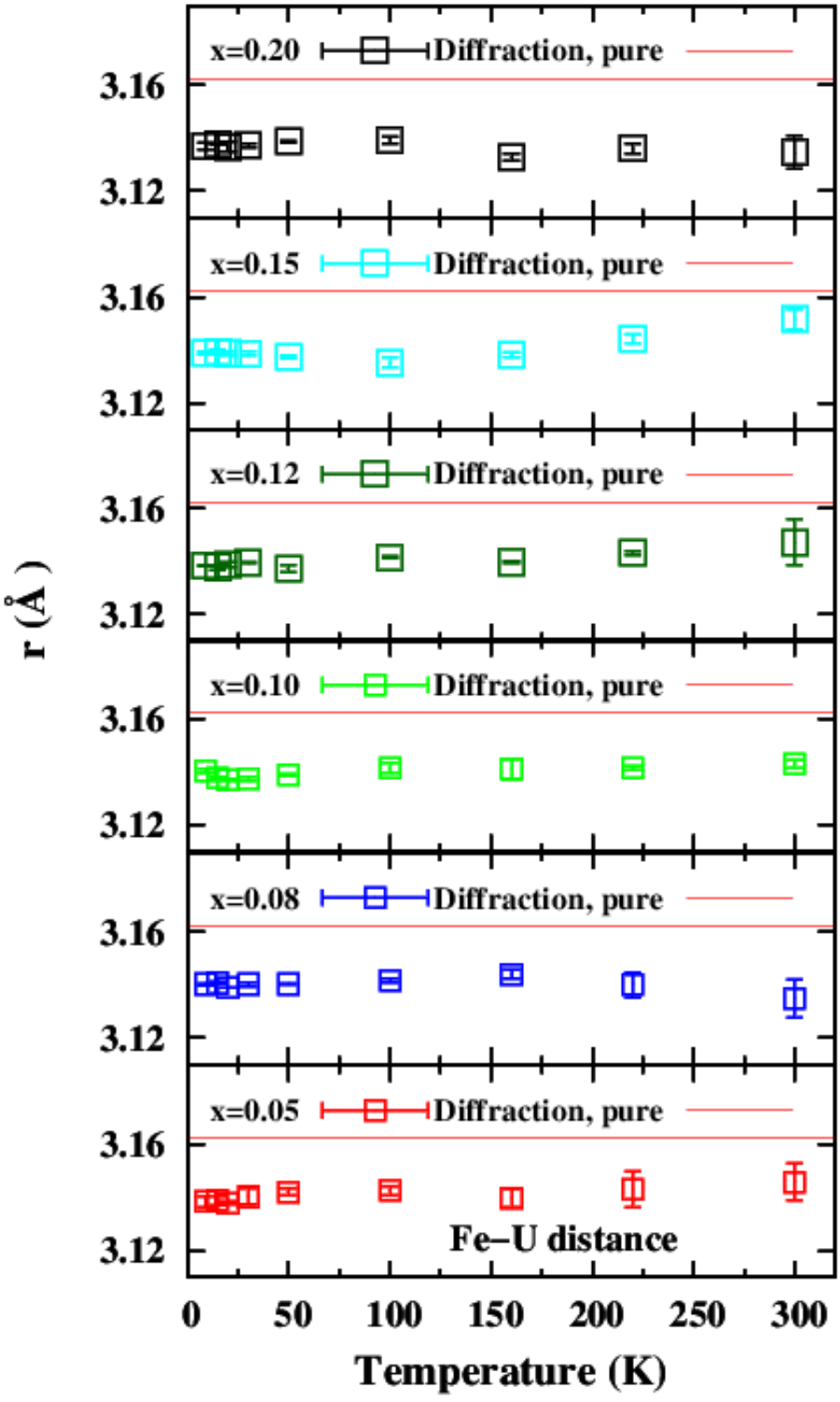


Figure D.6: The average distance between Fe and its closest U neighbor as a function of temperature. The solid red line resembles the distance of 3.1623 Å between Ru and U that is based on diffraction at 300 K. The Fe-U bond is shorter than the Ru-U distance based on diffraction at 300 K by approximately 0.02 Å, which agrees with the concept of chemical pressure.

## D.3 Ru Edge Position plots

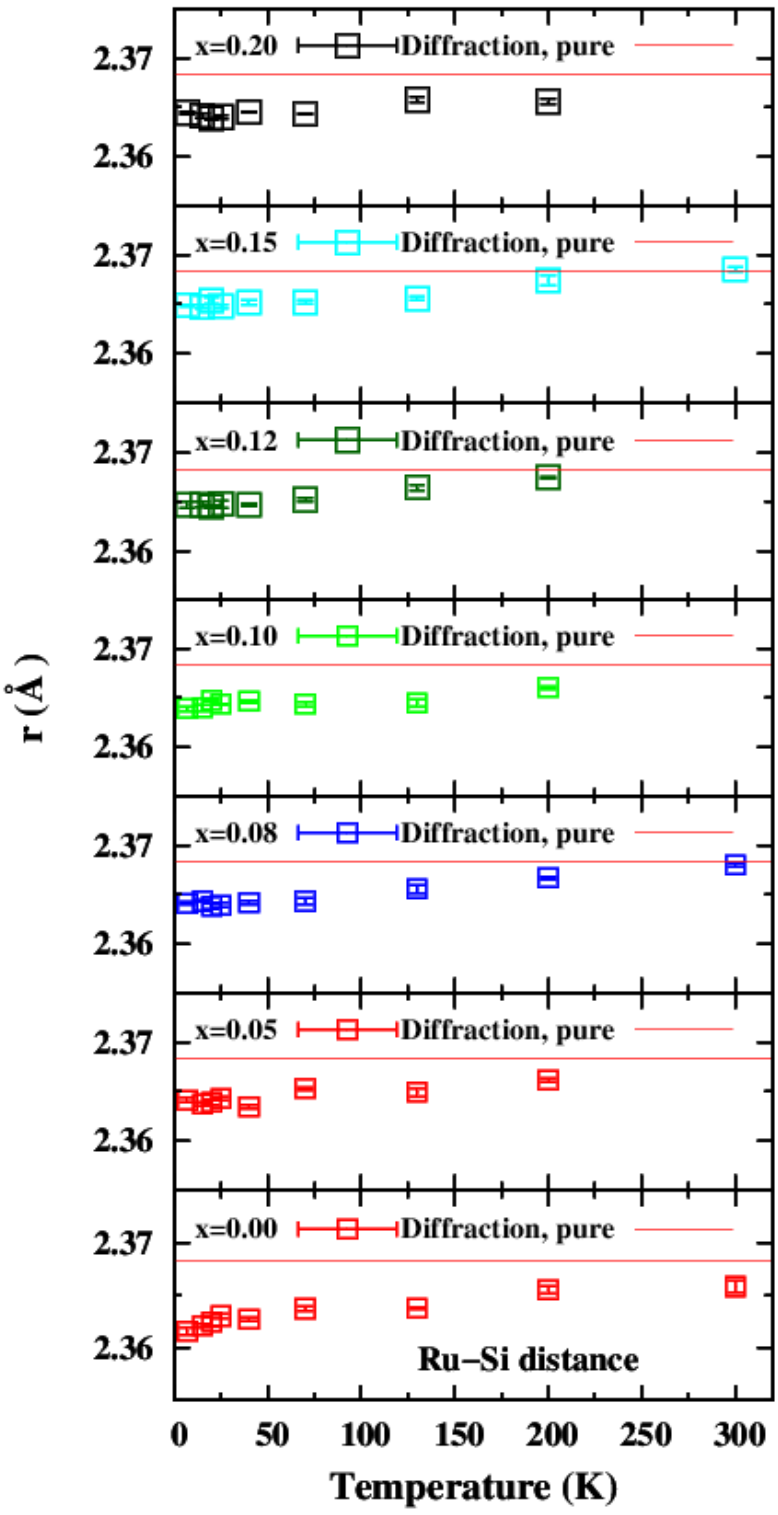


Figure D.7: The average distance between Ru and its closest Si neighbor as a function of temperature. The distance between Ru and its closest Si neighbor was found to be 2.3683 Å based on diffraction at 300 K, and is depicted as the solid red line. The Ru-Si distance from EXAFS agrees well with diffraction at 300K.

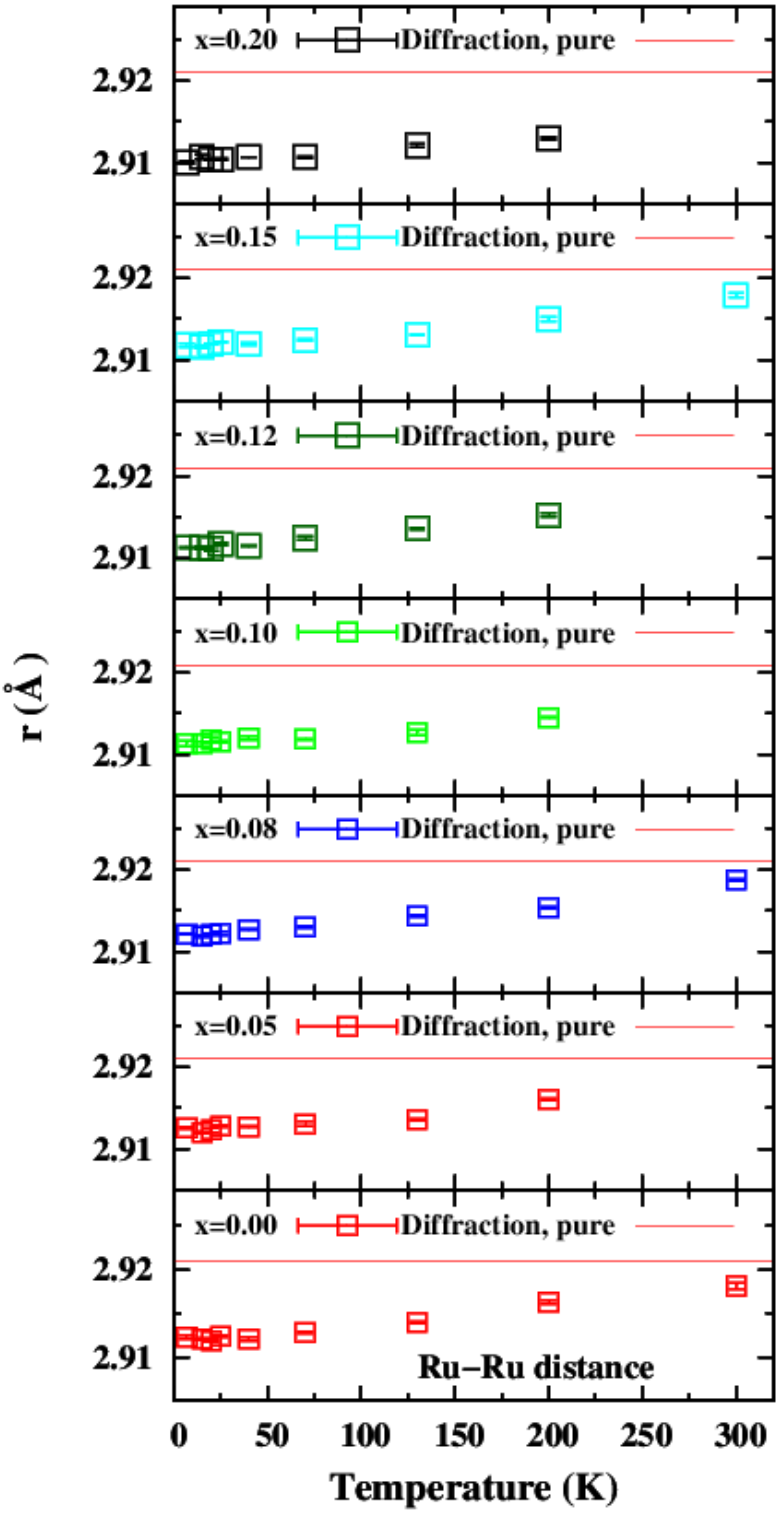


Figure D.8: The average distance between Ru and its closest Ru neighbor as a function of temperature. The distance between Ru and its closest Ru neighbor was found to be 2.9209 Å based on diffraction at 300 K, and is depicted as the solid red line. The Ru-Ru distance from EXAFS agrees well with diffraction at 300K.

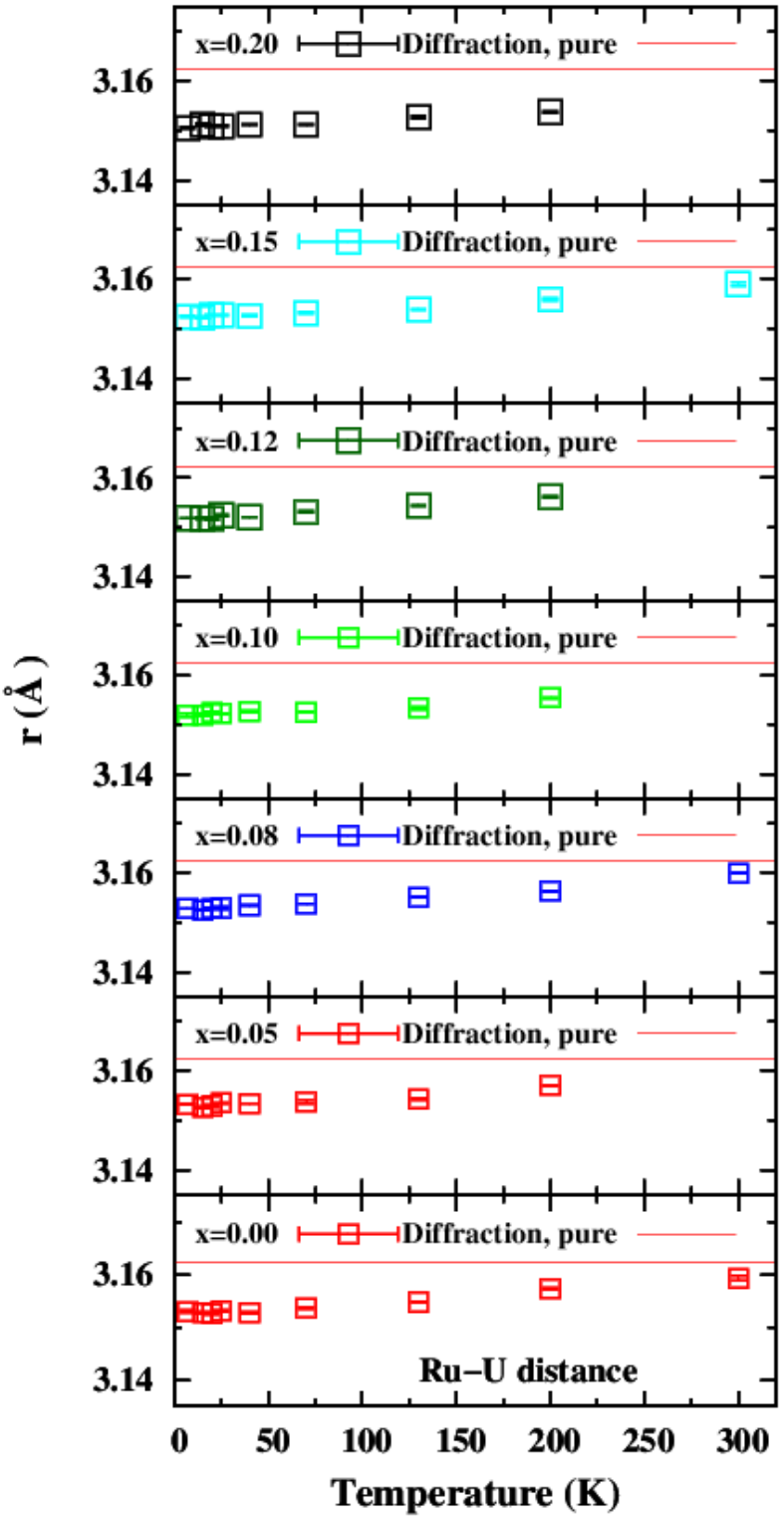


Figure D.9: The average distance between Ru and its closest U neighbor as a function of temperature. The distance between Ru and its closest U neighbor was found to be 3.1623 Å based on diffraction at 300 K, and is depicted as the solid red line. The Ru-U distance from EXAFS agrees well with diffraction at 300K.

# Appendix E

# Debye Temperature vs x Plots

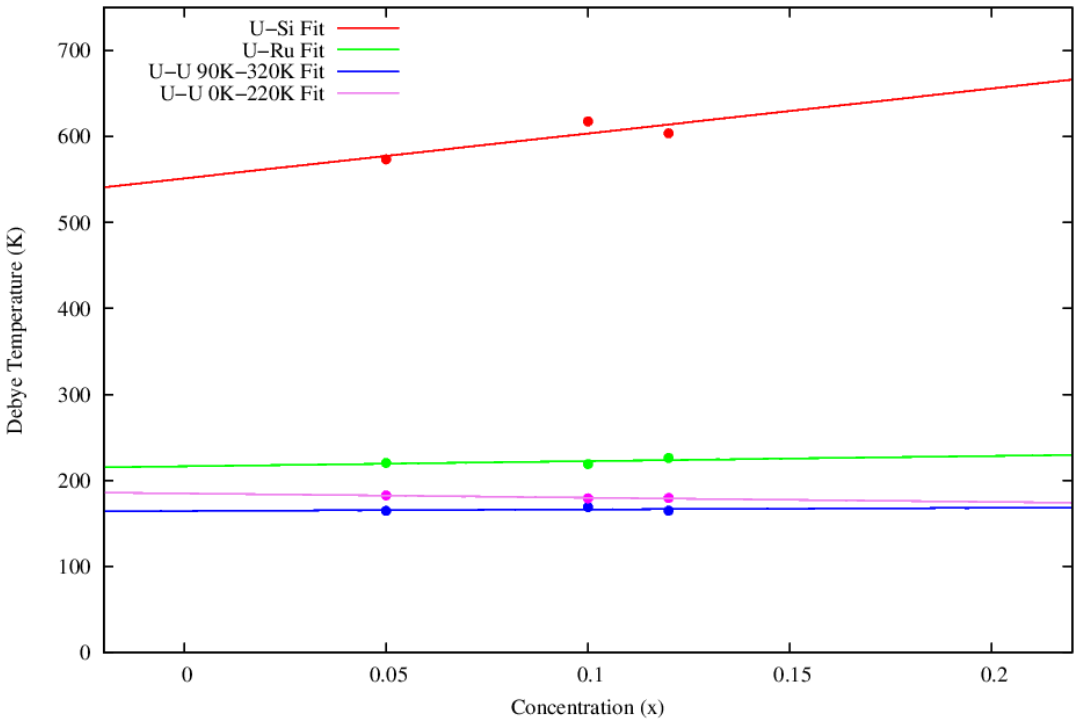


Figure E.1: The Debye temperature $\Theta_D$ vs concentration x for the first 3 single scattering peaks of the U edge. Only x=0.05, x=0.10, and x=0.12 had data up to 300K. A line was fit through the 3 data points corresponding to each individual peak. The Debye temperature for the other concentrations were taken from the value on the linear fit.

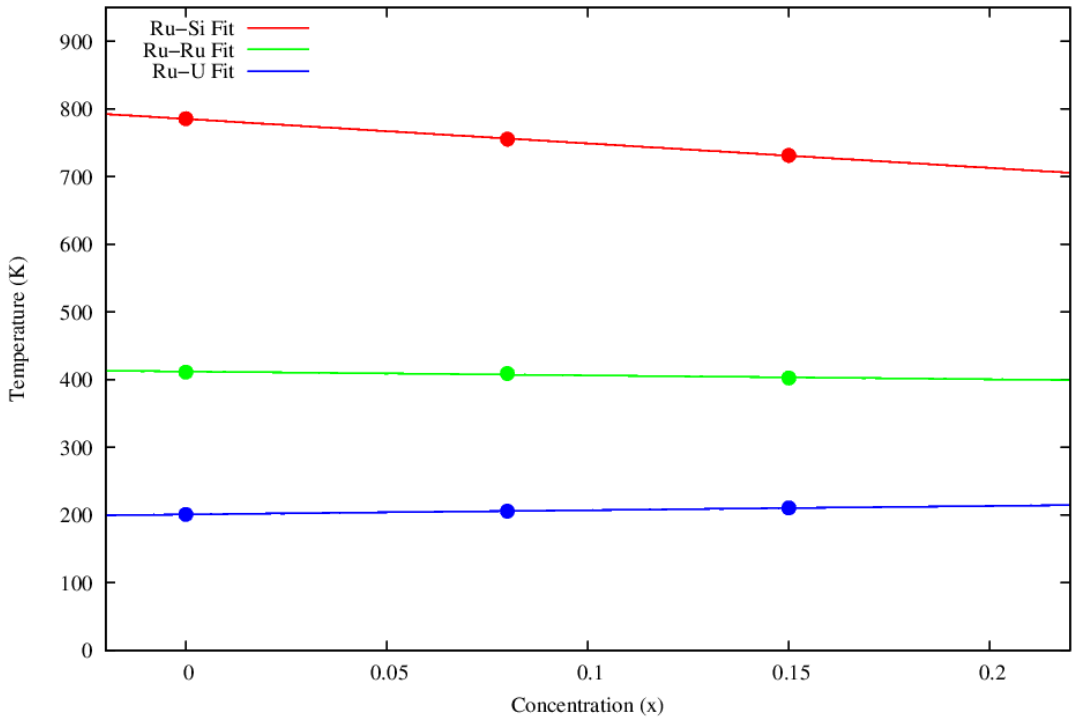


Figure E.2: The Debye temperature $\Theta_D$ vs concentration x for the first 3 single scattering peaks of the Ru edge. Only x=0.00, x=0.08, and x=0.15 had data up to 300K. A line was fit through the 3 data points corresponding to each individual peak. The Debye temperature for the other concentrations were taken from the value on the linear fit.

# Bibliography

[1] Auger, P. (1923). Sur les rayons $\beta$ secondaires produits dans un gaz par des rayons X. CR Acad. Sci.(F), 177, 169.

[2] Bragg, W. H., & Bragg, W. L. (1913). The reflection of X-rays by crystals. Proceedings of the Royal Society of London. Series A, Containing Papers of a Mathematical and Physical Character, 88(605), 428-438.

[3] Ewald, P. P. (1921). "Die Berechnung optischer und elektrostatischer Gitterpotentiale". Annalen der Physik. 369 (3): 253287.

[4] Sevillano, E., Meuth, H., & Rehr, J. J. (1979). Extended X-ray Absorption Fine Structure Debye-Waller Factors. I. Monatomic Crystals. Physical Review B, 20(12), 4908.

[5] Lee, P. A., Citrin, P. H., Eisenberger, P. T., & Kincaid, B. M. (1981). Extended X-ray Absorption Fine Structure  Its Strengths and Limitations as a Structural Tool. Reviews of Modern Physics, 53(4), 769.

[6] Sayers, D. E., Stern, E. A., & Lytle, F. W. (1971). New Technique for Investigating Noncrystalline Structures: Fourier Analysis of the Extended X-rayAbsorption Fine Structure. Physical Review Letters, 27(18), 1204.

[7] Lee, P. A., Pendry, J. B. (1975). Theory of Extended X-ray Absorptionb Fine Structure. Phys. Rev B, 11(8), 2795

[8] Lee, P. A. (1976). Possibility of adsorbate position determination using final-state interference effects. Physical Review B, 13(12), 5261.

[9] (n.d.). Retrieved June 11, 2019, from http://www.cryst.ehu.es/cgi-bin/cryst/programs/nph-wp-list?gnum=139

[10] Schlabitz, W., Baumann, J., Diesing, J., Krause, W., Neumann, G., Bredl, C.D., Ahlheim, U., Mayer, H.M., Rauchschwalbe, U.: Poster presented at the Fourth International Conference on Valence Fluctuations ICVF, Cologne 1984 (unpublished).

[11] Schlabitz, W., Baumann, J., Pollit, B., Rauchschwalbe, U., Mayer, H. M., Ahlheim, U., & Bredl, C. D. (1986). Superconductivity and Magnetic Order in a Strongly Interacting Fermi-System: $URu_2Si_2$. In Ten Years of Superconductivity: 1980 -1990 (pp. 89-95). Springer, Dordrecht.

[12] Palstra, T. T. M., Menovsky, A. A., Van den Berg, J., Dirkmaat, A. J., Kes, P. H., Nieuwenhuys, G. J., & Mydosh, J. A. (1985). Superconducting and Magnetic Transitions in the Heavy-Fermion System $URu_2Si_2$. Physical Review Letters, 55(24), 2727.

[13] Maple, M. B., Chen, J. W., Dalichaouch, Y., Kohara, T., Rossel, C., Torikachvili, M. S., ... & Thompson, J. D. (1986). Partially Gapped Fermi Gurface in the Heavy-Electron Superconductor $URu_2Si_2$. Physical Review Letters, 56(2), 185.

[14] Broholm, C., Kjems, J. K., Buyers, W. J. L., Matthews, P., Palstra, T. T. M., Menovsky, A. A., & Mydosh, J. A. (1987). Magnetic excitations and ordering in the heavy-electron superconductor $URu_2Si_2$. Physical review letters, 58(14), 1467.

[15] Isaacs, E. D., McWhan, D. B., Kleiman, R. N., Bishop, D. J., Ice, G. E., Zschack, P., ... & Buyers, W. J. L. (1990). X-ray magnetic scattering in antiferromagnetic $URu_2Si_2$. Physical review letters, 65(25), 3185.

[16] Booth, C. H., Medling, S. A., Tobin, J. G., Baumbach, R. E., Bauer, E. D., Sokaras, D., ... & Weng, T. C. (2016). Probing 5 f-state configurations in $URu_2Si_2$ with U $L_{III}$-edge resonant x-ray emission spectroscopy. Physical Review B, 94(4), 045121.

[17] Butch, N. P., Manley, M. E., Jeffries, J. R., Janoschek, M., Huang, K., Maple, M. B., ... & Lynn, J. W. (2015). Symmetry and correlations underlying hidden order in $URu_2Si_2$. Physical Review B, 91(3), 035128.

[18] Wray, L. A., Denlinger, J., Huang, S. W., He, H., Butch, N. P., Maple, M. B., ... & Chuang, Y. D. (2015). Spectroscopic determination of the atomic f-electron symmetry underlying hidden order in $URu_2Si_2$. Physical review letters, 114(23), 236401.

[19] De Boer, F. R., Franse, J. J. M., Louis, E., Menovsky, A. A., Mydosh, J. A., Palstra, T. T. M., ... & De Visser, A. (1986). High-magnetic-field and high-pressure effects in monocrystalline $URu_2Si_2$. Physica B+ C, 138(1-2), 1-6.

[20] Amitsuka, H., Sato, M., Metoki, N., Yokoyama, M., Kuwahara, K., Sakakibara, T., ... & Mydosh, J. A. (1999). Effect of pressure on tiny antiferromagnetic moment in the heavy-electron compound $URu_2Si_2$. Physical Review Letters, 83(24), 5114.

[21] Kanchanavatee, N., Janoschek, M., Baumbach, R. E., Hamlin, J. J., Zocco, D. A., Huang, K., & Maple, M. B. (2011). Twofold enhancement of the hidden-order/large-moment antiferromagnetic phase boundary in the $URu_{2-x}Fe_xSi_2$ system. Physical Review B, 84(24), 245122.

[22] Ran, S., Wolowiec, C. T., Jeon, I., Pouse, N., Kanchanavatee, N., White, B. D., ... & Williamsen, M. (2016). Phase Diagram and Thermal Expansion Measurements on the System $URu_{2-x}Fe_xSi_2$. Proceedings of the National Academy of Sciences, 113(47), 13348-13353.

[23] Ran, S., Jeon, I., Pouse, N., Breindel, A. J., Kanchanavatee, N., Huang, K., ... & Singleton, J. (2017). Phase diagram of $URu_{2x}Fe_xSi_2$ in high magnetic fields. Proceedings of the National Academy of Sciences, 114(37), 9826-9831. Chicago

[24] Phillips, J. C., Hodgson, K. O., Winick, H., & Doniach, S. (1980). Synchrotron Radiation Research. edited by H. Winick and S. Doniach. New York/London: Plenum, 565-605.

[25] Buhot, J., Masson, M. A., Gallais, Y., Cazayous, M., Sacuto, A., Bourdarot, F., ... & Ivanov, A. (2015). Lattice Dynamics of the Heavy-Fermion Compound $URu_2Si_2$. Physical Review B, 91(3), 035129.